Contents

Superconducting Dipole Magnet

The SC dipole magnet 3D modeling for muon option of the CBM detector

P.G. Akishin[*1], *V.V. Ivanov*[1], *V.P. Ladygin*[2], *and A.I. Malakhov*[2]
[1]LIT-JINR, Dubna, Russian Federation; [2]LHEP-JINR, Dubna, Russian Federation

The superconducting dipole magnet is a central part of the CBM experiment detection system [1]. The target station, the Micro-Vertex Detector (MVD) and the Silicon Tracking System (STS) are placed in the magnet gap, which has a height of 140 cm and a width of 250 cm in order to cover a polar angle acceptance of $\pm 25°$ and a horizontal acceptance of $\pm 30°$. The magnet has to provide a vertical magnetic field with a bending power of $\sim 1\ T{\cdot}m$ over a length of 1 m from the target. One of the options of the CBM detector includes a muon detection system (MuCH), which consists of 6 hadron absorber blocks and 6 tracking detector triplets [2] placed downstream the magnet. This report presents the calculation of the magnitude of the magnetic field and acting forces on the MuCH detector.

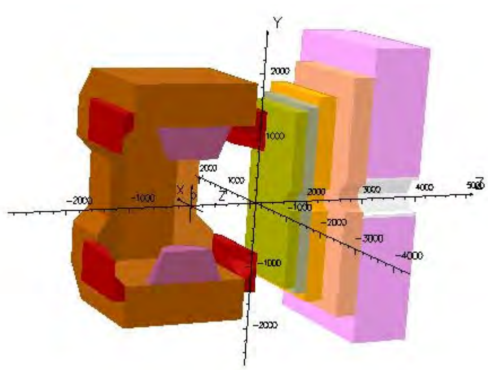

Figure 1: 3D model for CBM SC dipole magnet with MuCH system.

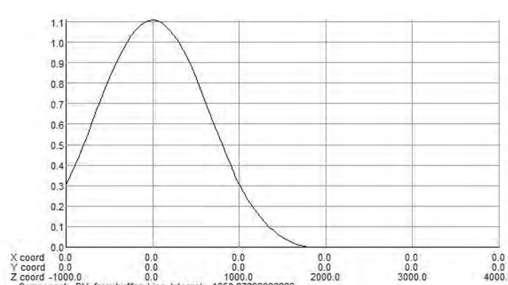

Figure 2: Vertical magnetic field component B_y distribution along the beam direction.

* akishin@jinr.ru

One half of a simplified 3D model for CBM SC dipole magnet with MuCH system is shown in Figure 1. It is assumed that the first absorber and supporting structure of the MuCH system are made from the nonmagnetic materials. The magnetic field calculations have been performed using 3D TOSCA code [3]. Two plane symmetries of the magnetic field have been used in the modeling. The current density is taken as 43.93 A/mm^2, which provides the total current through one coil of 1.121 MA. The calculated stored energy is 4.592 MJ. The vertical magnetic field component B_y distribution along the beam direction is presented in Figure 2. The maximal value of the B_y component is $\sim 1.1\ T$ with the field integral of $\sim 1\ T{\cdot}m$.

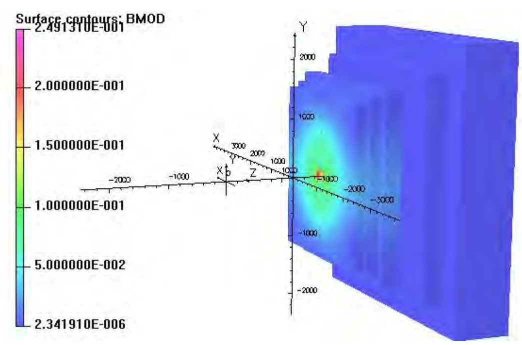

Figure 3: Magnetic field saturation picture in the MuCH absorber.

The distribution of the magnetic field in the MuCH absorber is shown in Figure 3. The maximal value of the magnetic field of $\sim 0.25\ T$ is in the center of the first absorber.

Table 1: Forces (in $[N]$) acting on the MuCH absorbers.

No. of absorber	2	3	4	5	6
Force $[N]$	1358	459	174	0.06	0.1

The results of the calculations for the forces acting on the MuCH absorbers are presented in Table 1. These forces are negligible for the last 2 absorbers.

References

[1] The CBM collaboration, Technical Design Report for the CBM Superconducting Dipole Magnet, Darmstadt 2014.

[2] S.Ahmad et al., Nucl.Instrum.Meth. A775 (2014) 139.

[3] OPERA-3d User Guide, http://www.lepp.cornell.edu/critten/opera/user-3d.pdf.

Superconducting dipole magnet for the Compressed Baryon Matter (CBM) experiment at FAIR.

A.V. Bychkov[1], *Yu.V. Gusakov*[*1], *P.K. Kurilkin*[1], *V.P. Ladygin*[1], *A.I. Malakhov*[1], *G. Moritz*[2], *P. Senger*[2], *and A.V. Shabunov*[1]

[1]LHEP-JINR, Dubna, Russian Federation; [2]GSI, Darmstadt, Germany

The superconducting dipole magnet is a central part of the CBM detector system. The magnet has to provide the vertical magnetic field with a bending power of 1 Tm on the length 1m from the target. The magnet gap has a height of 140 cm and a width of 250 cm in order to accommodate the target station, Micro- Vertex Detector and Silicon Tracking System providing a polar angle acceptance of $\pm 25°$ and a horizontal acceptance of $\pm 30°$.

The CBM superconducting dipole magnet [1] is of H-type with a warm iron yoke/pole and cylindrical superconducting coils in two separate cryostats. The potted coil has 1749 turns. The wire, similar to the CMS wire, has Nb-Ti filaments embedded in a copper matrix and is soldered in a copper stabilizer with a total Cu/SC ratio of about 13 in the conductor. The operating current and the maximal magnetic field in the coils are 686 A and 3.25 T, respectively. The coil case made of stainless steel contains 20 liters of liquid helium for one coil. The vertical force in the coils is about 250 t. The cold mass is suspended from the room-temperature vacuum vessel by six suspension links. Six cylindrical support struts compensate the vertical forces. Design calculations for CBM superconducting dipole magnet have been performed [2]. The code TOSCA was used for calculating electromagnetic forces exerted on the coil, while the structural analysis for the coil case, the coil vessel and the support links was made using the code ANSYS.

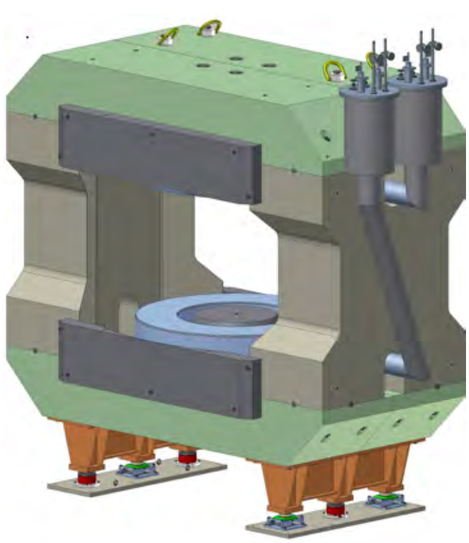

Figure 1: CBM dipole magnet with the support.

The energy stored in the magnet is about 5 MJ. The magnet will be self-protecting. However, in order to limit the temperature rise to 100 K in case of a quench, the energy will be dumped in an external resistor [3].

One of the purpose of the magnet support is the vertical and horizontal adjustment of the CBM magnet. A perspective view of the CBM magnet with the support is shown in Fig.1. The design of the CBM magnet is corrected according to Toshiba recommendations.

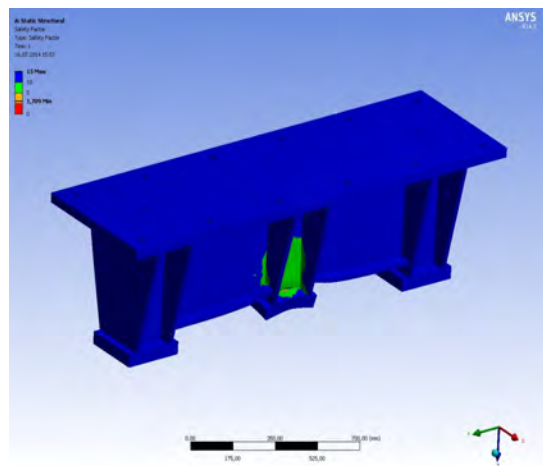

Figure 2: Results of the stress calculations for the support beam using ANSYS code.

The magnet support consists of two support beams each of them is placed on the base plate. The vertical adjustment of the magnet is provided by 3 hydraulic jacks. 3 roller skids is used for the adjustment in the horizontal plane. They allow to adjust the magnet position along and transversely to the beam direction as well as provide the rotation in the horizontal plane. 6 sets of the magnetic base with digital indicators are used for displacement control. The results of the stress calculation for the beam support using ANSYS code is shown in Fig.2. The design of the support system satisfies to the CBM magnet requirements [1].

References

[1] The CBM collaboration, Technical Design Report for the CBM Superconducting Dipole Magnet, Darmstadt 2014.

[2] P.Akishin et al., CBM Progress Report 2013, Darmstadt 2014, pp.7-8.

[3] P.Kurilkin et al., CBM Progress Report 2013, Darmstadt 2014, p.10.

* Iourii.Goussakov@cern.ch

3D CIEMAT code optimization for the CBM magnet quench calculation.

P. Kurilkin[*1], *P. Szwangruber*[2], *E. Floch*[2], *F. Toral*[3], *A. Malakhow*[1], *and V. Ladygin*[1]

[1]LHEP-JINR, Dubna, Russian Federation; [2]GSI, Darmstadt, Germany; [3]CIEMAT, Madrid, Spain

A superconducting dipole magnet for the CBM experiment will be constructed and installed at CBM cave at GSI(Darmstadt, Germany). The important features of the CBM superconducting dipole magnet is a large gap (high of 1.4m and width of 2.5m) in order to accommodate the target and Silicon Tracking System.

The magnet is H-type dipole, having circular superconducting coils. It will store about 5.15 MJ at its nominal current of 686 A. The coil design for the CBM magnet is based on the design of the FAIR Super-FRS dipole. It has 1749 turns(53 layers with 33 turns per layer). The conductor insulation consist of 2×0.05 mm polyimide tape and 2×0.1 mm glassfiber material (tape or braid), in total 0.3 mm. The detailed information about coil and conductor structure can be found in [1].

To design the quench protection system for the magnet it is important to perform the simulation of the quench process in the coil at different operation conditions. This note presents the results of $3D$ calculations done with the use of two programs. One of them is currently used at GSI[2]. The other based on 3D CIEMAT code[3] was modified for CBM dipole magnet calculation[1].

The calculation presented here was done for the case when no dump resistor was used for the quench protection. Both calculations take into account the inductance function $L_d(I)$[1]. The 3D GSI calculation is performed for the uniform field map distribution in the coil using the maximal values $B_m(I)$ and also for the conductor insulation (G10 tape) of 0.3 mm thickness. The modified 3D CIEMAT program takes into account the real field map distribution in the coil and two layer of conductor insulation (0.1mm Kapton, 0.2mm G10). The additional 3D CIEMAT calculations have been performed to investigate the influence of the coil field map distribution and insulation properties on the simulation results.

Fig.1 and Fig.2 present the hot-spot temperature and quench voltage time dependence during the quench, respectively. Blue solid and dash-dotted curves are the results of 3D CIEMAT and GSI computation for uniform coil field map distribution and G10 conductor insulation, respectively. They gives the maximum hot-spot temperature and quench voltage on the level of 130 K and 1240 V, respectively. The difference between the results calculated with the GSI and CIEMAT models is related to the different material data bases used in those programs.

The red curves present the result of 3D calculation for two layer of conductor insulation(0.1mm Kapton, 0.2mm

* pkurilkin@jinr.ru

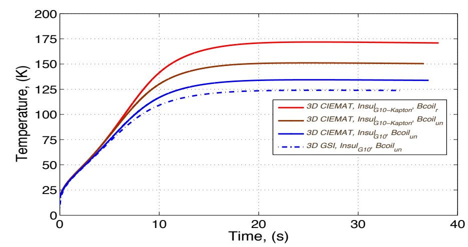

Figure 1: 3D quench calculation of the CBM dipole magnet – the hot-spot temperature.

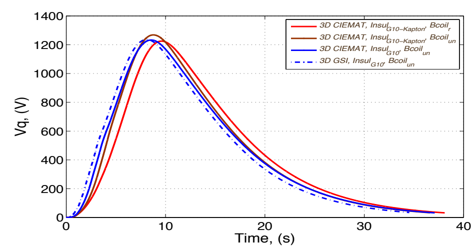

Figure 2: 3D quench calculation of the CBM dipole magnet– the quench voltage.

G10) and real field map distribution in the coil. The maximum hot-spot temperature and quench voltage equal to the 170 K and 1200 V,respectively.

The modification of the 3D CIEMAT program was done to perform the CBM magnet quench calculation for the use of two-layer conductor insulation of different type and real field map distribution in the coil. The presented results show that the CBM dipole magnet is a self-protecting.

References

[1] The Technical Design Report for the CBM Superconducting Dipole Magnet. *http://www.fair-center.eu/fileadmin/fair/experiments/CBM/TDR/CBM_magnet_TDR_31_10_2013-nc.pdf*

[2] *P. Szwangruber et al., "Three-Dimensional Quench Calculations for the FAIR Super-FRS Main Dipole", IEEE Transactions on Applied Superconductivity,* **23** *No.3 (2013) 4701704*

[3] *F. Toral, "Design and Calculation Procedure for Particle Accelerator Superconducting Magnets: Application to an LHC Superconducting Quadrupole", Ph. D. Thesis, Madrid, 2001*

[4] *P.Kurilkin et al., "Quench calculation for the CBM dipole magnet" CBM Progress Report 2013, Darmstadt 2014, p. 9*

Micro-Vertex Detector

Status of the CBM MVD simulation model*

S. Amar-Youcef[1], M. Deveaux[1], E. Krebs[1], B. Linnik[1], B. Milanovic[1], Ph. Sitzmann[1], T. Tischler[1], and J. Stroth[1,2]

[1]Goethe-Universität, Frankfurt, Germany; [2]GSI, Darmstadt, Germany

The MVD simulation model is subject to a major revision and considerable progress has been achieved. In the following its motivation and status are discussed.

Motivation

Due to its proximity to the target and its excellent spatial resolution the MVD is the dedicated detector to resolve secondary vertices. In addition, its capability to clean-up background in di-electron spectra is subject of a dedicated study [1]. However, the primal implementation in simulation lacked in a realistic description (with respect to e.g. the material budget or peculiar sensor features) for advanced studies. These studies are needed to develop strategies to achieve best performances, to analyze critical points and to finalize the concept of the MVD and its tools.

The revision of the MVD model, to be incorporated to the CbmRoot simulation framework, aims at a more realistic description of the current understanding of the MVD. Before, in the standard scenario, the MVD was simplified as two homogeneous discs at 5 cm and 10 cm downstream the target, with an outer (inner) radius of 2.5 cm (0.5 cm) and 5 cm (0.5 cm), respectively. As no representation of individual sensors was included, this simplification possesses many limitations. The limitations involves mainly sensor properties beyond the hit response as e.g. the data parallelism of sensors, the rolling-shutter frame read-out, bandwidth limitations, busy circuits, a definition of a fake hit rate, time stamping and the data format.

The new approach [2] addresses these issues and is based on a segmented geometry with four stations (at 5 cm, 10 cm, 15 cm and 20 cm downstream the target) including all relevant features. Its underlying sensor characteristics are borrowed from MIMOSIS. The detailed geometry was elaborated in CAD. The conversion from the respective description into the ROOT geometry format was conducted by a dedicated tool. In this way we are able to respond very quickly to changes in the detector design.

Along with the proper representation of the gradual material budget, there is the possibility to incorporate the missing features mentioned above, as hits are assigned to sensors now. The data parallelism is incorporated by restructuring the data processing through the three process steps called digitizer, clusterfinder and hitfinder. Here, the corresponding data representations called Monte Carlo (MC) hits, digis (firing pixels) and clusters, which serve as input for the respective process step are assigned to the respective sensors. All further properties of the sensors are incorporated within the digitizer. As previously mentioned digis are particularly important, as they describe the response of the sensor to impinging hits mimicked by the digitizer. Apart from the generated pattern of single hits the interference among hits is important to consider. This is implemented in the digitizer by creating the signal amplitudes and distributions of all hits before jointly discriminating to generate the binary charge measurement. Hits from consecutive events might pile-up and/or neighboring hits merge. This is particularly true due the long integration time of one frame of $\sim 30\ \mu s$. The respective output is dependent upon the features included as listed above. These features require a definition of the temporal sequence of the recorded MC hits accordingly. Its considerations are relevant especially for the time-based track reconstruction of CBM. The time-based consideration is a necessary condition to use the reconstruction software with real data, too.

In order to verify the performance in the reconstruction (e.g. tracking) matching of all data states is incorporated. All geometry information are accessible via the 'GeoHandler'-Class. For the tracking a simplified representation of the material budget is provided in the form of a map in dedicated files provided together with the digitizer.

In order to study the impact of misalignment the position of the individual sensors can be modified within simulation.

Status

The new MVD geometry and data processing has been incorporated and uploaded to CbmRoot. All functionality has been re-established and can be used within the event-based reconstruction. Due to constraints on the part of CbmRoot, the time-based reconstruction is not fully available for the time being. Likewise the MVD model does not yet comprise all the details. However, all preparations necessary have been provided. The pile-up of events can be studied via background events. Moreover, further details related to the performance of the sensor (as e.g. aging with the integrated radiation dose, noisy pixels, different pixel geometries) have not yet been treated.

The current representation of the MVD in simulation is the prerequisite to allow for realistic simulations on the performance of the MVD in secondary vertexing and background rejection in di-electorn spectroscopy.

References

[1] Erik Krebs, "Background rejection in the dilepton analysis with the CBM-Micro Vertex Detector", this report

[2] Philipp Sitzmann, "Integration eines sensorbasierten Detektorresponsemodells", Master-thesis 2015

* Work supported by BMBF (05P12RFFC7), HIC for FAIR and GSI

Non-ionizing radiation hardness of CMOS Monolithic Active Pixel Sensors manufactured in a 0.18μm CMOS process*

D. Doering[1], *M. Deveaux*[1], *B. Linnik*[1], *and J. Stroth*[1,2] *for the CBM-MVD collaboration*
[1]Institut für Kernphysik, Goethe-University Frankfurt, Germany; [2]GSI Darmstadt, Germany

Modern 0.18 µm CMOS processes provide numerous features, which may allow for decisive progresses in the read-out speed and the radiation tolerance of the CMOS Monolithic Active Pixel Sensors (MAPS) to be used in the Micro-Vertex-Detector of CBM. Together with the PICSEL group of IPHC Strasbourg, we aim to exploit those features by migrating the successful architecture of our sensors toward this novel technology. This work reports about our findings on the first prototypes manufactured with the new technology.

A weak point of CMOS sensors is the slow diffusion of signal charge in the undepleted active medium. A sufficient radiation hardness was only achievable with very small pixels, which do not provide the required readout speed. A few years ago, this obstacle was alleviated by the upcoming availability of CMOS processes providing a high-resistivity epitaxial layer of 1 kΩcm. It could be demonstrated that this increases the non-ionizing radiation hardness by more than one order of magnitude. Therefore pixels of this high-resistivity AMS-0.35-process having a pitch of $20 - 30$ µm achieved the design goal of a non-ionizing radiation hardness in the order of $10^{13}\ \mathrm{n_{eq}/cm^2}$ [1].

Using this technology, a first vertex detector based on CMOS sensors is taking data in the heavy-ion experiment STAR since 2014.

Achieving the required non-ionizing radiation hardness, the ionizing radiation hardness and read-out speed of sensors in the AMS-0.35-process were not sufficient for the application in modern vertex detectors, e.g. in ALICE and CBM. Therefore, a novel $TOWER - 0.18$ µm process was exploited and found to provide a higher tolerance to ionizing radiation [2]. Moreover, the smaller feature size allows for the integration of a more complex logic into the pixel providing a faster read-out. An additional feature of this process is the use of very high resistivity epitaxial layers up to 6 kΩcm. It was expected, that this would improve the non-ionizing hardness further, which would allow for larger pixels and therefore for a faster sensor readout.

To test this assumption, the prototype sensor MIMOSA-34 was designed, irradiated to $10^{13}\ \mathrm{n_{eq}/cm^2}$ and tested hereafter. The sensor provides elongated pixels with a pixel pitch between 22 µm × 33 µm and 33 µm × 66 µm. Figure 1 shows the response to photons of an Fe-55-source of the largest pixel. Its charge collection efficiency is

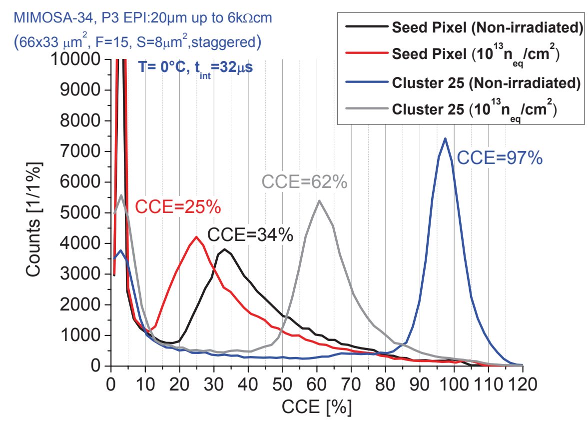

Figure 1: Signal response to photons after a radiation dose of $10^{13}\ \mathrm{n_{eq}/cm^2}$.

reduced by radiation damage from 34% to 25% for the seed pixel and from close to 100% to 62% for the charge of the full cluster. The signal to noise ratio, as measured with a Sr-90-β-source, decreases from 49 to 35. According to our experience with other sensors, this signal to noise ratio is sufficient to provide an excellent detection efficiency.

In conclusion, the novel process is likely to provide a tolerance to $10^{13}\ \mathrm{n_{eq}/cm^2}$ as needed for CBM even in combination with a 33 µm × 66 µm pixel pitch. Consequently, this pitch seems now limited by the need for matching a spatial resolution of 5 µm rather than by the radiation tolerance. The latter allows for increasing the pixel pitch of the vertex detector, which comes with significant advantages in terms of readout speed and reduced power consumption.

References

[1] D. Doering et al., Pitch dependence of the tolerance of CMOS monolithic active pixel sensors to non-ionizing radiation, Nuclear Instruments and Methods A, **730**, 111, 2013.

[2] D. Doering et al., Noise performance and ionizing radiation tolerance of CMOS Monolithic Active Pixel Sensors using the 0.18 µm CMOS process, Journal of Instrumentation, **9**(05) C0551, 2014.

* This work has been supported by BMBF (05P12RFFC7), HIC for FAIR and GSI.

An ultra-low material budget Cu-based flexible cable for the CBM-MVD *

P. Klaus[1], *J. Michel*[1], *M. Wiebusch*[1], *M. Koziel*[1], *T. Tischler*[1], *S. Schreiber*[1], *C. Müntz*[1], *J. Stroth*[1,2], *and the CBM-MVD collaboration*
[1]Goethe-Universität Frankfurt; [2]GSI, Darmstadt, Germany

The CBM Micro-Vertex-Detector (MVD) relies on employing a material budget x/X_0 per detector station of 0.3% (first station) to 0.5% (following stations) to allow for a secondary vertex resolution of better than 70 μm with typical pixel pitches of about 20 μm. To reach this ambitious goal, all components in the acceptance of the detector have to be challenged w.r.t. their impact on the material budget, while at the same time maintaining their cutting edge performance regarding mechanical and electrical properties as well as radiation hardness. In addtion, the sensor readout has to be robust with low noise occupancy, which puts strong constraints on the electrical properties of the rather long cables connecting the sensors with the front-end electronics (FEE) being outside the acceptance of the detector. Especially in the outer stations, substantial parts of those cables are placed inside the acceptance and hence contributes to multiple scattering. Those cables are flexible printed circuits (FPC) and provide power to the CMOS Pixel Sensors (CPS), allow to control them, and to read out the hits. The previous generation cable was not specifically optimized for ultra-low material budget being a two-layer copper-based cable with a layer thickness of about 25μm. It was successfully tested in a beamtime with the CBM-MVD prototype [1].

Reducing the dominant factor of the material budget meant reducing the thickness of the copper layer, see Tab. 1. The cable was redesigned with a readout to the side (see Fig. 1), a smaller feature size (80μm) and thus a reduced total cable width, and copper traces with a thickness of only 12μm. The cables were manufactured using a commercial technology offered by ILFA [2]

Some problems may arise from the ultra-thin layout though: Without an accompanying ground layer, the traces will not have an excellent controlled impedance. In addition, the resistance of the power supply lines becomes substantial. To compensate for this, their width was increased to 360 μm resulting in visible areas of higher material budget in Fig. 1. Dedicated tests with a new sensor test stand will evaluate the effect of the missing shielding and possible impedance mismatch of signal lines as well as the higher resistance of the power supply lines. This test stand comprises a compact, Peltier-based temperature control unit, and a readout chain using a special test mode of the sensor which makes it possible to measure transfer functions. This allows to deduce the temporal and fixed pattern noise of a reference sensor to conduct extensive systematic tests of flex cable generations.

* Work supported by BMBF (05P12RFFC7), HIC for FAIR and GSI

Layer	d [μm]	x/X_0	Si-equiv [μm]
Coverlay	26	0.009 %	8.6
Copper	40% · 12	0.033 %	31.3
Polyimide	25	0.009 %	8.2
Sum	63	0.051 %	48.1

Table 1: Material budget of the new cable.

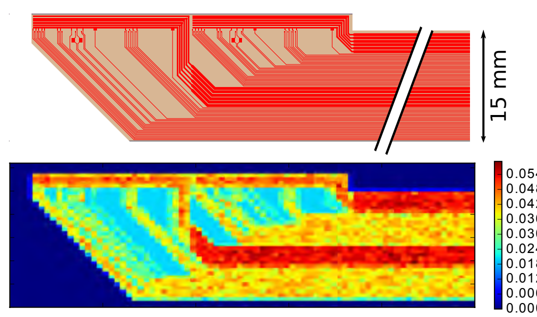

Figure 1: CAD layout of the new ultra-thin FPC showing the bonding zone and the part of the cable situated in the acceptance of the detector (top); an analysis of its material budget in % of x/X_0 (bottom).

Another possible approach to reach an even smaller material budget employs Aluminium instead of Copper for the conductive layer. Aluminium has a smaller conductivity (3.5010^7 S/m vs. $5.96 \cdot 10^7$ S/m) but at the same time a much longer radiation length (88.97 mm vs. 14.36 mm), suggesting an improvement of $\times 3.6$ smaller material-budget. The downside of this non-standard Aluminium-based technology is the lower production reliablity, and thus higher cost and production times.

To summarize, a new ultra-thin design of the FPC for the CBM Micro-Vertex-Detector was created and the cables produced. Its suitability will be analyzed including its electrical performance and integration stability. Further technologies to reduce the material budget even more are being evaluated.

References

[1] M. Koziel et al., The prototype of the Micro Vertex Detector of the CBM Exp., Nucl.Instrum.Meth. A732 (2013) 515

[2] ILFA Industrieelektronik und Leiterplattenfertigung aller Art GmbH, Hannover, Germany

PRESTO: PREcursor of the Second sTatiOn of the CBM-MVD*

M. Koziel[1], T. Tischler[1], C. Müntz[1], and J. Stroth[1,2] for the CBM-MVD collaboration[1]
[1]Institut für Kernphysik, Goethe-Universität, Frankfurt, Germany; [2]GSI Darmstadt, Germany

This report summarizes the activities undertaken to construct a precursor of a quadrant of the second MVD-station.

The PRESTO (PREcursor of the Second sTatiOn) project of the CBM-MVD addresses the double-sided integration of 15 MIMOSA-26 sensors (dummies and working sensors, 9 of these on the front in a 3×3 and 6 sensors on the back in a 2×3 arrangement) onto a 8×8 cm^2 CVD diamond carrier [1] featuring a thickness of 150 µm. The PRESTO module will employ new flex cables (FPC) [2] providing all signals needed to operate and read out the sensors (10 FPCs in total), see fig. 1.

To assembly this module, new sensor positioning jigs aiming for a sensor positioning precision with respect to the support and the neighboring sensors of below 100 µm were manufactured. To evaluate the integration concept, the RAL-247 adhesive [3] and the new jigs, a dummy PRESTO module has been assembled employing 50 µm thin MIMOSA-26 dummies and a 200 µm thin glass plate which serves as sensor carrier, see fig. 2.

In the process of gluing, the inclusion of air bubbles should be avoided due to the vacuum operation of the MVD and the use of thinned sensors. This triggered a study focusing on optimizing the preparation of the glue, its dispensing and the quality assurance of the results. The number of air bubbles introduced into the glue during its mixing process has been significantly reduced by degassing it in an exicator at about $4 \cdot 10^{-1}$ mbar for about 1 hour. However, this did not prevent the air bubbles to appear after the gluing of the sensors onto the carrier. The introduced air bubbles featured a size of about $100 - 300$ µm diameter. To verify their impact on the 50 µm thin sensor dummies, the cured module has been placed inside a small vacuum chamber which has been evacuated for about 48 hours to a value of $4 \cdot 10^{-1}$ mbar. The visual inspection of the sensor dummies using a high precision microscope did not reveal any mechanical damage. Further studies will be addressed with working sensors to check on-the-fly any possible correlation between sensor performance, pressure and bubble sizes.

The gluing of the dummy sensors onto the glass carrier demonstrated that a glue volume of $3 - 5$ µl (different glue volume used for each row of sensors) is sufficient to dispense a uniform and thin (about $10 - 17$ µm) layer underneath the sensors. The horizontal sensor-to-sensor distances were measured to be below 5 µm. The vertical variation in the distances between the sensor edges were measured to be of about 20 µm. The achieved precision is significantly below the envisioned one. Next steps comprise the establishing of procedures for the integration of the FPCs, the exercise of double-sided bonding and the verification of the vacuum compatibility.

*This work has been supported by BMBF (05P12RFFC7), EU-FP7 HadronPhysics3, HGS-HIRe, GSI and HIC for FAIR.

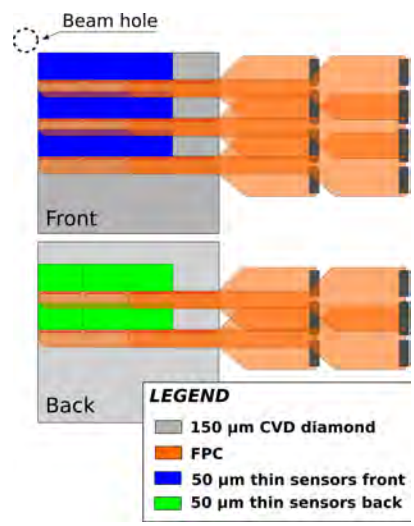

Figure 1: Sketch of the arrangement of the sensors and the FPCs with respect to the support carrier within the PRESTO module.

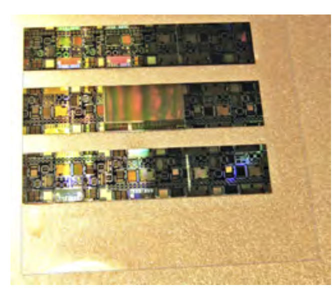

Figure 2: Assembled dummy module of PRESTO.

References

[1] Diamond Materials GmbH, Germany

[2] P. Klaus et al., "Ultra-low material budget Cu flex cable for the CBM-MVD. "GSI annual report 2014.

[3] Private communication, Simon Canfer Rutherford Appleton Laboratory, Composites and Materials Testing Group, UK.

The CBM-MVD: Progress in Mechanical Integration *

M. Koziel[1], *T. Tischler*[1], *C. Müntz*[1], *M. Deveaux*[1], *and J. Stroth*[1,2] *for the CBM-MVD collaboration*
[1]Institut für Kernphysik, Goethe-Universität, Frankfurt, Germany; [2]GSI Darmstadt, Germany

This report summarizes the activities undertaken towards the construction of the Micro Vertex Detector (MVD) of the Compressed Baryonic Matter (CBM) experiment.

Quality assurance of 50 µm thin PRESTO sensors: Thinned MIMOSA-26 sensors will be used for assembly the so called PRESTO module. PRESTO addresses the double-sided integration of 15 MIMOSA-26 sensors (dummies and working sensors) onto a 8×8 cm^2 CVD diamond support (see [1] for more details). Sensors will be connected with the R/O system by means of a newly designed ultra-low material budget flex cable employing commercially available processes based on copper traces [2]. Constructing the PRESTO allows to estimate the integration yield providing that the employed sensors are tested prior to assembly. Up to now, 18 MIMOSA-26 AHR sensors thinned to 50 µm were probe tested using the setup described in [3]. The setup allows testing the standard operation modes of the sensor as well as measure the fixed pattern and temporal noise by the means of so called s-curves. 12 sensors were found without a significant number of dead/noisy pixels; they were qualified as fully operational. Four sensors exhibiting some dead rows/columns were marked as faulty. The two remaining sensors were not operational due to a power supply short (one sensor) and problems while powering one out of the four MIMOSA-26 sub-matrices. The estimated yield was then of about 65% which is in agreement with expectations for this type of sensors [4]. The temporal noise was found to be of about 1.6-1.8 mV and the fixed patter noise of about 0.5-1.0 mV. This is by factor of 2-3 higher than the noise specified by a sensor provider. This was nevertheless as expected since the sensor power signals were generated outside the probe card. The addressed probe tests allowed also to establish test procedures required for non-destructive tests of thinned CMOS sensors and can be applied for testing the final MVD sensors.

Development of a custom made glue: An "ideal" adhesive for the integration of the sensors onto their supports should be easy to dispense in a thin and uniform layer—calling for a low viscosity—, radiation hard as well as flexible (to compensate for the thermal expansion mismatches between the sensor and their support material) within the temperature range foreseen for the operation of the MVD sensors. Since there are none "on-shelf" products that meet these requirements, a custom-made, two compound adhesive with a working name RAL-247 was manufactured at the Rutherford Appleton Laboratory (RAL), Composites and Materials Testing Group, UK. The glue features a glass temperature of -45 °C, a viscosity of below 100 mPa·s and a curing time of 48 h at +50 °C. To investigate its radiation hardness, RAL-247 samples were irradiated with X-rays to 100 Mrad and to a proton dose of about 10^{15} n_{eq}/cm ^{2}. The irradiated samples were sent to RAL for further Dynamic Mechanical Analysis tests which unraveled no significant change of properties [5] that confirms the expected radiation hardness at the range of radiation doses expected at the MVD.

Development of the heat sinks for the MVD: The operation of the MVD in vacuum requires a continuous cooling of the sensors to limit radiation induced defects as well as noise. To keep the material budget of the individual MVD station as low as possible, the cooling approach of the MVD employs highly thermal conductive sensor support materials (CVD diamond [6] and encapsulated high performance graphite) in the acceptance of the MVD and actively cooled aluminum-based heat sinks outside of this area. To evaluate the cooling concept and its vacuum compatibility, half-station heat sinks of the first three MVD stations were manufactured at COOLTEK GmbH. The heat sinks incorporate a buried cooling pipe and have thermally been simulated prior their manufacturing using a worst case scenario for the sensor power dissipation plus an additional safety factor of four. These heat sinks are currently being evaluated under laboratory conditions focusing on their vacuum compatibility [7]. The heat dissipation of the MVD sensors is provided by kapton insulated flexible heaters from OMEGA Engineering, INC.

References

[1] M. Koziel et al., "PRESTO: PREcursor of the Second sTatiOn of the CBM-MVD." GSI annual report 2014.

[2] P. Klaus et al., "Ultra-low material budget Cu flex cable for the CBM-MVD. "GSI annual report 2014.

[3] M. Koziel et al., GSI annual report 2013.

[4] L. Greiner et al., CPIX 2014, Bonn, Germany

[5] Private communication, Simon Canfer Rutherford Appleton Laboratory, Composites and Materials Testing Group, UK.

[6] Diamond Materials GmbH, Germany

[7] G. Kretzschmar et al.,"Vacuum compatibility of the CBM-MVD." GSI annual report 2014.

* This work has been supported by BMBF (05P12RFFC7), EU-FP7 HadronPhysics3, HGS-HIRe, GSI and HIC for FAIR.

Yield studies on a fully integrated sensor for the CBM-MVD*

B. Linnik[1], *D. Doering*[1], *M. Deveaux*[1], *and J. Stroth*[1,2] *for the CBM-MVD collaboration*
[1]Institut für Kernphysik, Goethe University Frankfurt, Germany; [2]GSI Darmstadt, Germany

The CBM-experiment will study the phase diagram of hadronic matter in the region of highest baryon densities by means of rare probes like open charm particles. Reconstructing those particles calls for a vertex detector providing a unique combination of excellent spatial resolution, light material budget and high rate capability. To match those requirements, we intend to use CMOS Monolithic Active Pixel Sensors, which are developed by the PICSEL group of IPHC Strasbourg and evaluated at the IKF Frankfurt within an common R&D project.
A first fully integrated sensor, MIMOSA-28, was developed in the AMS $0.35\ \mu\mathrm{m}$ CMOS process and it is used in the STAR-HFT since 2014. However, this sensor does not match the requirements of CBM regarding radiation tolerance and readout speed. Therefore, the sensor architecture was migrated to a novel $0.18\ \mu\mathrm{m}$ process. This process was found to provide a higher tolerance to ionizing radiation [1]. Moreover, its higher packing density allows for reading two lines in parallel, which accelerates the readout by a factor of two with respect to the elder design.
In 2014, a first fully integrated prototype sensor (FSBB-M0) was realized in the new process [2]. The sensor was realized in two flavors (FSBB-M0a and FSBB-M0b), which differ slightly in the dimensions of some transistors. It features 416×416 pixels of $22 \times 33\ \mu\mathrm{m}^2$ pitch and it is read out within $40\ \mu\mathrm{s}$ via a pair of discriminators at the end of each column. Hereafter, the digital data is zero-suppressed and sent out via two 320 Mbps digital links. The sensitive surface of the FSBB is $13.7 \times 9.2\ \mathrm{mm}^2$. The final sensor of the CBM-MVD will presumably consist of three FSBBs. The FSBB-M0 was tested at the CERN-SPS and provided a detection efficiency for minimum ionizing particles of $\gtrsim 99,5\%$, a noise occupancy of $\lesssim 10^{-5}$ and a spatial resolution of $< 5\ \mu\mathrm{m}$ in both dimensions [3], which matches the requirements of CBM.
To test the robustness of the design and to assess the production costs for the CBM-MVD, we measured the production yield of the FSBB. In accordance with our experience, we assumed that flaws due to production mistakes would turn into a measurable deterioration of the noise of the sensors. A total of 25 (17 FSBB-M0a and 8 FSBB-M0b) sensors was bonded on PCB and operated with a suited readout system. By measuring the transfer functions we revealed the temporal noise (TN) of the individual pixels and the fixed pattern noise (FPN), which is caused by the offset of the dark signal of the pixels.

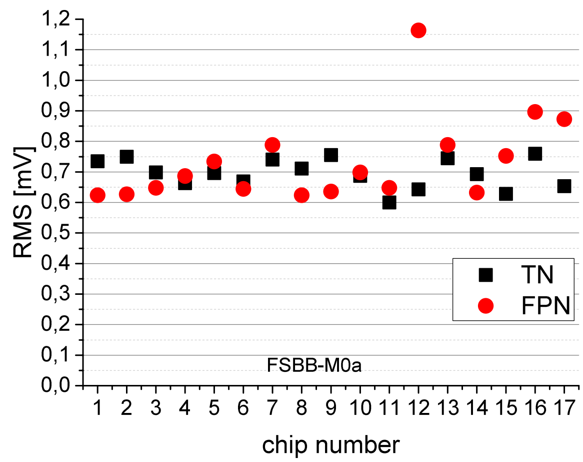

Figure 1: Temporal noise and fixed pattern noise measurement of all 17 FSBB-M0a chips.

The results of the study on the FSBB-M0a are shown in Fig. 1. We found all sensors tested to be operational and they provided a $\mathrm{TN} = (0.70 \pm 0.05)\ \mathrm{mV}$ and $\mathrm{FPN} = (0.73 \pm 0.14)\ \mathrm{mV}$. Only one of the tested sensors showed a higher FPN of $\sim 1.2\ \mathrm{mV}$, which might still be acceptable. Similarly good results were observed with the eight FSBB-M0b tested, which all found being operational (not shown).
We conclude that a first full size sensor meets the requirements of CBM with respect to surface size, data rate and spatial resolution. Moreover, the design mostly meets the specification in terms of readout speed. Measurements demonstrated that the sensor provides a good detection of minimum ionizing particles and the production yield was found to exceed 95%.

References

[1] D. Doering et al., Noise performance and ionizing radiation tolerance of CMOS MAPS using the $0.18\ \mu\mathrm{m}$ CMOS process, J. of I., 9(05):C0551, 2014.

[2] F. Morel et al., MISTRAL & ASTRAL: two CMOS Pixel Sensor architectures suited to the Inner Tracking System of the ALICE experiment, J. of I., 9(01):C01026, 2014.

[3] M. Winter, Private communication.

*This work has been supported by BMBF (05P12RFFC7), HIC for FAIR, HGS-HIRe and GSI.

The CBM MVD read-out electronics*

M. Wiebusch[1], J. Michel[1], M. Koziel[1], B. Milanovic[1], S. Amar-Youcef[1], P. Klaus[1], J. Stroth[1,2], and the CBM-MVD collaboration

[1]Goethe-Universität Frankfurt; [2]GSI, Darmstadt, Germany

Electronics

The CBM Micro-Vertex-Detector (MVD) front-end electronics serve as an intermediating device between the Monolithic Active Pixel Sensors (MAPS) and the DAQ system (based on the TRB3 system developed by HADES). In the current connection scheme, one TRB3 FPGA board can support up to 16 sensors of type "MIMOSA-26" in parallel. The front-end electronics are necessary to supply the sensors with electrical power and to convert between different digital signal standards. The central element of these custom-built PCBs is the converter board. In addition to remote controlled power supplies, signal switches and drivers, it features an ADC section to monitor the sensor's momentary electrical parameters. The sensors have to be supplied with a sensitive external biasing voltage, the so-called clamping voltage, which gets distributed to all sensor pixels. Several generation and distribution schemes were implemented to investigate which setup results in the best noise performance.

Measurements

The MIMOSA-26 provides a test mode to measure the discriminator transfer function[1] of all pixels. The slope steepness is directly related to the temporal noise of the sensor. The read-out sytem was extended to operate and read out the sensor in this test mode. The recorded data is evaluated by a dedicated ROOT-based analysis software. Noise tests with MIMOSA-26 are ongoing. However, preliminary results concerning the influence of the clamping voltage suggest that it is beneficial to generate this reference voltage as close to the sensor as possible and to use decoupling capacitors, if possible, next to the bonding pads on the flex print cable. These results are in particular important for the development of the next generation of cables[2]. Furthermore, the ADC section on the converter board can be used to perform systematic scans in order to characterize the sensors. As an example of such an automatic scan, Fig. 1 shows the dependence of the sensor's current consumption on the discriminator threshold setting.

Laboratory instrumentation

When characterizing sensors, it is desirable to investigate the temperature dependence of certain sensor parameters. Until recently, such tests were conducted using a large cooling system which circulates coolant through a cooling block to which the sensors under test are attached. The sensors are now operated on a small copper platform which is cooled with a peltier element. A PID controller implemented on a microcontroller senses the temperature of the platform by means of a onewire temperature sensor and regulates the current through the peltier element. The device features a small display and a simple user interface, alternatively it can be remote controlled via a USB connection. The platform can be cooled down to circa $-10°C$ within few minutes while consuming 50 W. Overall, the set-up was greatly reduced in size, while at the same time improved in usability.

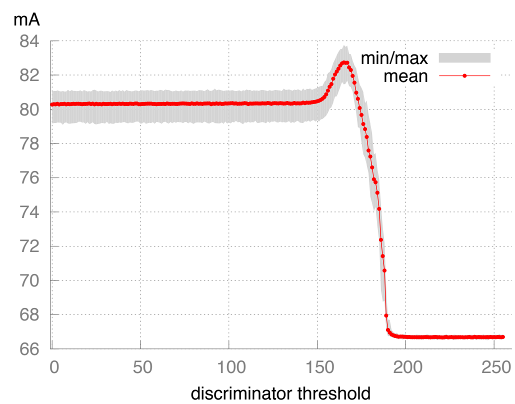

Figure 1: The current consumption (digital VCC) of a MIMOSA-26 sensor as a function of the discriminator threshold. Data acquired with front-end electronics onboard monitoring devices.

PRESTO

Current activities focus on bulding a prototype[1] of a quadrant of the second station of the MVD. For now, MIMOSA-26 sensors are used in this project though they do not qualify to be used in the final detector. Parts of the front-end electronics are currently redesigned to fit the spacial constraints of the set-up.

References

[1] M. Koziel, T. Tischler et al., PRESTO: PREcursor of the Second sTatiOn of the CBM-MVD, this issue.

[2] P. Klaus et al., Ultra-low material budget Cu-based flexible cable for the CBM-MVD, this issue.

* Work supported by BMBF (05P12RFFC7), HIC for FAIR and GSI

[1] The firing probability of a binary pixel as a function of discriminator threshold; usually has the form of a sigmoid function.

Silicon Tracking System

Improvement of ultra-light microcables production at LTU for the CBM Silicon Tracking System

V.M.Borshchov[1], *I.T.Tymchuk*[1], *C.J.Schmidt*[2], *V.G.Kucherenko*[1], *G.I.Nikitskiy*[1], *J.M.Heuser*[2], *M.A.Protsenko*[1], *J.Eschke*[2,3], *R.A.Kushniruk*[1], *L.V.Klimova*[1], *and K.M.Liholitova*[1]

[1]LED Technologies of Ukraine (LTU) Ltd, Kharkov, Ukraine; [2]GSI, Darmstadt, Germany; [3]FAIR, Darmstadt, Germany

Ultra-light micro-cables are the key component for the CBM-STS. They are employed to realize the analogue signal interconnection between detector and readout for the STS at minimized material budget. Taking into account the complexity of micro-cables and their required quantity a few "bottlenecks" in the production line have been identified and improvements were realized on the production line. Additionally the preliminary technological regimes were defined and a test batch of micro-cables (100 pieces) was manufactured within the framework of the STCU partner project P635.

For the detector modules two kinds of interconnection components will be employed [1-2]:

- ultra-light interconnection microcables based on aluminium-polyimide adhesiveless dielectrics (connecting microcables, interstrip cables, daisy-chain cables, shielding layers).
- meshed spacers based on Kapton or polyimide (narrow and wide meshed spacers).

The typical technological process of micro-cable and spacer manufacturing includes the following main technological operations based on photolithography and chemical wet etching processes: chemical cleaning of the substrate, photoresist coating on the substrate, photoresist exposure, photoresist development, aluminium etching (for interconnecting micro-cables), polyimide etching and finally photoresist removal.

Taking into account that large numbers of components in a considerable design variety need to be produced for the CBM STS (about 58 thousand micro-cables and spacers) the available technological equipment and the production line were analyzed with the aim to identify possible production "bottlenecks" which might result in production yield issues or even a suspension of production. The available equipment allows to produce the required components but two "bottlenecks" were identified:

- equipment for photoresist coating needed duplication,
- an exposure unit for photoresist exposing needed to be duplicated.

The following equipment was in consequence supplied by GSI to LTU Ltd within the STCU partner project, both from Bungard Elektronik, Germany:

- a Dip Coater RDC 21-K type,
- a parallel beam exposure unit EXP8000.

The equipment was installed and tuned in the clean room at the cable production site in Kharkov (Fig. 1). Process parameters for the operation of these machines for the different types of components were investigated and preliminary regimes were chosen.

Based on these parameters, a first pilot batch of microcables was produced and delivered to GSI so that the module assembly processes could be elaborated (48 laminated and 52 non-laminated test microcables 11 cm and 21 cm long). Samples of test cables are depicted in Fig. 2. The cable production line at LTU has been strengthened towards the large scale serial production of micro-cables for the CBM-STS. Technological regimes on the newly installed equipment were investigated and a batch of test microcables produced. This is a starting point for further production process optimization towards yield.

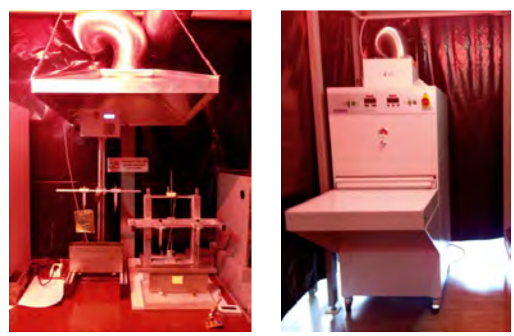

Figure 1: Dip coater RDC 21-K (left) and exposure unit EXP8000 (right) installed at LTU.

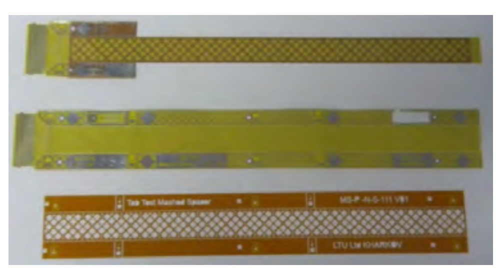

Figure 2: Experimental micro-cables for the development of the TAB-bonding assembly steps at GSI.

References

[1] V.M. Borshchov et al., CBM Progress Report 2013, p. 41

[2] C.J. Schmidt et al., CBM Progress Report 2012, p. 18

Manufacturing detector modules for the CBM Silicon Tracking System

V.M. Borshchov[1], Yu.A. Murin[2], C.J. Schmidt[3], M.A. Protsenko[1], I.T. Tymchuk[1], J.M. Heuser[3], R.A. Kushniruk[1], N.F. Chernikova[1], L.V. Klimova[1], and M.S. Tykhomirova[1]

[1]LED Technologies of Ukraine (LTU) Ltd, Kharkov, Ukraine; [2]JINR, Dubna, Russia; [3]GSI, Darmstadt, Germany

Based on the new module assembly concept [1] and its preliminary test on the first half-detector module mock-up [2], three types of detector modules were developed and 18 module mock-ups manufactured to verify the technical approach. The module mock-ups allowed specifying their exact composition, defining nomenclature and marking of components, and the work-off of the assembly procedure. The work, coordinated by JINR, was co-funded through the BMBF-JINR project 5.2 "Development of ultra-low-mass silicon micro-strip detector systems for precision tracking in high-energy heavy-ion collision experiments" with project partners at GSI and JINR.

The detector module mock-ups have been developed according to the composition of the smallest STS ladder comprising 6 modules:

- 2 double-sensor modules with sensor-to-FEB distance 111 mm (one left and one right type),
- 2 single-sensor modules with sensor-to-FEB distance 212 mm (one left and one right type),
- 2 single-sensor modules with sensor-to-FEB distance 252 mm (one left and one right type).

Each module mock-up includes following components:

- one or two dummy sensor with interstrip cable;
- multilayered connection microcables;
- dummy chips;
- dummy FEBs.

For sensor-to-FEB connection [1,2] following components are foreseen:

- eight multilayered microcables (128 lines for chip to sensor connection). Each multilayered cable includes two connecting layer (FDI-A-24, 64 traces at 113 μm pitch) and eight meshed spacers (Kapton 50 μm thick).
- overall meshed spacer for all 8 multilayered microcables (two Kapton spacers 50 μm thick).
- overall shielding layer for all 8 multilayered microcables (FDI-A-24) with glued meshed spacer (Kapton 50 μm thick).

Taking into account abovementioned types of components for each module from 16 to 19 types of components were developed and produced. Also was defined following nomenclature and marking of components for further production:

1. AC-P-S-T- *- analog cable, P-side, short, top
2. AC-P-L-T- *- analog cable, P-side, long, top
3. AC-P-S-B- *- analog cable, P-side, short, bottom
4. AC-P-L-B- *- analog cable, P-side, long, bottom
5. AC-N-S-T- *- analog cable, N-side, short, top
6. AC-N-L-T- *- analog cable, N-side, long, top
7. AC-N-S-B- *- analog cable, N-side, short, bottom
8. AC-N-L-B- *- analog cable, P-side, long, bottom
9. SL-P- *- shielding layer, P-side
10. SL-N- *- shielding layer, N-side
11. MS-P-N-S- *- meshed spacer, P-side, narrow, short
12. MS-P-N-L- *- meshed spacer, P-side, narrow, long
13. MS-N-N-S- *- meshed spacer, N-side, narrow, short
14. MS-N-N-L- *- meshed spacer, N-side, narrow, long
15. MS-P-W- *- meshed spacer, P-side, wide
16. MS-N-W- *- meshed spacer, N-side, wide
17. ISC-**- interstrip cable,
18. DCC-P- daisy-chain cable, P-side,
19. DCC-N- daisy-chain cable, P-side

* *base sensor-to FEB distance (111, 212, 252 mm)*
** *length of sensor (42, 62 mm)*

Example of cable marking: AC-N-S-T-111 = analog cable, N-side, short, top with sensor-to-FEB distance 111 mm.

According to the above mentioned composition of STS ladder, modules and multilayered connection microcables for three types of modules (111, 212, 252 mm) about 100 photomasks were developed and produced. Using those photomasks for 18 modules more than 1300 microcables and spacers (about 70 components for one module) were manufactured. Six types of assembled modules are depicted in Fig.1. The mock-ups of the detector modules (6 pcs) will be used to assemble the first mock-up of a full-scale ladder [3].

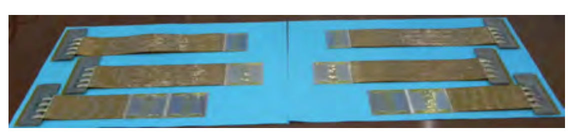

Figure 1: Detector module mock-ups.

References

[1] V.M. Borshchov et al., CBM Progress Report 2013, p. 41
[2] C.J. Schmidt et al., CBM Progress Report 2012, p. 18
[3] V.M. Borshchov et al., The first mock-up of the CBM STS full-scale ladder, this report

The first mock-up of a CBM-STS full-scale ladder

V.M. Borshchov[1], N.F. Chernikova[1], V.V. Elsha[1], V.G. Kucherenko[1], Yu.A. Murin[2], G.I. Nikitskiy[1], M.A. Protsenko[1], and I.T. Tymchuk[1]

[1]LED Technologies of Ukraine (LTU) Ltd, Kharkov, Ukraine; [2]JINR, Dubna, Russia

The first mock-up of the CBM STS ladder has been developed and manufactured by the Kharkov team at the assembly site of LTU Ltd (Figs. 3 and 4). The ladder mock-up was developed for verification of ladder assembly route [1,2]. The work was funded and coordinated by JINR.

The ladder mock-up includes the following components, similar as in real full-scale ladder (Fig. 1):

- mock-ups of silicon strip modules (6 pcs) [3];
- containers for the FEBs (2 pcs);
- carbon fiber frame (CF-frame) on the support units (1 pc).

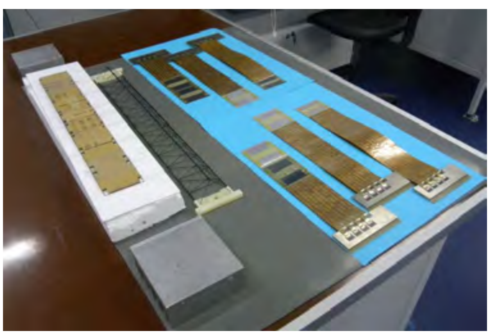

Figure 1: Components of the ladder mock-up.

For the assembly of the ladder mock-up, the sequence of work steps has been developed. It includes following steps:

- mounting and fixation of double-sensor modules #1 and #2 to jig (Fig. 2);
- mounting and fixation of single-sensor modules #3 and #4 with the necessary overlapping of sensors to fixture;
- mounting and fixation of single-sensor modules #5 and #6 with the necessary overlapping of sensors to fixture;
- mounting and fixation of CF-frame to fixture;
- gluing of sensor holders to sensors and CF-frame. Glue polymerization;
- mounting of the FEB mock-ups in the container on thermal paste;
- turning of containers with the FEBs by 90 degree.

The assembled mock-up is depicted in Figs. 3 and 4. The completed work allows us to conclude on the feasibility of the previously selected design ladder for the CBM STS.

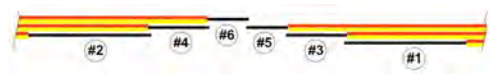

Figure 2: Diagram of sensor overlap.

The obtained results will be used for the clarification of technical tasks for sthe pecialists of PLANAR for designing and manufacturing of the optical-mechanical assembly tools. Further efforts of should be aimed at the clarification of the ladders composition, applied materials and geometrical dimensions of all ladder components.

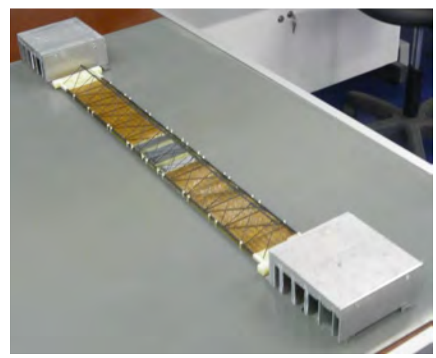

Figure 3: First mock-up of the CBM STS ladder.

Figure 4: Team at the assembly site of LTU Ltd.

References

[1] Workshop on module and ladder components production and assembly for the CBM Silicon Tracking System, LTU Ltd, Kharkov, Ukraine, 14-17 January 2014.

[2] Workshop "From Consortium to Cooperation", LHEP JINR, Russia, 1-3 October 2014.

[3] V.M. Borshchov et al., Manufacturing detector modules for the CBM Silicon Tracking System, this report

A scalable neutron source for detector radiation hardness test*

E. Friske[1] *and H. R. Schmidt*[1,2]
[1]Universität Tübingen, Tübingen, Germany; [2]GSI, Darmstadt, Germany

Silicon detector radiation hardness

During operation of the STS, the silicon strip detectors are expected to be irradiated with large numbers of neutrons, some sectors in excess of 10^{12} n_{eq}/cm^2/month [**?**], with an accumulated dose of 10^{14} n_{eq}/cm^2 [**?**].
To test detector performance and particularly changes in the semiconducting properties due to neutron induced activation, a neutron source with high flux is necessary. Unfortunately, reactors with sufficient neutron flux are heavily occupied. This leads to irradiation campaigns with very short irradiation times (in the order of minutes) in which the desired neutron dose is achieved [**?**].
To get a more realistic representation of the irradiation process, an exposure of days or weeks with defined annealing phases is more desirable. To fulfill these goals a scalable neutron source with good accessibility is required.

Neutron source

Present source The current neutron source consists of a gas cell filled with deuterium gas under a pressure of a few bar. A 2 MeV deuteron beam from the Rosenau accelerator passes an entrance window of a few microns thickness to induce deuterium fusion. However, even at this thickness the heat load on the entrance window reduced it mechanical stability, limiting both the beam current and the pressure of the gas cell.
Due to the limitations of both the accelerator and the window currently the neutron production is limited to a rate of $\approx 10^{12} n_{eq}/cm^2$/week. As this rate is about two orders of magnitude below the required total dose, it would take way too long to accumulate with the current setup. To solve these issues, a new gas cell is currently being manufactured, based on [**?**].

Cryogenic source The new neutron source currently in production consists of a steel endcap for the accelerator beam pipe. Mounted inside the endcap is the actual cell, cooled by liquid nitrogen. In contrast to [**?**], the gas cell is cooled by a copper finger reaching into a liquid nitrogen dewar. The entrance window is fixed to a thick copper disk sealing off the gas cell. (A technical sketch is shown in Fig. 1.)
This setup has several advantages over the present cell: The enclosed deuterium gas is more dense by a factor of 4 compared to room temperature, and the lower ambient temperature should increase the durability of the entrance window, allowing higher beam currents.

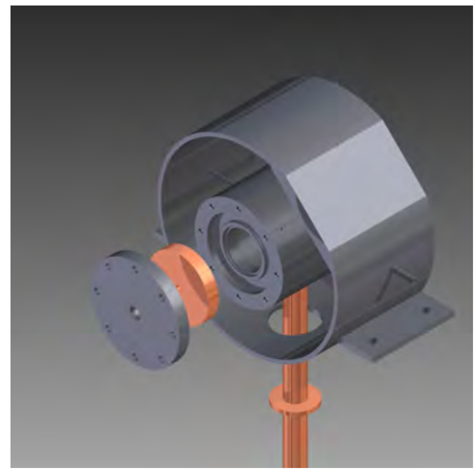

Figure 1: Schematic view of the cryogenic source

Combining these effects, it should be possible to increase both beam current and beam energy (to the accelerator's limit), which both significantly increases the neutron yield. In addition, the detector can be put within a few cm of the gas cell, providing maximum solid angle coverage. These improvements should increase the neutron flux by at least one order of magnitude, but the actual gain has to be determined once the cryogenic source is operational.
Before the new source can be put into operation additional tasks have to be performed, including tests of possible window materials and the cooling system.

* Work supported by GSI(CBM).

Development of laser test system for the characterization of double-sided silicon micro-strip prototype sensors *

P. Ghosh[†1,2], *J. Eschke*[3], *W. Niebur*[2], *and P. Zumbruch*[2]

[1]Goethe University, Frankfurt am Main, Germany; [2]GSI Helmholtz Center for Heavy Ion Research GmbH, Darmstadt, Germany; [3]Facility for Anti-proton and Ion Research GmbH, Darmstadt, Germany

For the characterization and quality assurance (QA) of prototype sensors produced for the Silicon Tracking System (STS) at the Compressed Baryonic Matter Experiment (CBM), a semi-automated infra-red pulsed Laser Testing System (LTS) has been developed [1]. The aim is to investigate performance and characterize properties of the prototype sensors. These characterization utilizes an infra-red laser. Focused and calibrated beam of photons are injected locally to the inter-strip region for understanding charge sharing and investigate uniformity of sensor performance. Two prototype sensor namely, CBM02 (double-sided, 256 strips/side, pitch = 50 μm, full read-out) and CBM05 (double-sided, 1024 strips/side, pitch = 58 μm, one-fourth read-out) has been investigated in the LTS [2]. The strips on the sensors are read-out via self-triggering n-XYTER based front-end electronics.

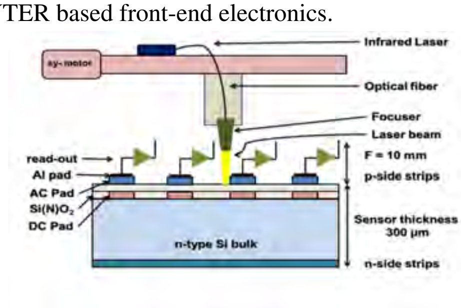

Figure 1: Schematic representation of the laser set-up

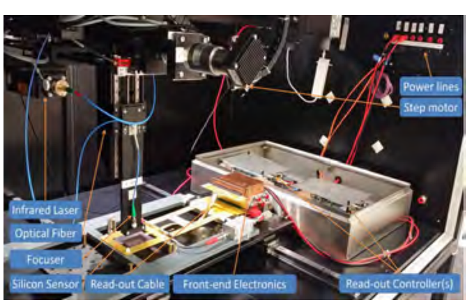

Figure 2: Components of Laser Test Stand characterizing a silicon detector module

The automatized characterization and quality assurance in a controlled manner at several positions across the sensor. The laser beam is focused to a spot-size of $(\sigma_{spot}) \approx$ 12 μm. The duration ($\sim$ 5 ns) and power (few mW) of the laser pulses are selected such that the absorption of the laser light in the 300 μm thick silicon sensors produces about 24000 electrons, which is similar to the charge created by minimum ionizing particles (MIP). The wavelength of the laser is chosen to be 1060 nm because the absorption depth of infra-red light with this wavelength is of the order of the thickness of the silicon sensors [3]. Fig. 1 shows the measurement set up in a schematic view. Fig. 2 shows various components installed with in the laser test stand. The laser beam is transmitted through a 6 μm thick optical fibre to a single focusing system, which focuses the light to a spot of about 12 μm diameter and the working distance is about 10 mm [1]. The laser focuser is calibrated to a focused position above the sensor surface as a function of the number of strips fired with a signal just above threshold. With this measurement the proper focus distance has been achieved. Fig. 3 shows one such measurement of charge sharing function (η) in the inter-strip region. The η function is defined as ratio of charge collected by either strip to the sum of both. The EPICS device control is used to control the step motor. A special program with a user interface has been developed operate and step over the active area to make several measurements automatically. Data acquisition software (DABC), the EPICS position information for data acquisition, logging and further analysis is performed using Go4 analysis tool.

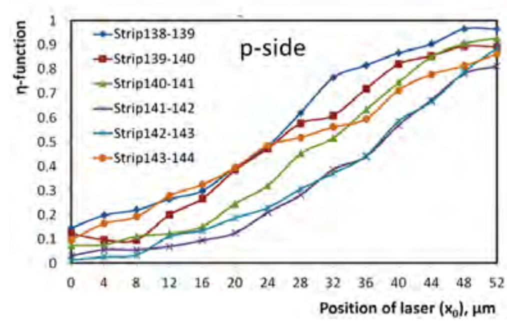

Figure 3: Charge sharing as a function of position of laser spot on p-side of the sensor

References

[1] P. Ghosh, PoS (Bormio 2013) 018, 2013

[2] P. Ghosh, J.Phys.: Conf. Ser. 503 012028, 2014

[3] P.O'Connor *et al.*, Proc. of SPIE Vol. 6276 62761W-1, p.2

* Work supported by HIC-for-FAIR, H-QM and HGS-HIRe

† Pr.Ghosh@gsi.de

Non-invasive quality assurance methods using infra-red laser for silicon micro-strip sensors for the CBM experiment *

P. Ghosh† [1,2]

[1]Goethe University, Frankfurt am Main, Germany; [2]GSI, Darmstadt, Germany

Silicon tracking system (STS) at the CBM experiment is aimed to reconstruct the trajectories of the hundreds of charged particles created in a central heavy-ion collision, and to determine their momenta with a resolution of around Δp/p $\approx$1. This precision is prerequisite for high-resolution mass measurements of e.g. rare probes and implies a thin detection system, with high-resolution space-point measurement and capable of readout rates up to 10 MHz. The STS will comprise of 1220 silicon sensors and out of which 896 detector modules will be construct to detect and track charge particle in the CBM environment [1]. The quality assurance (QA) tests procedures are developed for prototype double-sided silicon micro-strip sensors. These tests can be either invasive or non-invasive in nature. This yields in a database where one can identify sensors or detector modules with certain characteristics and grade them according to their performance.

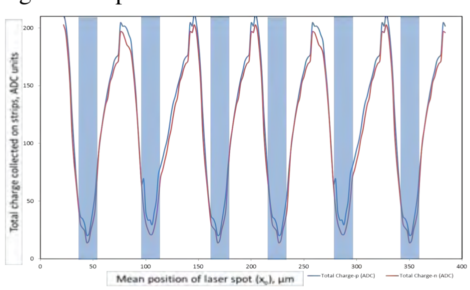

Figure 1: Uniformity and amplitude response of various strips from a detector module (strip positions are shaded)

Invasive methods - characterization and investigation of performance based on methods which require physical contact of probes to the sensor or detector module. The pros and cons are: (i) detailed analysis of the device under test (DUT), (ii) leaves scratches or marks on the surface, (iii) limited to sensors and non-viable to test detector modules and (iv) method involves passive electrical measurements using a wafer prober and micro-probing needles for QA [2].

Non-invasive methods - characterization and investigation of performance based on methods which do not require physical contact of probes to the sensor or detector module. The pros and cons are: (i) important parameters of the DUT can be investigated, (iii) leaves no scratches or marks on the surface, (iii) not limited to sensors and also viable to test detector modules and (iv) method involves injection of localized charge using a pulsed infra-red laser for QA [3].

* Work supported by HIC4FAIR, HGS-HIRe and H-QM

† Pr.Ghosh@gsi.de

The laser test stand (LTS) is developed with an idea to perform key quality assurance tests on silicon detector modules. The significant parameters that could be analysed or investigated using the LTS are: (i) Uniformity of charge collection (or strip integrity) from scanning the strips (see Fig. 1), (ii) Operational Voltage from the bias scan (see Fig. 2), (iii) Charge coupling to neighbour and next neighbour strips from bias scan (see Fig. 2 (a)) and (iv) Ratio of AC-coupling to inter-strip capacitance from amplitude response at specific positions (see Fig. 2 (b)).

Above discussion and example results clearly explains how an infra-red laser could be used to assure quality of the silicon micro-strip sensors in an non-invasive way.

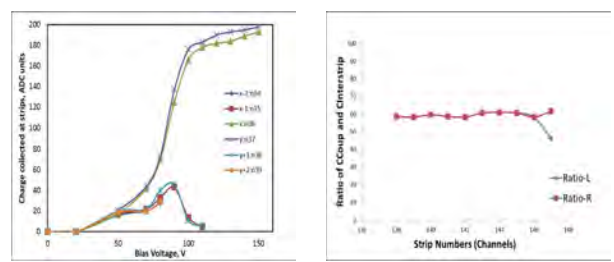

(a) (b)

Figure 2: a) Operating voltage determination and charge sharing between neighbouring and next to neighbouring strips and b) Ratio of coupling to inter-capacitance.

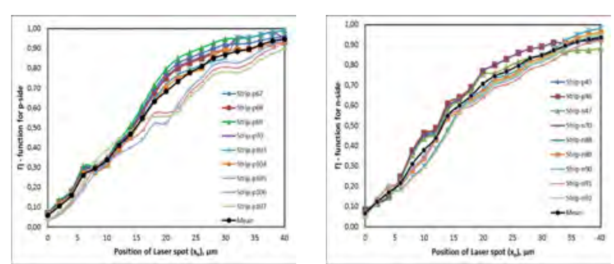

(a) (b)

Figure 3: Charge sharing measurements in the inter-strip region of a silicon detector module: a) p-side and b) n-side.

References

[1] P. Ghosh, for CBM coll. J.Phys.: Conf. Ser. 503 012028, 2014

[2] P. Ghosh, for CBM coll. PoS (Bormio 2013) 018, 2013

[3] P. Ghosh, CBM Progress Report 2013, Darmstadt 2014, p.48

[4] P. Ghosh, CBM Progress Report 2014, Darmstadt 2015

Design and prototyping of a carbon fiber support frame for the central ladders of the CBM Silicon Tracking System

S. Igolkin[1], *S. Belogurov*[2], *A. Chernogorov*[2], *A. Kolosova*[2], *Yu. Murin*[3], *and A. Semennikov*[4]
[1]CERN, Geneva, Switzerland; [2]JIEP, Moscow, Russia; [3]JINR, Dubna, Russia

The ladders of the STS placed in the central part of the station have to be specially designed to pass through the beampipe. The original concept of the beampipe was optimized to conduct experiments at SIS 300 and at SIS 100 with the energy of the incident gold ions above 8 AGeV. Further development of the CBM@SIS100 physical program required tuning of the setup to work with the energy of incident gold ions lowered down to 4 AGeV. The principal change of experimental conditions at low energies relevant to the beampipe and central ladders design is higher multiple scattering of gold ions inside the target. At present, there is no single reliable parameterization of multiple scattering of heavy ions at wide angles. The CbmRoot (Geant3), Geant4, and FLUKA codes provide a possibility to simulate this process, but since they give different results, the most conservative estimate (3.2 degrees at 4 AGeV given by GEANT4) was used for definition of the beampipe opening angle. The original design of the central ladder suitable for the beampipe with a 1.6 degree opening angle is shown in Fig. 1.

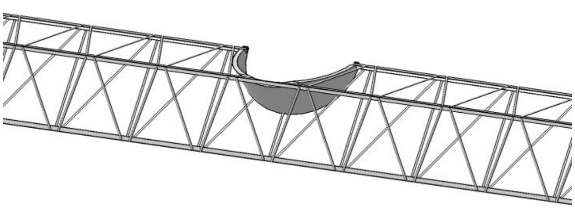

Figure 1: Design of the CF frame of central ladder.

One can see that the middle rib of the carbon fiber (CF) frame is not broken thus providing the necessary rigidity of the construction. The 3.2 degrees opening angle for the beampipe is not compatible with the original design of the central ladder CF frame. One has to increase the diameter of the cylindrical insert by a factor of two. The new type of the central ladder with a 118 mm diameter of the cylindrical part has been designed and built. Figure 2 shows the overall view of such a ladder, the components of the central ladder are shown in Figure 3. In Fig. 4 a mold is presented used in the manufacturing the ladder. The ladder obtained has the necessary rigidity at the mass of the cylindrical part of 5 g. Depending on the result of the ongoing simulations, the mass of the cylindrical part can be reduced by removing the excess material in the regions with low mechanical stress.

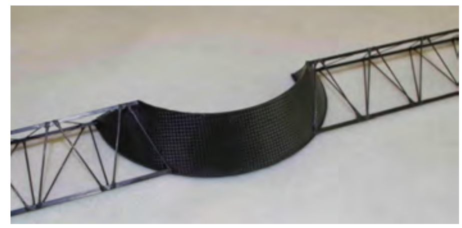

Figure 2: Prototype CF frame of a central ladder.

Figure 3: Components of the prototype CF frame.

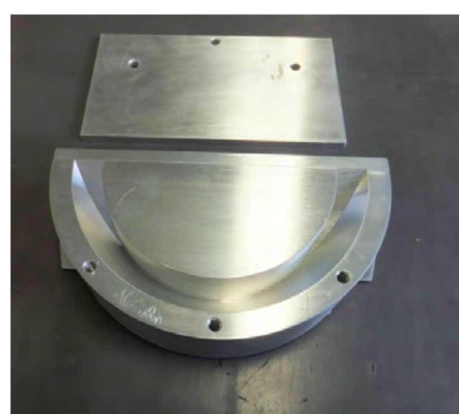

Figure 4: Mold for the production of the CF frames.

Towards the STSXYTERv2, a silicon strip detector readout chip for the STS

K. Kasinski, R. Kleczek, R. Szczygiel, P. Grybos, and P. Otfinowski
AGH University of Science and Technology, Cracow, Poland

STS-XYTER as a 128+2 channel full-size prototype IC dedicated for silicon strip detector readout for the STS was fabricated in 2013 [1]. Fig. 1. presents the test PCB developed at AGH used for functional verification. It provides on-board 5 separate power domains with dedicated low-noise LDO regulators, ERNI connector for sensor attachment, interconnects for test interface, test points and AC-coupled CBMnet interface (HDMI connector). The board is controlled by SysCore V3 (CBMnet) and NI FPGA (test interface) cards.

Figure 1: Test PCB for the STSXYTER ASIC.

The architecture details of the chip and test results were presented and published in [2]. Detailed tests using silicon sensors (e.g. CBM05) are currently being prepared. Using the same setup it was possible to further evaluate the chip. Fig. 2. shows the thermal image of the STS-XYTER chip on the test PCB. The thermal resistance was estimated to be approx. 52 °C/W, but it needs to be verified on the final FEB board in the environment similar to the final application as well. The temperature coefficients measured for various biasing points of of the ASIC evaluated for ambient temperatures of 7–85 °C are:

ADC_vdiscr_ref = -0.622 mV/°C,
ADC_ibias_corr = -0.312 mV/°C,
BG_iref = +0.154 mV/°C,
ADC_vref_n = -0.366 mV/°C,
ADC_vref_p = +0.286 mV/°C,
DISCR_bias_t = -0.435 mV/°C.

The STSXYTERv2 which will be an evolution of the STSXYTER prototype ASIC among the small fixes the changes include:

- new concept of the digital back-end (focused on the use of GBTx chip as a data concentrator), reaching hit bandwidths 9.4–47 MHit/s/chip,
- definition of the new communication protocol optimized for the conditions and requirements of the CBM experiment. The preliminary protocol was published [3] and is currently a subject of fine-tuning,
- configurable front-end (gain, bandwidth) for possible support of gas detectors (MUCH),
- new pad layout supporting quality test with pogo-probes and reduced connectivity required for regular operation,
- testability and temperature stability improvements of the in-channel ADC,
- further optimization of the analog front-end towards lower noise and better stability.

The STS-XYTERv2 ASIC is currently being under development. It is expected to be taped-out in Q2 of 2015 via Europractice services.

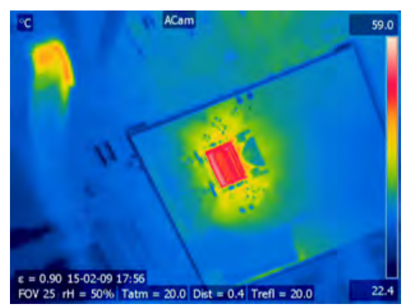

Figure 2: Thermal imaging of the operating ASIC on the test board.

Acknowledgment

We would like to thank the colleagues from GSI and WUT Warsaw for the efforts towards verification and specification of the new requirements.

References

[1] P. Grybos *et al.*, "STS-XYTER - a prototype silicon strip detector readout chip for the STS", CBM Progress Report 2012, Darmstadt 2013, p. 17.

[2] K. Kasinski *et al.*, "STS-XYTER, a High Count-Rate Self-Triggering Silicon Strip Detector Readout IC for High Resolution Time and Energy Measurements", IEEE NSS/MIC, 2014.

[3] K. Kasinski, W. Zabolotny, R. Szczygiel, "Interface and protocol development for STS read-out ASIC in the CBM experiment at FAIR", Proc. SPIE 9290, doi: 10.1117/12.2074883.

Long-term stability of the STS prototype sensors irradiated to 2×10^{14} n_{eq}.

P. Larionov[1]
[1]Goethe Universität, Frankfurt, Germany

The Silicon Tracking System (STS) is the core tracking detector of the Compressed Baryonic Matter (CBM) experiment. The STS silicon sensors [1] will be operated during long periods of time continuously. During the operation a high level of radiation damage is expected to impact on the sensors. The exposure of 1×10^{14} in 1 MeV neuton equivalent is the harshest scenario for sensors in the innermost, close to the beam areas of the STS stations after several years of running. In this work, the long-term stability of the leakage current of highly irradiated prototype sensors have been investigated.

Prototype sensor	Vendor	Sensor size, cm	Interconnection technology
CBM05H4	Hamamatsu	6.2×4.2	Double-Metal
CBM05H4	Hamamatsu	6.2×4.2	External cable
CBM05C6	CiS	6.2×6.2	Double-Metal
CBM06C4	CiS	6.2×4.2	External cable

Table 1: Prototype sensors used for tests.

To study the impact of irradiation on the properties of sensors, the latest STS prototype sensors have been irradiated to 2×10^{14} n_{eq} cm^{-2} at KIT, Karlsruhe. The following prototype sensors with two different strip interconnection technologies [1], indicated in the Table 1, were used for tests. All the measurements were performed at -5°C to reproduce the real operating conditions of the CBM experiment. Sensors were placed inside the shielded box with connected N_2 supply to keep the humidity at the lowest possible level. During a single measurement, the leakage current of the sensor at 350 V reverse bias voltage applied, and the temperature and humidity of the surrounding air were monitored with the step of 30 seconds. Figure 1a indicates the measurement result of the CBM06C6 sensor prototype during 15 days of continuous operation. The temperature of the air fluctuated within 1°C periodically during the measurement because of the cooling device operating principle, keeping the mean value of - 5.5° C.

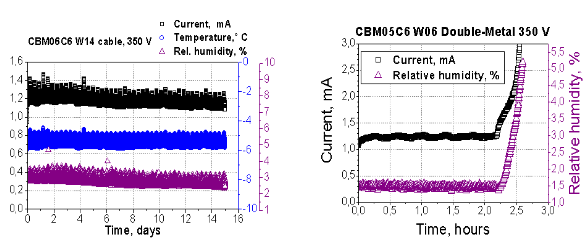

(a) (b)

Figure 1: a) Long-term stability of the leakage current of the CBM06C6 prototype sensor; b) Measurement results of the humidity impact test.

$$I(T) \propto T^2 exp(-E_g/2k_BT) \quad (1)$$

This resulted in a leakage current value fluctuation due it's temperature dependance that is shown in Eq. 1. Moreover, it was observed that the leakage current is also sensitive to the humidity variation. The correlation between leakage current and the relative humidity curves are shown in Fig. 1 a, b. This can be explained by the introduction and rearrangement of negative charges in a humid air on the oxide surface which leads to surface depletion and consequent increase in the leakage current, as the surface generation becomes added to the bulk leakage current [2], [3].

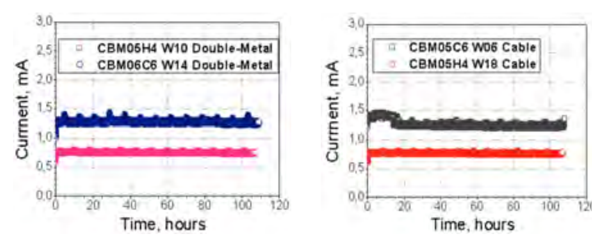

Figure 2: Leakage current stablity: sensors with double-metal (left) and external microcable (right) technologies.

Figure 2 shows the results obtained for all prototype sensors for a 110 hours time period. All the presented data points have been normalized to the values at the reference temperature (-5°C) to exclude the temperature variation impact using the Equiation 1. The humidity variation for the selected time period was considered to be negligible. The measurement results show stable behaviour of the leakage current for the sensors with both double-metal and external microcable interconnection technologies.

This work is supported by HGS-HIRe, H-QM, HIC for FAIR.

References

[1] CBM collaboration, Technical Design report for the CBM Silicon Tracking System, GSI Report 2013-4.

[2] M. Laakso, P. Singh, P.F. Shepard, Nucl. Instr. and Meth. A **327** (1993) 517-522.

[3] F.G. Hartjes, Nucl. Instr. and Meth. A **552** (2005) 168-175.

Development of a compact, highly efficient heat exchanger assembly for bi-phase CO_2 Cooling of the CBM Silicon Tracker

E. Lavrik[1], *A. Lymanets*[1,2], *and H.-R. Schmidt*[1]
[1]University of Tübingen, Tübingen, Germany; [2]Institute for Nuclear Research, NASU, Kiev, Ukraine

The CBM Silicon Tracking System (STS) is a compact detector that consist of double-sided silicon microstrip sensors with an overall volume of about 1 m^3 defined by the aperture of the dipole magnet[1]. In order to reduce the material budget of the detector all heat producing readout electronics were moved outside of the acceptance zone, which in turn greatly reduced the space available for cooling. In order to avoid thermal runaway during the operation of the detector, silicon sensors have to be kept at temperatures below $-5°$C. This is quite challenging as up to 50 kW of heat is dissipated from the STS Front-End-Electronics (FEE) in a rather small volume with very limited space for heat exchanger plates. We use bi-phase CO_2 cooling due to its superior volumetric heat transfer coefficient, which is about an order of magnitude better than conventional freons. The aim of this research project is to optimize the Front-End-Board box (FEB) housing FEE elements in terms of heat transfer efficiency under the given space constraints.

Open CO_2 Cooling system

In order to find the most effective FEB box design (Fig. 1), a series of Finite Element Method (FEM) studies were conducted as well as an open CO_2 cooling system was built, which allowed us to utilize the bi-phase CO_2 cooling.

The cooling system is designed to absorb about 200 W thermal load under realistic geometrical constraints. One has to verify the cooling efficiency of various FEB box designs. The heat generated by resistive thermal load will be dissipated in FEB box and removed by a cooling plate with integrated capillaries with total length of about 2 m and about 2 mm diameter[2].

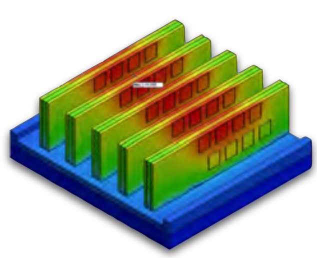

Figure 1: Sample FEB box design with heat distribution information obtained from thermal FEM studies.

Results

To find out the most effective FEB box design, different FEB box were produced with varying thickness of the FEE supporting structure (shelve). These designs were then tested under different heat loads. Table 1 shows the experimental results from selected measurements. The experimentally measures trends were reproduced by the simulations.

Power Applied, W	**Maximum Temperature, °C**		
	1 mm	2 mm	3 mm
140	15	-14.2	-22.6
200	24	0.2	-15

Table 1: Experimentally measured maximal temperature on the FEB box in dependence of power applied and shelve thickness

The optimal FEB box design was found to be with shelve thickness of 3mm. Resulting FEB box dimensions are $105 \times 85 \times 35{,}6$ mm^3. This design was proposed to be used in the production of STS detector.

To make the operation of the STS detector cooling safer one wants to move further away from the triple point of liquid CO_2 ($-56.6°$C, 5.11 bar), i.e. eliminate the risk of solidifying the coolant. This is achieved by increasing the CO_2 temperature and pressure in the cooling lines, although this decreases cooling power. Table 2 shows the results of FEM simulations conducted to examine the dependence of maximal FEB box temperature versus coolant temperature.

Maximum temperature, °C		
T, coolant	T@200 W	T@140 W
-40	-10.6	-12.7
-30	-4.9	-9.9
-20	0.8	-4.1
-10	6.5	1.58

Table 2: Result of simulations showing the expected maximal temperature on the FEB box in dependence of initial coolant temperature and power applied

This study show that safe operation and sufficient cooling can be achieved at $-30°$C.

References

[1] J. M. Heuser et al., Nucl. Instr. Meth A **568**, 258 (2006)

[2] E. Lavrik, A. Lymanets, H.-R. Schmidt, CBM Progress report 2013, p. 40

Optical quality assurance procedures for STS silicon sensors

E. Lavrik[1], *A. Lymanets*[1,2], *and H.-R. Schmidt*[1]
[1]Universität Tübingen, Tübingen, Germany; [2]Institute for Nuclear Research, NASU, Kiev, Ukraine

The CBM Silicon Tracking System (STS) is a compact array of silicon microstrip sensors [1]. The total number of sensors is about 1300 and they will be delivered from different manufacturers and in different form factors[2]. Thus the operation of the detector requires all sensors to be optically quality assured in order to meet the requirements with respect to surface conditions (scratches, durst grains, photo-resist residues, etc) and geometry (wafer thickness and warp, edge parallelity etc.)

For this purpose a clean area was established in a laboratory at the University of Tübingen and an optical inspection setup was built[3]. The setup consists of a XY-inspection object table based on closed-loop Movtec SMC-300 linear servomotors with a 5 MP Moticam microscope camera combined with 12X magnification lens from Navitar company. The setup allows to scan in X-Y-Z range of 200/75/75 mm with a micrometer precision and taking pictures with a resolution of 2592 × 1944 pixels.

Optical inspection workflow

A typical inspection workflow consists of several steps - preparation for inspection, inspection procedures, inspection report. (Fig. 1)

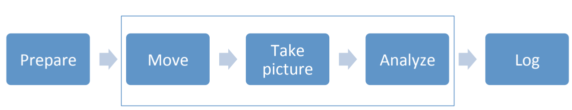

Figure 1: Typical workflow of inspection procedure

First, a sensor is laid on the inspection chuck, camera parameters are adjusted followed by self-calibration cycle of the system. In a main part of the program the sensor is moved below the camera to scan the regions of interest, pictures are taken and analyzed to detect various defects and features on the sensors' surface. Lastly, a report that summarize the inspection results is produced. In this report all the technical data about sensor defects and features with corresponding images containing these defects and features. The report is then stored to disk and uploaded to the STS sensor database.

Method implementation

First, the motors and camera parameters are adjusted if needed (gamma, brightness, color gain, other parameters). Geometrical self-calibration begins with a spiraling pattern search for the nearest alignment mark which is an 120×120 µm^2 object. The alignment mark is detected by pattern matching algorithms (Fig. 2). Information extracted at this step gives rough estimate on the sensor misalignment with respect to the XY motor axes. This in turn allows to optimize amount of steps needed to detect all 8 alignment marks of a sensor.

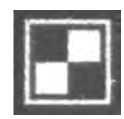

Figure 2: Sample alignment mark image to use in pattern matching algorithms

After detecting all of 8 alignment marks and determining their respective coordinates in step motor space, one can solve the minimization problem (1).

$$\vec{x}_m = \mathbf{S}\,\mathbf{R}\,\vec{x}_s \qquad (1)$$

Having a stretching matrix S and rotation matrix R from problem solution, coordinates from sensor coordinate space (s) could be translated to motor coordinate space (m), thus enabling us to precisely scan along sensor axes. Specific scans are performed for various geometries (normal, "baby", daisy-chained sensor) and different manufacturers (CiS, Hamamatsu) of a sensor.

After each step of a moving sequence the picture in the camera's field of view is taken. This image is then analyzed with the NI Vision® package to detect various defects and features on the sensors' surface, such as photo-resist residues, scratches, dust grains. OCR algorithms from the Vision package enable us to read text parts written on the sensor to extract information about sensor's part number and include it later in the report.

When scan is finished, the quality of the sensor is classified based on a given set of criteria. Lastly a human readable report containing the information on the sensor is produced. The report contains pictures of possible defects and their coordinates in sensor coordinate space.

References

[1] J. M. Heuser et al., Nucl. Instr. Meth A 568 (2006) 258

[2] The CBM Collaboration, "Technical Design Report for the CBM. Silicon Tracking System (STS)", December 2012, p. 23.

[3] E. Lavrik et al., CBM Progress report 2013, p.28

The GBT Based Readout Concept for the CBM Silicon Tracking System

J. Lehnert[1], *W. Müller*[2], *and C.J. Schmidt*[1]
[1]GSI, Darmstadt, Germany; [2]FAIR, Darmstadt, Germany

The sensors of the CBM Silicon Tracking System (STS) are read out by frontend boards (FEB) with 8 STS-XYTER ASICs for 128 channels each implementing the analog frontend, analog-to-digital conversion and the readout of buffered hits via multiple serial links. A subsequent stage with data aggregation from several ASIC links and an electrical-to-optical interface is required before transfering the data to the FPGA based data processing boards (DPBs) located in some distance at the detector site where preprocessing and further data transfer occur. The aggregation stage is located in the cooled STS detector box inside the CBM magnet, which implies that the hardware must fulfill conditions in terms of radiation hardness, magnetic field, space contraints and thermal environment.

GBT Devices

A concept was devised for the STS readout to implement the aggregation and optical readout functionality on a separate readout board (ROB) using the GBTX, SCA and Versatile link devices [1] developed at CERN. The devices of the GBT project are mainly designed as interface between on-detector and off-detector electronics for future LHC experiment upgrades in a radiation environment up to tens of Mrad. The GBTX ASIC implements up to 56 SLVS links (E-Links) as electrical frontend interface with link speeds of 80, 160 or 320 Mb/s and a total bidirectional user bandwidth up to 4.48 Gb/s on the high speed serial link. Latencies of data throughput in the GBTX are fully deterministic. The Versatile Link devices are radiation hard optical transceivers and (twin) transmitters in SFP formfactor modules.

The STS Readout Chain

The ROBs for the STS will contain 1 GBTX device as master connected to an optical transceiver (VTRx), 2 GBTX devices connected to an optical twin transmitter (VTTx) and a GBT-SCA (Slow Control Adapter) device for I2C based control of the 2 GBTX without optical downlink (see Fig.1). The GBTX uplinks will be operated in the widebus mode (without forward error correction) and therefore provide 3x14 frontend links at 320 Mb/s each. 40 of these links are used to connect to the FEBs. 3 types of FEBs will be used with either 1, 2 or 5 readout E-Links per ASIC depending on the local data load, resulting in a maximum of 5, 2.5 or 1 FEBs of the different types connected to a single ROB. With additional spatial contraints from system integration (no connections across quarter stations, no cable crossings) the total number of ROBs for the STS amounts to approx. 1000, with 3000 optical readout links and 1000 control links. For ASIC timing and control, one single E-Link output and one phase adjustable 160 MHz clock are connected from the master GBTX to each FEB; the control responses use any of the readout uplinks. All E-Links between FEBs and ROBs will be AC-coupled in order to allow the connection of a single ROB to multiple FEBs operated at different potentials together with their connected sensors. The ROBs will be located at the sides of the STS detector box outside the detector acceptance. Flexible flat cables of approximately 0.6 m length will connect the stacks of FEBs for a given quarter station of the detector to the corresponding stack of ROBs.

The version 2 of the STS-XYTER ASIC[2] will implement the GBTX E-Link interface with a configurable number of 1 to 5 readout links and a synchronous readout and control protocol that was specifically developed for the STS-XYTER readout via GBTX [3]. A demonstrator board with a single GBTX and Versatile Link components will be available from CERN for initial tests in early 2015 and a CBM ROB prototype with full functionality is currently being prepared. Larger quantities of the devices from the sole production run are expected end of 2015.

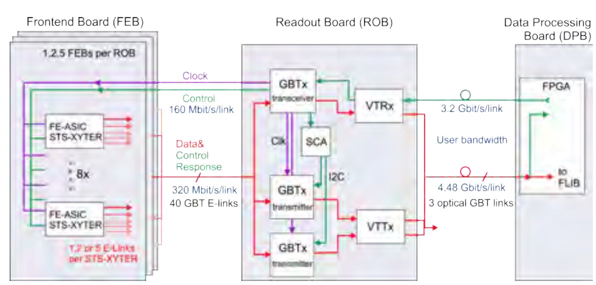

Figure 1: The STS readout chain with the readout board based on GBTX and Versatile Link components.

References

[1] P. Moreira et al., CERN Document Server CERN-2009-006.342

[2] R. Szczygiel et al., CBM Progress Report 2014, Darmstadt 2015

[3] K. Kasinski et al., Proc. SPIE 9290 (2014) 929028

Monitorig system for radiation hardness tests of electronic components for future FAIR experiments.

S. Löchner[1] *and P. Koczoń*[1]
[1]GSI, Darmstadt, Germany

Electronic components installed in the field of reaction products in future experiments at FAIR have to be radiation hard. At present, selected parts undergo exhaustive tests with use of intense minimum ionising particles' beams, mostly 3 GeV protons at Jülich sychrotron facility. A control system based on ARDUINO processor has been developed to monitor the components status in situ .

Monitoring system requirements

For components like DC/DC converters or LDO voltage stabilisers the output voltage level as well as expected transient voltage spikes rate has to be monitored during irradiation. Voltage level monitoring (input and output) requires relatively low readout frequency below 1 Hz and can be implemented on inexpensive ARDUINO-Nano system. It is programmed to control an optocoupler based set of relays to govern applied input voltages (for each of 12 channels separately) and reading an ADC values of output voltages for each channel. System supervises the output voltage level and - if needed - switches off the malfunctioning channels to avoid its influence on other DUTs. Measurement status is logged on a local memory and displayed via implemented web server on connected clients. The control electronics has to be placed far away from the device under test in order to avoid spurious effects due to the irradiation.

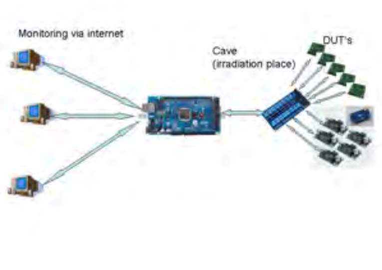

Figure 1: Block diagram of the system testing a set of DC/DC converters controlled by ARDUINO processor.

Hardware realisation

A base plate equipped with two sets of clamps and a PCB-holder has been prepared to accomodate different devices under test (DUTs). They have to be placed in a row such that the irradiating beam punches through all of them. A small scintillator placed on the beam axis behind tested chips and read out by a photomultiplier monitors the beam intensity. Its signals are also registered by ARDUINO system on separate counter and stored with time stamps spill

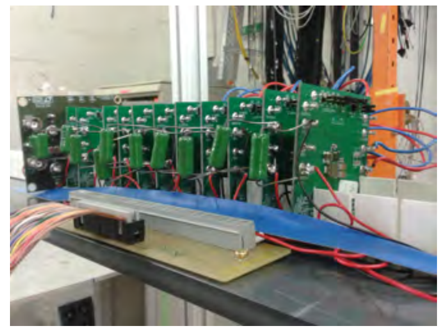

Figure 2: Base plate with PCB card holder and wiring.

by spill. This information helps to estimate precisely beam intensity integral. One raw of electrical clamps is supplied with input voltage (controlled by ARDUINO via set of relays) for the DUTs. Their outputs are wired via second clamps raw to the multiplexer and ADC on controller board to supervise output voltage levels.

ARDUINO control system

The processor itself can be programmed in a C-like programing language with use of different libraries to serve standard functionality (time server, SD-card I/O, internet I/O). Main loop of the program consists of output voltage

Figure 3: Control output of the monitoring system.

check channel by channel, input voltage check, counter readout, internet service, timer service. The voltage read out values are compared to the upper and lower threshold values which can be defined for each channel. In case of over- or under voltage in three consecutive readout steps the affected channel is switched off.

References

[1] http://http://www.arduino.cc/

Radiation hardness tests on electronic components for CBM/STS low voltage power supply.

S. Löchner[1], *P. Koczoń*[1], *and A.Rost*[1]

[1]GSI, Darmstadt, Germany

Electronic components installed in the field of reaction products in future experiments at FAIR have to be radiation hard. At present, selected parts like DC/DC converters and LDO voltage stabilisers undergo exhaustive tests with use of intense minimum ionising particles' beams, mostly 3 GeV protons at Jülich sychrotron facility.

Testing setup

For components like DC/DC converters or LDO voltage stabilisers the output voltage level as well as expected transient voltage spikes rate due to the Single Event Upsets has to be monitored during irradiation. Voltage level monitoring (input and output) requires relatively low readout frequency below 1 Hz and can be implemented on inexpensive ARDUINO-Nano system [1]. Fast transients have been investigated on 4 trace digital oscilloscope Rhode-Schwarz RTO1044 [2] (triggering threshold has been setup to 15 mV). Measurement results have been recorded in nonvolatile memory and analysed.

Selected ASICs

For the radiation hardness tests several DC/DC converters have been chosen. Selection criteria like circuit efficiency, chip size, low coil inductivity, apropriate output voltage and sufficient output power as well as voltage setting flexibility have been applied. Only one model

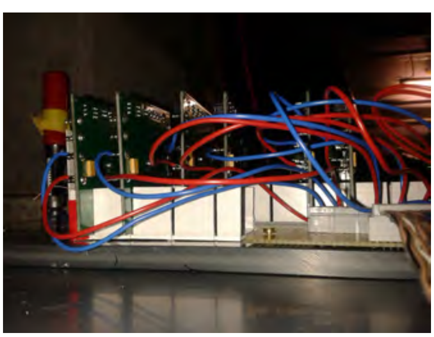

Figure 1: Base plate with PCB card holder and wiring.

of the LDO stabilizer produced in rad hard technology has been examined until now. Alltogether 10 test boards with LTC3605 and 3 Boards with LTC3610 (Linear Technology) and 4 boards containing LM2596S (Texas Instruments) have been tested in two beam times. A GaN based ISL75051SRH has been abandoned according to producer information on radiation hardness of only 100 krad. All tested ASICs have been powered on during irradiation runs.

Test results

PCBs with tested chips have been placed in a row along the beam axis such that the irradiating beam punched through all of them. A small ionisation chamber placed on the beam axis behind tested chips has been used to monitor the beam intensity. corresponding to the shape of the

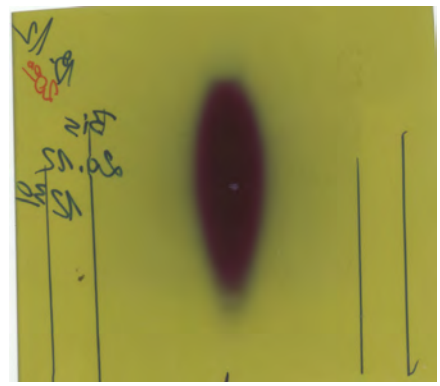

Figure 2: Beam spot on Gafchromic self-developing dosimetric film.

proton beam with optical density corresponding to the integrated beam intensity. The total dose is known from the measurement with the ionisation chamber and position of irradiated chips is marked on the film. By optical scanning a fractional dose can be estimated for each point on the film. This allows to estimate precisely beam intensity integral and - consequenty - the dose at ASIC chips.

Neither of tested DC/DC converters survived more than $4.3*10^9$ protons.

No fast transients have been observed on LDO voltage stabilisers which have absorbed only 10^8 protons (measurement was stopped for technical reasons before planned dose was reached).

References

[1] S. Löchner and P. Koczoń GSI Annual Report 2014

[2] http://www.rohde-schwarz.de/de/Produkte/messtechnik-testsysteme/aerospace-and-defense/messtechnik/oszilloskope-fuer-ad/RTO.html

[3] http://www.ashland.com/products/gafchromic-radiotherapy-films

A custom made wafer probe for strip detector quality assurance of the CBM

A. Lymanets[1,2]*, I. Panasenko*[1,2]*, and H. R. Schmidt*[1]

[1]Physikalisches Institut, Universität Tübingen; [2]Institute for Nuclear Research, Kiev, Ukraine

The STS will be constructed of about 1300 double-sided silicon microstrip detectors with total area of $\sim 4\ m^2$. It has about 2.1 million readout channels. The microstrip sensors with 58 μm pitch have double metalization connecting the short corner strips resulting from the stereo angle of 7.5°. Due to its complex structure, all sensors have to be tested before assembling into detector modules. Large volume tests of the sensors require a suitable probe station and automatisation. Due to the large size of $62{\times}62\ mm^2$, the CBM microstrip sensors are not well suited for the characterization at conventional probe stations. Therefore, a custom probe station is beeing developed at Tübingen University (see Fig. 1). It consists of optical, mechanical and vacuum systems placed in a shielding box. Components of our probe station are (see schematic view on Fig. 2):

- SourceMeter Keithley 2410
- Picoammeter Keithley 6487
- LCR-Meter QuadTech 7600
- Switching matrix Keithley 708B
- Aerotech linear and rotary motors with NPAQ-MR controller
- Vacuum pump (200 mbar abs.) and shielding box
- NAVITAR optical system with TheImagineSource camera (5 MP resolution)

One of the main requirements is a repeatability better than 1 μm to allow an automatic succesive positioning on all 1024 pads of a sensor. It will be fulfilled with Aerotech linear motors with precision $\sim 0.4\ \mu m$. The sensors will be fixed on a custom made vacuum chuck mounted on the motors.

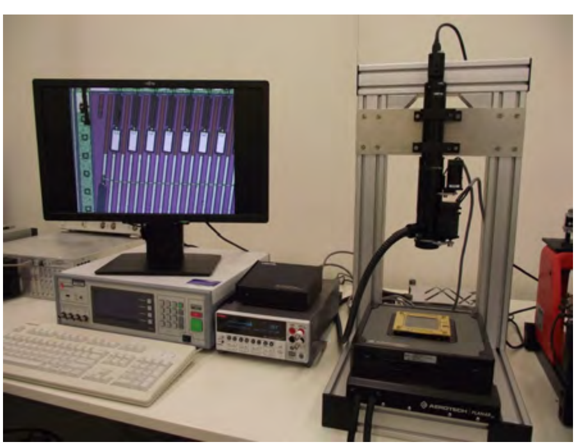

Figure 1: Quality assurance infrastructure in the clean room.

The probe station allows to investigate the electrical characteristics of the sensors (full depletion votage) as well as characteristics of individual strips (leakage current, interstrip capacitance, etc). The switching matrix allows to use all connected needles in any combination by any of the measuring devices. It leads to strongly reduced measurement time due to fast reconfiguration of the setup.

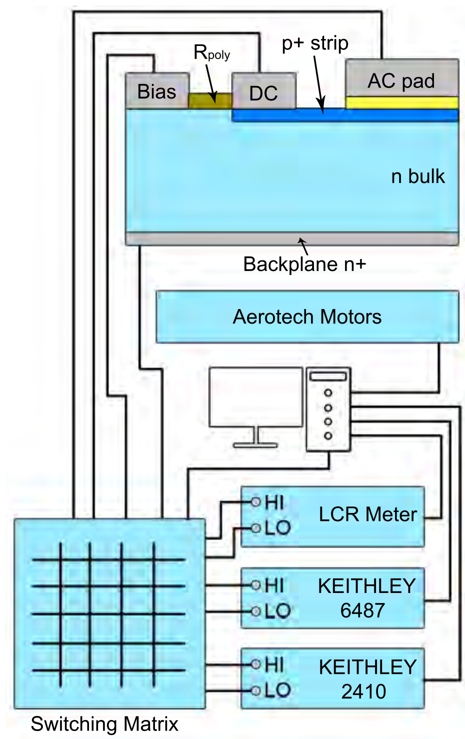

Figure 2: Schematic view of the custom made probe station.

It is foresees that all system components will be controlled via LabVIEW. A dedicated software development to automate repetitive measurement steps is in progress.

References

[1] J. Heuser *et al.*, *Technical Design Report for the CBM Silicon Tracking System*, GSI Report 2013-14, http://repository.gsi.de/record/54798

[2] J. Heuser *et al.*, CBM Progress Report 2012, p. 8

Charge sharing in micro-strip sensors: experiment and simulation

H. Malygina[1,2], *V. Friese*[3], *J. M. Heuser*[3], *A. Senger*[3], *and I. Sorokin*[2,3]
[1]Frankfurt University, Germany; [2]KINR, Ukraine; [3]GSI, Darmstadt, Germany

In December 2013 [1] and December 2014 [2] a prototype setup of the Silicon Tracking Systerm (STS) for the CBM Experiment was tested in a 2.4 GeV/c proton beam at the COSY synchrotron (Juelich, Germany). In the middle station, which could be rotated around its vertical axis, CBM05 prototype sensors (n-side with 0^0 stereo-angle, p-side with 7.5^0) were under a test aiming at studying charge sharing. Readout NXYTER chips were triggered by a hodoscope. The equivalent noise charge of about 8 ADC promoted adapting the threshold of 20 ADC in the cluster finder to cutoff the noise.

Charge sharing between two fired strips is described by $\eta = S_R/(S_R + S_L)$ with $S_{R(L)}$ being the signals on the right (left) strip of the cluster [3]. The left panel in fig. 1 shows the measured distribution of η. Position and width of the peaks depend on characteristics of the sensor and the readout electronics (e.g. strip pitch, signal-to-noise ratio, coupling capacitance, threshold, etc.). For inclined tracks the η-distribution is essentially asymmetric. The position of the cluster with respect to the left strip can be calculated as $x_\eta = p\left(\int_0^\eta \frac{dN}{d\eta'} d\eta'\right)\left(\int_0^1 \frac{dN}{d\eta'} d\eta'\right)^{-1} = pf(\eta)$, where p is the strip pitch and $f(\eta)$ obtains from measurements (see the right panel of Fig. 1).

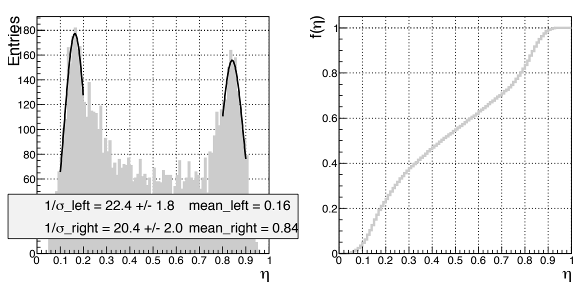

Figure 1: *Left:* η measured for p-side of CBM05 with Gaussians fitting the peaks. *Right:* $f(\eta)$. Perpendicular tracks.

Cluster size distribution at different angles is a good tool to verify the simulations of charge sharing in a silicon strip detector (implemented in the advanced model of the digitizer in cbmroot). Figure 2 presents a typical distribution at one angle. Assuming the NXYTER calibration [4] to be accurate, we get the reconstructed charge (Fig. 3) lower than the one modelled. This indicates additional charge losses. Imposing 20% charge losses in the sensor (on top of the 5% losses due to the trigger signal delay) yields a better agreement. These losses have currently no explanation.

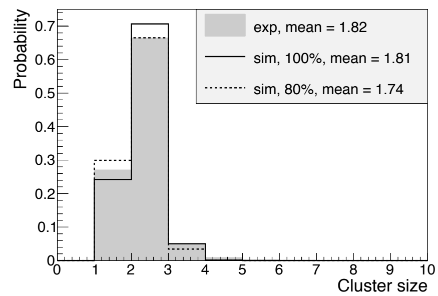

Figure 2: Cluster size distribution for slightly inclined tracks (10^0). Experimental data for n-side (the gray filled histogram), simulations with no (the solid line) and 20% (dashed) additional charge loosing.

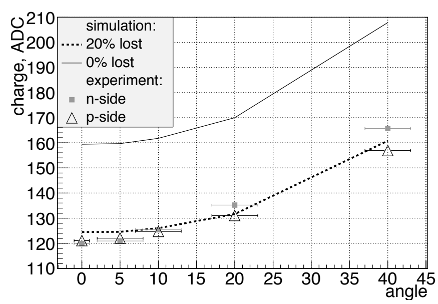

Figure 3: Most probable registered charge in dependence of track angles. The points show the experimental data from beamtime 2013 (the open triangles – p-side, the filled squares – n-side, the uncertainties in the angle measurements are drawn with bars) and the modelled data are represented by the lines (the solid line – no charge losses in the sensor, the dashed – 20% losses).

References

[1] T. Balog et al., “In-beam test of prototype modules for the CBM Silicon Tracking System”, CBM Progress Report 2013 (2014) p. 32

[2] J. M. Heuser et al., **“TITLE OF THIS YEAR REPORT ABOUT BEAMTIME”**, this report

[3] R. Turchetta, Nucl. Instrum. Methods A335, 44-58 (1993)

[4] I. Sorokin et al., “Transconductance calibration of n-XYTER 1.0”, CBM Progress Report 2012 (2013) p. 14

Setting up the STS module and ladder assembly site at JINR-LHEP

Yu.A. Murin[1], V.V. Elsha[1], V.A. Penkin[1], O.D. Sheremetyev[1], V.M. Borshchov[2], M.V. Gerasimenko[2], M.A. Protsenko[2], and I.T. Tymchuk[2]

[1]LED Technologies of Ukraine (LTU) Ltd, Kharkov, Ukraine; [2]JINR, Dubna, Russia

Works on the organization of module and ladder assembly site at LHEP JINR for CBM STS were performed.This assembly site is developed jointly by the specialists from JINR and LTU. The work was supervised and coordinated by JINR.

The assembly site includes: dressing room, changing room and clean room (see Fig. 1). The range of clean room purity should correspond to the ISO 7 class. The total area of the site exceeds 100 square meters, including more than 50 square meters of clean room.

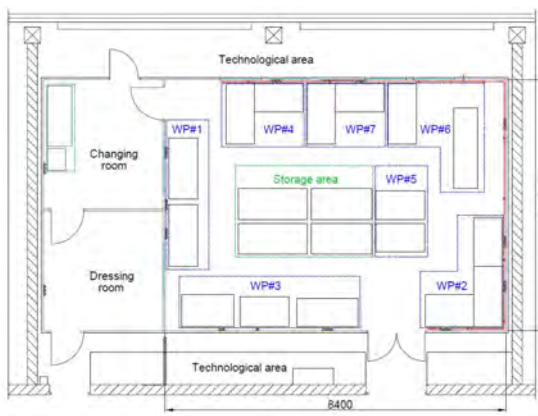

Figure 1: Layout of the assembly site.

In the cleanroom seven workplaces will be created with the following indicated equipment [1-2]:

1. Workplace for parts kitting.
2. Workplace for modules and components assembling (automatic bonder for TAB-bonding).
3. Workplace for bond joints protecting and gluing (dry box, scales, dispenser, oven).
4. Workplace for chip-to-FEB wire bonding (semi-automatic bonder for wire-bonding).
5. Workplace for modules and components testing.
6. Workplace for ladders assembling (optical-mechanical system).
7. Workplace for ladders testing.

All work places must be equipped by microscopes and ionizers. Also the area for modules and components storage must be prepared.

In the beginning of 2014 space for the construction of the cleanroom was prepared in the building of JINR-LHEP. In the beginning of 2015 the creation of the cleanroom was finished and its certification completed (Fig. 2).

Figure 2: Cleanroom prepared at JINR-LHEP.

Further works on the establishment of an assembly site will comprise: installation of equipment on workplaces, connecting line of the vacuum and compressed air, start-up of the site, training of technical staff of the basic assembly operations. After completion of the abovementioned works, this site will be able to provide assembly productivity (within production stage) in the range of 15 to 16 modules per month and 3 ladders per month [3]. At full load, the staff working in the cleanroom will amount to at least seven technicians.

References

[1] Workshop on module and ladder assembly for the CBM Silicon Tracking System, JINR, Dubna, Russia, 6-7 June 2013.

[2] Workshop on module and ladder components production and assembly for the CBM Silicon Tracking System, LTU Ltd, Kharkov, Ukraine, 14-17 January 2014.

[3] V.M. Borshchov at al. CBM Progress Report 2013, Darmstadt 2014, p.44.

Charge collection in STS silicon microstrip sensors at their surface layer

I. Panasenko[1], *V. Dobishuk*[1], *J. Heuser*[2], *V. Kyva*[1], *V. Militsiya*[1], *Ie. Momot*[1,3], *V. Pugatch*[1], *and M. Teklishyn*[1]

[1]KINR, Kiev, Ukraine; [2]GSI, Darmstadt, Germany; [3]Goethe University, Frankfurt, Germany

To provide radiation tolerant devices for the CBM experiment (Silicon Tracker Station) prototypes of silicon microstrip sensors have been produced in two technologies. For the short-long stereo-strips connection, either double-metallization lines ("double metal" sensor) or a single-metallization design with an external microcable ("single metal" sensor) have been manufactured. We report here the results of studies performed for those sensors with the Pu (triplet) alpha-source and laser (640 nm wavelength). Both methods provide test of the charge collection at the sensor surface layer where double metallization is laid out. Measurements were carried out exploring discrete electronics and the fast-slow coincidences setup at KINR. This allows studying a charge sharing between adjacent strips of the silicon sensor hit by alphas or laser pulses. The degradation of the cluster finding efficiency in the vicinity to the double-metal connecting lines in heavily irradiated microstrip silicon sensors has been observed [1].

The CBM05H4 'double metal' and 'single metal' (HAMAMATSU) sensors were full depleted at 80 V. In a two-dimensional (E_i x E_{i+1}) energy distribution of events in adjacent strips 'i' and '(i+1)' three loci for a ^{239}Pu, ^{238}Pu and ^{233}U alpha-particles source are shifted by ~ 20 % to lower energies for the double metallization sensor in comparison with the single metal one. Also the widths of loci are larger. The evaluation shows that this could be explained by the alpha-particles energy loss and straggling in the SiO_2 isolation layer present only in the sensor with a second metallization layer. Biasing voltage scan has demonstrated expected performance for these sensor types, while CBM06C6 (CiS production) have shown appearance of the dead layer ($\sim$ 25 μm) in the interstrip gap at full depletion voltage.

Also measurements with a 640 nm laser beam (7 μm spot) scanned over the sensor area were performed for sensors irradiated at the KINR isochronous cyclotron up to the $2{*}10^{14}$ 1 MeV n_{eq}/cm^2. Figure 1 shows two dimensional distribution of amplitude of charges originated in the interstrip gap of the CBM05 non-irradiated sensor illuminated by the scanning laser beam. It demonstrates excellent position resolution achieved: beam spot position is indicated by figures of 15 μm, 18 μm, 21 μm etc. Figure 2 illustrates degradation of the charge collection by 30% in the irradiated sensor (the locus of laser events is shifted to lower amplitudes region). Analysis of data for other sensors is in progress. Tests with the ^{90}Sr β-source will be made soon exploring the 'ALIBAVA' microelectronics readout system.

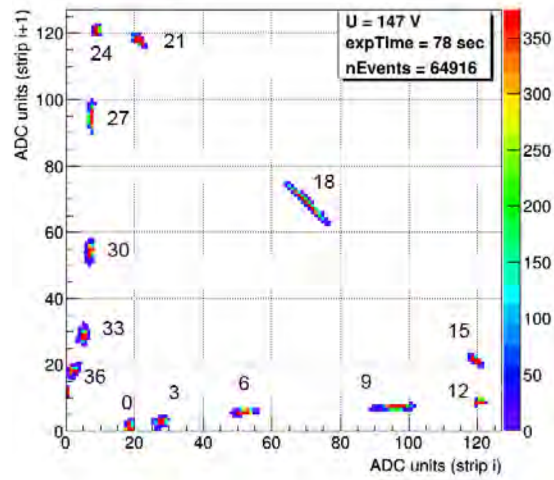

Figure 1: CBM05 – non-irradiated sensor: Laser scan in the interstrip gap.

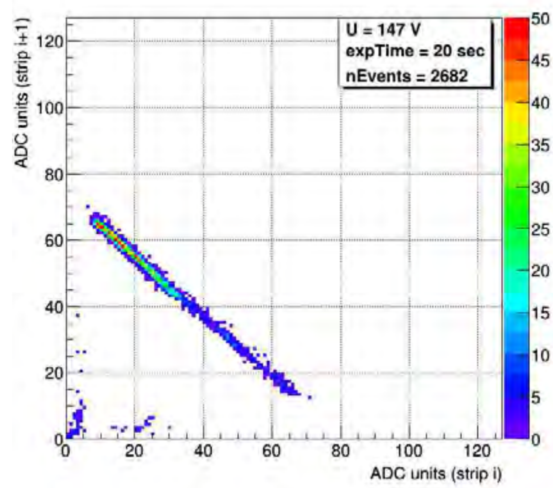

Figure 2: CBM05 – irradiated sensor: Laser scan in the interstrip gap.

References

[1] A. Affolder et al., Radiation damage in the LHCb vertex locator, JINST 8 (2013) P08002, arXiv:1302.5259.

Studies of Correlated Signals in CBM STS Silicon Microstrip Sensors

V. Pugatch[1], *J. Heuser*[3], *P. Larionov*[1], *M. Pugach*[1,2], *I. Sorokin*[1,3], *and C. Sturm*[3]
[1]KINR, Kiev, Ukraine; [2]Goethe University, Frankfurt, Germany; [3]GSI, Darmstadt, Germany

Physically correlated signals in adjacent strips of a microstrip detector appear due to charge sharing. A significant fraction of tracks is reconstructed from two- and three-strip cluster events where analogue read-out improves the position resolution. Non-physically correlated signals originated by cross-talk, pick-up or common mode fluctuations may also occur in read-out channels. Measurements of charge sharing between adjacent strips of the CBM05 and CBM06 prototype silicon sensors designed for the CBM Silicon Tracking System were performed at KINR [1]. In a two-dimensional (E_i x E_{i+1}) energy distribution of physically correlated events loci from an alpha-particle source were clearly observed in adjacent strips i and (i+1) (Fig. 1).

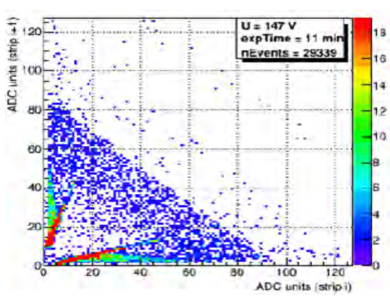

Figure 1: Two-dimensional (E_i x E_{i+1}) energy distribution in adjacent strips i and (i+1) obtained with alpha-particles.

Detailed studies revealed also non-physical correlated events populating loci from the very low amplitudes along the straight and reaching the positions of the alpha particle contribution. Among possible explanations we considered a cross-talk with the channels (i-1) and (i+2) located in close vicinity to the ones under the test. Correlated event studies were carried out recently with n-XYTER readout electronics at GSI. Examples of data obtained are shown in Fig. 2.

In Fig. 2 (upper) physically correlated events at the p-side triggered by MIP β-particles from ^{90}Sr are observed along the expected line (most probable value) with a sum of amplitudes around 140 ADC counts. The simulated noise distribution is shown in the middle part of Fig. 2. The events populating the loci alongside the straight lines originating from the (0.0 $\times$ 0.0) coordinate are apparently correlated non-physical events (see lower Fig. 2). These signals simultaneously appearing at adjacent strips i and (i+1) are initiated either by the digital part of the n-XYTER chip and/or by external powerful electromagnetic sources. It is worthwhile to notice that such events were also observed at

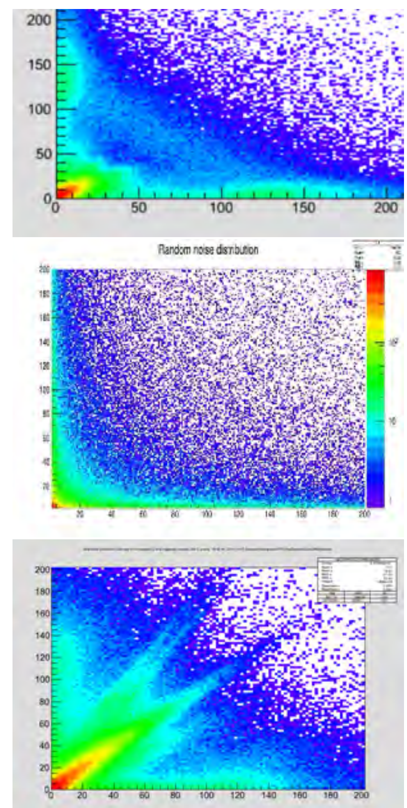

Figure 2: Two-dimensional (E_i x E_{i+1}) amplitude distribution of events in adjacent strips 'i' and '(i+1)' of the CBM05 sensor. Data taken with ^{90}Sr source (upper: p-side; lower: n-side). A simulated noise distribution is shown in the middle panel.

n-XYTER channels not connected to the microstrip detector at all though with a low, yet significant amplitude of up to 40 ADC counts. The results of these studies have to be taken into account in the test measurements with a newly designed STS-XYTER microchip as well as in building the infrastructure for power lines, shielding and grounding of the STS detector. Further studies with the ALIBAVA read-out system [2] are planned to clarify the origin of the non-physical correlated events.

References

[1] I. Panasenko *et. al.*, CBM Progress Report 2014

[2] https://www.alibavasystems.com

Low and high voltage powering concept for the CBM Silicon Tracking System.

C.J.Schmidt[1] *and P. Koczoń*[1]
[1]GSI, Darmstadt, Germany

Due to the radiation damage of the silicon sensors of CBM-STS detector their performance will deteriorate in course of experimental activity. Gradual increasing of their depletion voltage will improve the efficiency again and prolongate their life time. This procedure will be applied for each one of almost 1800 sensors separtely what forces powering architecture described in this report.

Requirements for low voltage powering of one silicon sensor.

Silicon Tracking Systen of CBM will be operated together with Micro Vertex Detector inside the magnetic field of 1 Tesla and rather small volume of about 1 m^3 [1]. To minimize the scattering of the reaction products tracked by the system only silicon sensors, their supporting structure and signal cables will be installed inside of the detector acceptance. The readout and converting electronics and its cooling as well as power converter will be installed on the detector circumference. Altogether almost 40kW of heat has to be removed from STS box to reach working conditions of -5 ^{o}C for silicon sensors. Moreover, a very restricted amount of surface is available for connectivity with the outside infrastructure: all the cooling system tubing, low and high voltage cabeling, data transmission and control links sockets have to be connected on 1.5 m^2 surface of the upstream wall of the detector. At least two different voltages are necessary for the STSxyter readout ASIC [3, 4] and additional two for the GBTx [5] and optical converter.

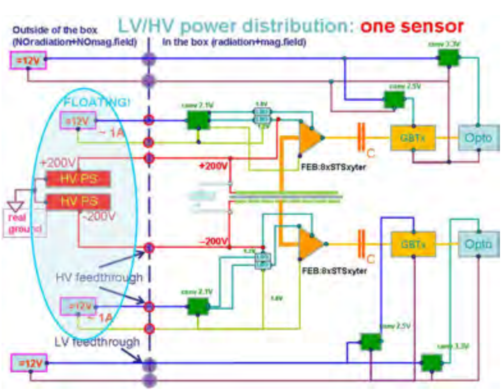

Figure 1: Low and high voltage powering of one silicon sensor..

Each sensor will be operated in a floating manner, e.g. p- and n-side will sense one half of the depletion potential (positive and negative) and the readout ASICs (and its powering) has to be applied "on top" of the sensors' depletion voltage. The distance between the last component shaping low voltage should be as close as possible to the front end ASIC in order to minimize amount of the noise irradiated into the system. High depletion voltage (low current) can be generated and controlled from the outside of the STS volume. All used electronic parts inside the STS box should be radiation hard and should stand a magnetic field strength of at least 1T.

Proposed powering for CBM-STS detector

Schematics in Fig.1 shows proposed power distribution system. Both sides of the sensor (central part in Fig.1) are supplied with positive and negative depletion voltage generated outside of the magnetic field (+200V and -200V in this case, red lines in Fig.1) with a common grounding. Sensor's strips are connected to the STS-xyter readout ASIC on the Front Electronic Board FEB with microcables (orange elements in Fig.1). ASICs powering of 2.2V and ca 4A (per FEB) will be generated by FEAST DC/DC converter placed on the side part of the cooling plate [2]. It supplies two LDOs converting the input voltage to 1.8V (digital) and 1.2V (analog part) of ASIC. The latter has to be grounded in the sensor vicinity to +200V or -200V respectively. Input power of 12V and about 1A is delivered from outside for each sensor separately. This construction minimizes grounding loops and assures separation of strong and weak current flow. A GBTx chip is equipped with many e-links and can communicate with more than one FEB simultaneously so GBTx circuitry has to be galvanically isolated from STSxyter chips. GBTx and optical interface require their own power which will be generated from dedicated 12V lines and additional FEAST converters (uppermost and lowermost parts in Fig.1 in green). STSxyter as well as GBTx power stabilisation will be realised by LDO components placed directly on corresponding PCB boards. Vertical dashed line in Fig.1 depicts the boarder of the high irradiation and magnetic field region (front wall of the STS detector box) and little circles – electrical connectors to the high (in red) and low (in blue) voltage DC generators.

References

[1] CBM STS Technical Design Report, 2012

[2] http://project-dcdc.web.cern.ch/project-dcdc/

[3] http://repository.gsi.de/record/51956/files/PHN-NQM-EXP-22.pdf,

[4] Time and energy measuring front-end electronics for long sil-

icon strip detectors readout, Nuclear Science Symposium and Medical Imaging Conference (NSS/MIC), 2013 IEEE

[5] GBTx Project: https://indico.cern.ch/event/113796/session/7/contribution/37/material/slides/0.pdf

Fixtures for quality assurance of STS silicon sensors and STS-XYTER ASIC

C. Simons[1], *C. J. Schmidt*[1], *V. Kleipa*[1], *and K.Kasinski*[2]
[1]GSI, Darmstadt, Germany; [2]AGH University of science and technology, Krakow, Poland

To assure the functionality of the silicon microstrip sensors and the quality of bond contacts of the microcables on the STS-XYTER-chip, fixtures are needed, that preferably allow on one hand for non-destructive handling and measurements as well as easy and fast procedures on the other. Several companies were asked for proposals and aps Solutions GmbH had the most promising one: test sockets with Pogo Pins for contacting. *Pogo Pin* is a registered trademark of a US company (*WinWay Technologies*); they are also called spring loaded contacts. Formed like a cylinder, it contains two peaked, spring-loaded pins that make secure contacts with two electronic circuits. For the Pogo Pins different combinations on tip shapes, structures, materials and plating are available so that the particular application may be optimized.

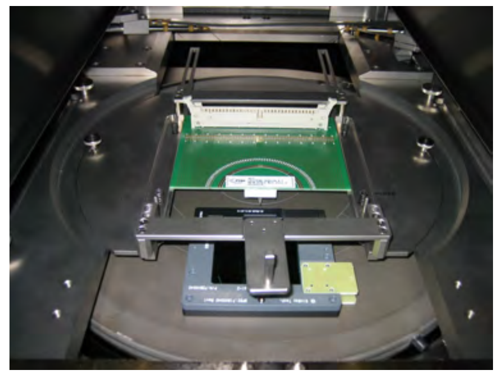

Figure 2: Test socket and probe card on wafer prober.

Test socket for the silicon sensors

The challenge for the different quality measurements of the double-sided sensors is the need for simultaneous biasing contacts from bottom and top side. This problem can be solved with a fixture that consists of a bottom and a top socket. Both sockets include a Pogo Pin to which the bias voltage is applied via a small pcb. The bias pads on the sensor have a comfortable size of 400 μm $\times$ 150 μm to facilitate contacting. With the help of a wafer prober equipped with a movable chuck, the strips may then be stepped through for investigation by means of a probe card. The schematical layout of the fixture and its installation on a wafer prober are shown in Figs. 1 and 2.

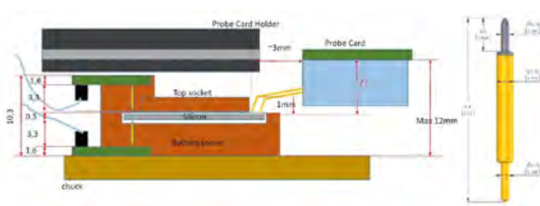

Figure 1: Draft design of the sensor test socket.

Test socket for the STS-XYTER-chip

Each traceline of the microcables that connect the silicon microstrip sensor to the STS-XYTER-readout-chips has to be TAB-bonded onto the pads of the sensors on one side and on the chip on the other. These contacts should be checked before applying the protective glob-top because TAB-bonds without contact may be rebonded. The quality check can be put into practice by taking the chip into operation, a minimal set of essential connectivity has been elaborated with the chip designers towards this end. A probe card, that is typically chosen as a good solution for operating a chip without wirebonding, cannot be used for this test because it only works in combination with a wafer prober that assures alignment and positioning. The STS-module (STS-XYTER + microcable + sensor) would need to be placed on the chuck of the prober, inhibitive because of the module size and the fragility of the module. Therefore working with a test socket with Pogo Pins is an appropriate solution. The chip by itself is placed into the socket that will have an opening for the microcable. Several requirements regarding the test pad size, pitch and general arrangement and balance of connections across the chip have to be taken into account. Proposals for the pad layout of the STS-XYTER are under development with consultation of *aps Solutions GmbH*. Continuative tasks for the execution of tests are the development of a modified STS-XYTER board and suitable software.

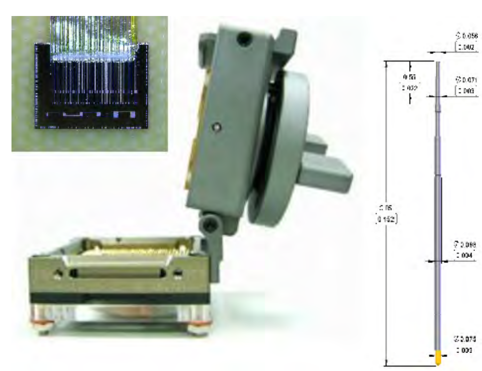

Figure 3: Test socket for ASICs.

Neutron irradiated prototype CBM-STS microstrip sensors tested for double metal or cable interconnections of the end strips

M. Singla[1], *P. Larionov*[2], *I. Momot*[2], *T. Balog*[1], *J. Heuser*[1], *I. Sorokin*[1], *and C. Sturm*[1]

[1]GSI, Darmstadt, Germany; [2]Goethe University, Frankkfurt

The Silicon Tracking System (STS), the core detector of the CBM experiment, is located in the dipole magnet to provide track reconstruction and momentum determination of charged particles from beam-target interactions. The STS will have double-sided silicon microstrip sensors mounted onto a low-mass carbon fibre support structure. The strips on one side of the double sided silicon microstrip sensors are tilted to have 7.5^0 stereo angle. This allows to reconstruct multiple hits from the same sensor at the expense of a poorer spatial resolution in vertical direction [1]. To have read out only from one sensor side, the end strips from one edge of the sensor were connected to the end strips on the other end as shown in Fig. 1. This interconnection can be provided via double metallization (DM) or by using external interstrip cables (SMwC). However, the central strips were the full strips without any kind of interconnections (region II in Fig. 1).

Test results of these prototype sensors before and after their exposure to neutron equivalent fluences of $2{\times}10^{14}$ $n_{eq}cm^{-2}$, as they are expected for the worst case scenario in the CBM experiment, will be disucssed. The sensors were irradiated at Karlsruhe Institute of Technology (KIT), Germany.

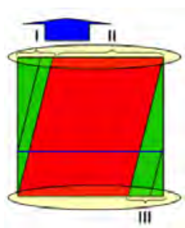

Figure 1: Sensor topology to read out inclined sensor strips.

All the measurements were performed in a refrigrator at temperatures between -5^0 C to -10^0 C to limit the radiation-induced effects on detector current and to prevent thermal runaway [2]. Four sensors were selected for the measurement of variation of leakage current with bias voltage (IV), bulk capacitance versus bias voltage (CV), and for charge collection tests for the central strips (region II in Fig. 1) and for the end strips (with these special interconnection scheme, region I in Fig. 1) with a ^{90}Sr source. In this report only the results from central strips will be discussed. The list of the sensors under test is given in Table 1 along with their sizes, thickness, types of the connections and full depletion voltage before irradiations (extracted from the capacitance-voltage measurements). These sensors were mounted in the printed circuit boards and were wire bonded to read out about 10 strips were read out for each sensor side using self-triggered n-XYTER chip.

Table 1: Specifications for the sensors under tests. The naming convention in the left column encodes the prototype generation (5 or 6), the manufacturer (H = Hamamatsu, C = CiS), the sensor height/strip length in cm (4 or 6), and the wafer number.

name CBM0-	size cm × cm	thickness μm	inter-connection	V_{fd} ±5 V
5H4-W18	6 × 4	327	SMwC	68
5H4-W10	6 × 4	331	DM	75
6C6-W14	6 × 6	293	SMwC	94
5C6-W6	6 × 6	291	DM	98

Charge collection studies were performed with ^{90}Sr for the sensors under test by applying suffieciently high reverse bias. Results are shown in Fig. 2 for all the sensors with either double metal interconnection scheme or single metal with external microcable bonded on its top p-side. As can be seen in Fig. 2, the charge collection efficiency degrades after the irradations. These sensors were also tested in-beam at COSY, Research Center Jülich, in December 2014. Before concluding on the type of the p-strip interconnection scheme, one should also consider the beamtime results about charge collection and detection efficiency of these sensors. This work is still in progress.

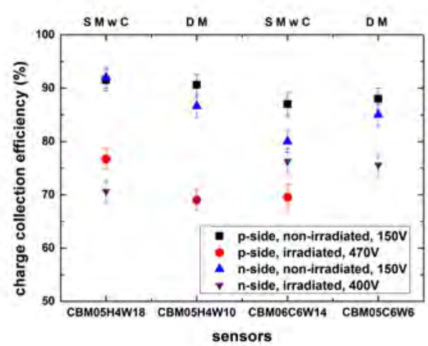

Figure 2: Charge collection results with ^{90}Sr, comparing the sensors before and after irradiation.

References

[1] J. Heuser et al., Technical Design Report for the CBM Silicon Tracking System, GSI Report 2013-4, http://repository.gsi.de/record/54798

[2] M. Moll et al., *Nucl. Instrum. Methods. A* 439 (2000) 282.

Development of a 124 mm long silicon strip sensor for the CBM STS

D. Soyk[1] *and C.J. Schmidt*[1]
[1]GSI, Darmstadt, Germany

The new segmentation of the CBM STS ladders [1] requires to design and produce a silicon strip sensor with 62 mm width and 124 mm height. This new long sensor will replace the 2 daisy-chained 62 mm sensors.

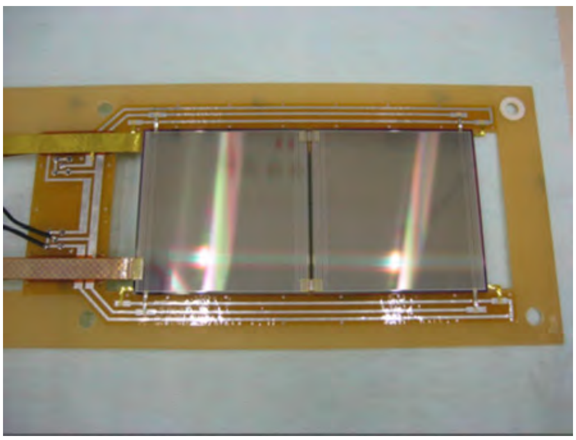

Figure 1: Two daisy-chained 62 mm sensors.

In Fig. 1 a functional prototype module with read-out of 1/8 of its channels is shown, produced by LED Technologies of Ukraine (LTU) Ltd, Kharkov, Ukraine, using two sensors 6.2 cm by 6.2 cm large compatible with 4 inch wafer technology. Between the two sensors two short daisy-chain-cables are shown. That serve to connect the strips from one sensor to the next. In the final version, all strips of the sensors must be connected. Therefore a daisy-chain-cable with the full width must be produced and bonded onto the sensors. Every sensor also needs a cross connection on the p-side that links inclined strips ending on one lateral side to a corresponding strip on the other lateral side. It is not jet finally resolved, whether such connection should be realised on an additional metal layer or with a seperate microcable. If the sensor is single-metal, additionally for each sensor a interstrip-connection-cable must be bonded on the p-side of the sensor. Together with the CiS Forschungsinstitut für Mikrosensorik und Photovoltaik GmbH, Jena, Germany the plan was developed to produce a single 124 mm × 62 mm sensor in double-side and double-metal technology on a 6 inch wafer. If it is possible to solve all technological challenges, the production of a module with 124 mm sensorheight would become much simpler. The production and assembly of two interstrip cables and the production and assembly of one daisy-chain-cable could be made unnecessary. Also the bonding process of these three cables will be avoided. This reduction of fabrication and manufacturing steps will increase reliability and yield. Additionally the replacement of the daisy-chained sensor by one sensor will reduce the assembly effort because the daisy-chained module must be installed on a special frame before it is mounted on the ladder. In Fig. 2 the layout of the wafer is shown.

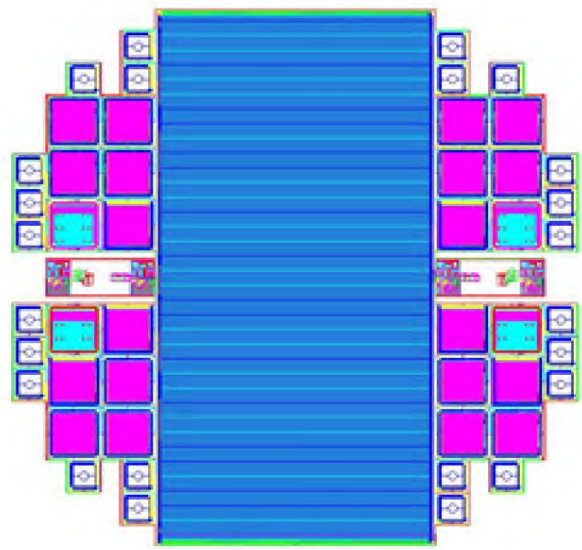

Figure 2: Layout of the 6 inch wafer with the 124 mm × 62 mm STS sensor in the middle, around the sensor CBM baby sensors and test features.

At the moment the design of the 124 mm sensor is finished and the production of masks has already started. The design of the AC- pads will follow the classification of pad layout, described in [2].

References

[1] J. Heuser et al., Technical Design Report for the CBM Silicon Tracking System, GSI Report 2013-4, Darmstadt, ISSN 0171-4546

[2] D. Soyk et al., "Silicon strip sensor layout for the CBM Silicon Tracking System", editors: V. Friese and C. Sturm, CBM Progress Report 2013, Darmstadt, ISBN 978-3-9815227-1-6

Modification of CBM micro cable stack-up

D. Soyk[1]*, C.J. Schmidt*[1]*, V. Kleipa*[1]*, and I. Sorokin*[1]
[1]GSI, Darmstadt, Germany

During several years of development of the CBM modules, the STS sensors and the CBM STS-XYTER chips were carefully studied and designed. Despite this careful evolution, the design and study of the connecting part between the sensor and the chip had not been addressed in such intensity. Some studies on the electrical behavior were performed, while all questions of cable stockage were addressed this year. In [1] the cross section of the cable - like it was used for the electrical simulation - is described. Figure 1 shows the modified cable stack-up.

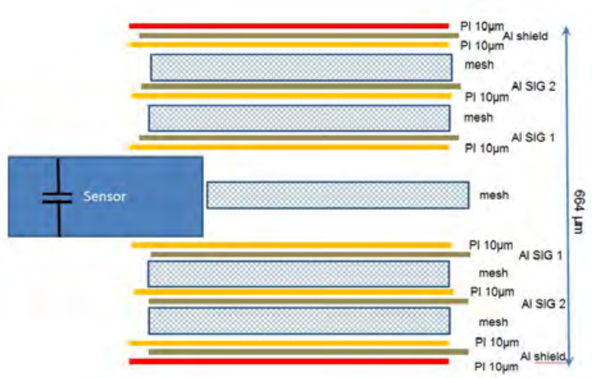

Figure 1: Schematic side view of the micro cable stack up for one CBM module. The red layer on the top and the bottom of the cable is the newly introduced insulation layer. In the middle, at the side of the sensor, the meshed layer to reduce crosstalk between the two sensor sides was newly introduced.

The geometry of the signal strands with a height of 14 μm and a width of 46 μm is kept, also the pitch between the strands remains 116 μm on each signal layer. As substrate for the strands 10 μm thick polyimide will be used. The thickness of the mesh will be kept at 100 μm, but a study is beeing done to find a mesh material with a lower mean dielectric constant. Also a additional layer of meshed material will be inserted between the microcable for the n- and p-side of the sensor. With this layer the crosstalk between the signals of both sensor sides should be minimized. The shielding layer will be modified. The thickness of the aluminum will be reduced to 14 μm (instead of 30 μm) and the polyimide will have a thickness of 10 μm (instead of 20 μm). With these changes the same aluminium polyimide film may be used for the signal layers, as well as for the shielding layers. Due to the fact that the sensors of different modules of a ladder are on different potentials, it could be an advantage to introduce a additional layer of polyimide insulation on the outside of the shielding. This allows us to keep the shielding potential for each sensor side and for each sensor in a ladder on a defined and independent level, namely the reference level of the pre-amplifier input stage. With these additional two insulating layers of 10 μm and the meshed layer in between, the total thickness of the stack is 664 μm per module.

The modified stack-up of the micro cable was already presented at the 24th CBM Collaboration Meeting in September 2014 [2]. The research for a mesh material with lower dielectric constant is ongoing. This cable stack-up will now be realized for the next module prototype.

References

[1] J. Heuser et al., Technical Design Report for the CBM Silicone Tracking System, GSI Report 2013-4, Darmstadt, ISSN 0171-4546, Fig. 4.10

[2] C.J. Schmidt, “Status of module development”, 24th CBM Collaboration Meeting, September 2014

Tooling for CBM STS module assembly

D. Soyk[1], *C. Simons*[1], *and R. Visinka*[1]
[1]GSI, Darmstadt, Germany

The CBM STS module assembly needs tooling to simplify and speed up fabrication [1]. For several assembly steps specialized assembly tools are needed. Assembly will comprise the following steps: First, two layers of microcables need to be bonded on to the STS-XYTER chip to form a "chip-cable". Second, 8 chip-cables must be bonded to the CBM STS sensors side by side for readout of the full 1024 channels for every sensor side. Additionally, on singlemetal sensors an interstrip connecting cable must be allocated and bonded on one side of the sensor. It serves to interconnect the inclined strips that end on the sensor side to form a continuous strip over the sensor. Therefore a whole set of assembly tools must be developed and - if needed - improved. To start with simplest element, the tool for the first cable layer on the chip was design, produced and tested. This first version was already shown in [1].

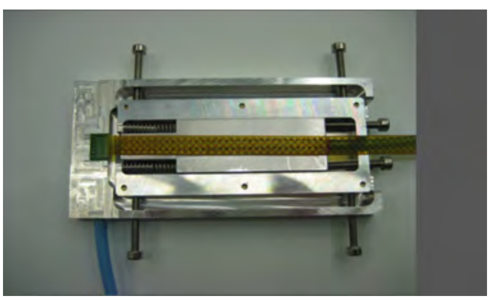

Figure 1: Tool for 1st layer on chip.

In Fig. 1 the improved version is depicted.It has small bumps to avoid crashes between the bond needle and the tool. This change increases the safety of operations and will be an advantage for the mass production by reducing the machine downtime due to such crashes. The chip and the cable in this design were still held by vacuum and manipulated via a bottom-side mechanics. Second, a tool for bonding of the second layer of the micro cable to the chip was designed.Because of the presence of the first layer, already bonded and glued to the chip, the second cable layer needs to be mounted from the top side. The chip is still fixed from the bottom-side, but the jig for micro cable mounting is now above it. This does increase the height of the tool, but this height is not a showstopper, because the operating range of the tab-bond needle is not above the cable but the chip. See Fig. 2.

To assembly the microcables with the chips to the sensor a third tool with a movable bottom-side sensor holder and a top-side mechanics for the microcables was designed. It is shown in Fig. 3.

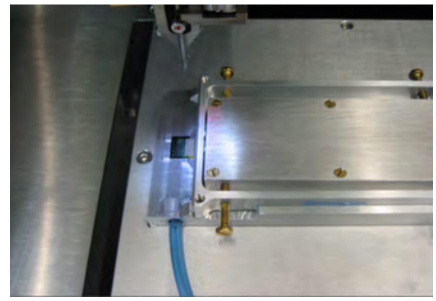

Figure 2: Tool for 2nd layer on chip.

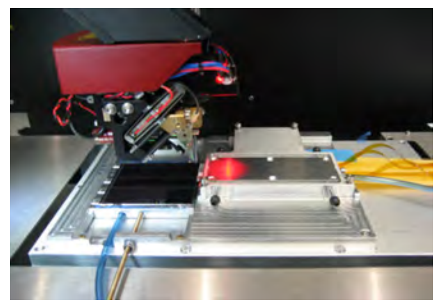

Figure 3: Tool for 1st and 2nd layer on sensor.

It turned out that a movable sensor holder is not the best way for this assembly step, because the flimsy microcables are destroyed if they're moved too strong. An improvement of this tool is in work. Fortunately it also turned out, that this tool could be used to bond the interstrip connecting cables on the p-side of the sensor (see Fig. 4).

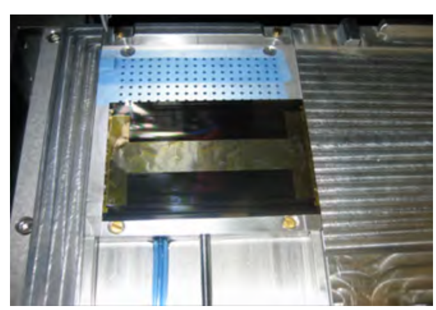

Figure 4: Insterstrip cable on sensor.

References

[1] D. Soyk et al., "Development of a tool for CBM STS module assembly", editors: V. Friese and C. Sturm, CBM Progress Report 2013, Darmstadt, ISBN 978-3-9815227-1-6

Ring-Imaging Cherenkov Detector

Mirror misalignment control system techniques and prototype

J. Bendarouach[*1], *C. Höhne*[1], *and T. Mahmoud*[1]
[1]Justus Liebig Universität, Gießen

An important aspect to guarantee a stable operation of any RICH detector is the alignment of the mirrors. Two methods have been studied in depth, one developed by the COMPASS experiment and called CLAM and the other developed by the HERA-B experiment.

The principle of the CLAM (Continuous Line Alignment Monitoring) alignment procedure [1] is to monitor over time mirror displacements via photographic images. A grid of retro-reflective stripes, forming a regular grid-shaped pattern and of photogrammetric target dots, is glued on the inner part of the RICH entrance window. A set of four cameras are arranged at the edges of the entrance window and around each camera a set of three LEDs are fixed to illuminate the grid through the mirrors (Fig. 1). A first qualitative look at mirror displacements can be

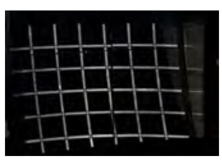

Figure 1: Reflection of the grid on the RICH mirrors. Here the lines do not appear broken at mirror edges, hence the mirrors are correctly aligned.

given, when looking at the continuity of the reflected stripes. Indeed if a mirror is displaced with regard to one of its neighbor, then stripes will appear broken or cut into two shifted parts at the mirror edges. According to the shift, the relative misalignment of the corresponding mirror parts can be deduced. A second quantitative observation can also be obtained with this setup, when using photogrammetry. From the target centers positions relative to external marked reference points, the orientation of mirrors can also be extracted. This shows consequently the relative orientation of each mirror with its neighbors [2]. A downscaled version has been implemented in the RICH prototype detector and tested at CERN. Analysis of the data is undergoing.

The second method, developed by the HERA-B experiment and which has also been used by the LHCb experiment [3, 4], relies on data. It consists of determining ring displacements from a fit of recorded data with a reference equation. In the cases of these experiments, two subsets of mirrors are used (spherical and planar), which is not the case for the CBM RICH detector. In this method Cerenkov

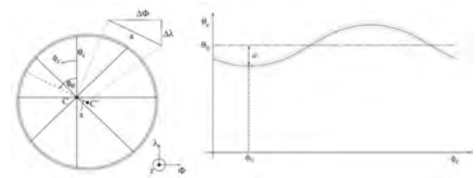

Figure 2: Variations of θ_c with regard to Φ_c in the case of a misaligned mirror system.

angles for given photons are measured. They are defined as the distance between any photon hit on the PMT plane and the particle hit, from which the photon was emitted and which is extrapolated from its track (Fig. 2). If the system is not perfectly aligned, the particle hit will not coincide with the ring center. It has been shown that the variation in the Cerenkov angle θ_c with regard to the azimuthal angle Φ_c has a behavior similar to:

$$\Delta\theta_c = (x \cdot \cos(\Phi_c))(y \cdot \sin(\Phi_c)) \qquad (1)$$

where x and y correspond to the misalignment angles on a mirror. Only unambiguous photons, i.e. photons which are reflected on a unique mirror part, regardless of its emission point on the particle track in the radiator, are taken into account for the study. The recorded data are displayed as a histogram, representing the difference in Cerenkov angle measurements depending on the azimuthal angle. A Gaussian fit is implemented for each slice Φ_c to determine its peak, and the resulting distribution can be fitted to equation 1, yielding the parameters of misalignment x and y.

References

[1] S. Costa et al., Nucl. Instr. Meth. Phys. Res. **A 553** (2005) 135

[2] L. Steiger et al., Nucl. Instr. Meth. Phys. Res. **A 639** (2011) 219

[3] A. Gorišek et al., Nucl. Instr. Meth. Phys. Res. **A 433** (1999) 408

[4] C. Blanks, Nucl. Instr. Meth. Phys. Res. **A 639** (2011) 215

* Corresponding author

Muon Detection System

Neutron dose test of active LVDB component to be used for CBM-MUCH detector, using K-130 Cyclotron at VECC

V. Jain[1], *J. Saini*[1], *A. K. Dubey*[1], *S. Chattopadhyay*[1], *R. Ravishankar*[1], *T. Bandyopadhyay*[1], *S. Mandal*[1], *J. Mitra*[1], *and P. Koczon*[2]

[1]VECC, Kolkata; [2]GSI, Germany

Introduction

A GEM based detector system is being developed at VECC, Kolkata for use as muon tracker in the Compressed Baryonic Matter (CBM) experiment at the upcoming FAIR facility at Germany [1][2]. MUCH adds to the neutron background immensely. As per FLUKA calculations [3], it is estimated that the electronics will have to withstand a high neutron dose of the order of 10e11 Neq/cm2 for lifetime of CBM-MUCH detector. To see the effect of the neutron on the components to be used near the detector, we have performed neutron dose effect with secondary neutrons by bombardment of proton on thick Ta target using Cyclotron at VECC.

Neutron irradiation test

The aim of the neutron tests is to find any physical or characteristics damage on the regulator. In this direction, we conducted the first such test of LTC3605 voltage regulator in VECC cyclotron. As shown schematically in Figure 1, a 15 MeV proton beam with the beam current of 4uA average was bombarded on a thick Ta target to get the secondary neutron. This experiment was performed for about 10days to achieve the required neutron dose. For efficiency measurement over time, input and output voltage and current was periodically moinitored using multimeter and power supply display as shown in Figure 2.

Figure 1: Schematic of the neutron test setup at VECC Cyclotron.

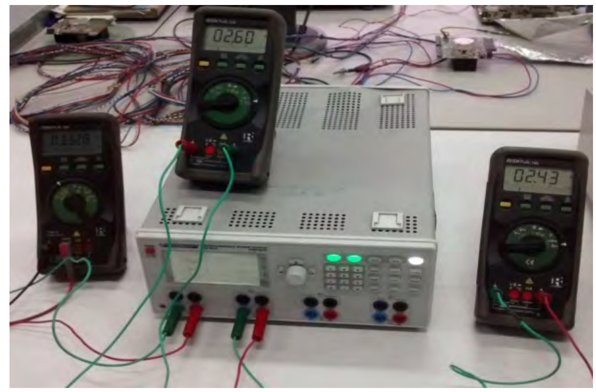

Figure 2: Voltage and current monitoring setup.

Neutrons test results

Figure 3 shows the efficiency of both Gamma radiated and non-irradiated voltage regulator with respect to number. of neutrons falling on the regulator. The plot shows that the efficiency of the regulator is almost stable throughout the irradiation of 7.1x 1010 neutrons/cm2.

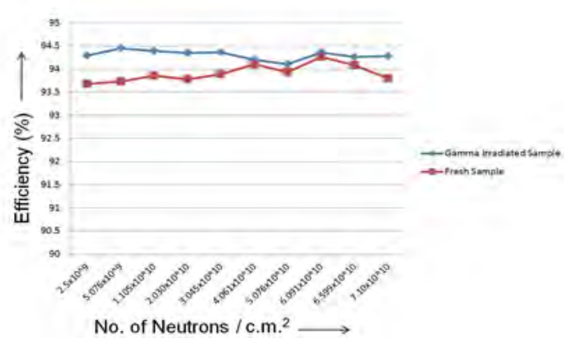

Figure 3: Efficiency vs. No. of neutrons/Sqcms

References

[1] CBM Technical Design Report 2013 (TDR)

[2] A.K. Dubey, et. al, DAE Symp. On Nucl.Phys. vv, ppp (2010), Anna Kiseleva, P.P. Bhaduri, et.al. 85, 211-216 (2011) (2013) 56

[3] Senger, CBM Progress Report 2012, p26

[4] “Conversion coefficient for use in radiological protection against external radiation” ICRP Publication 74

Total dose effect test of active LVDB component with 60Co Gamma chamber, to be used for CBM-MUCH detector

V. Jain[1], *J. Saini*[1], *A. K. Dubey*[1], *S. Chattopadhyay*[1], *A. Saha*[2], *and P. Koczon*[3]
[1]VECC, Kolkata; [2]UGC-DAE Consortium for Scientific Research, Kolkata; [3]GSI, Germany

Introduction

A GEM based detector system is being developed at VECC, Kolkata for use as muon tracker in the Compressed Baryonic Matter (CBM) experiment at the upcoming FAIR facility at Germany [1][2]. The Muon Chambers (MUCH) consists of alternating layers of six absorbers and detector stations. The harsh radiation dose in CBM owing to high hadronic environment poses severe constraints on the design and selection of the electronic components to be used along with the detectors. To make sure that selected components will work in this environment, we have performed Gamma dose testing one of the proper component in 60Co chamber at UGC-DAE Consortium for Scientific Research, Kolkata.

Gamma irradiation test

The most upstream detector station of MUCH will receive highest dose of 300Gy/2months as was simulated by FLUKA calculation [3] and total CBM-MUCH operating period in 10 years is expected to be of 20 operational months [1], and therefore the CBM readout electronics are to be made to withstand the total dose of 315 KRad.

Figure 1: Gamma irradiation testing setup.

Figure 1 shows the 60Co Gamma chamber has been used as a irradiation source. The equivalent dose rate inside this chamber was of 3.1kGray/hour. Two number voltage regulators were inserted in this chamber, one with load and another without load. As the chamber was a closed enclosure, so there is a possibility of temperature rise due to load. Hence a small fan arrangement was made inside the chamber to run continuously and additionally we have taken out chamber every 10 minutes to further cool it down to ambient room temperature. Input and output voltages and currents were measured every 10minutes. The efficiency which is calculated by the ratio of output power to the input power of voltage regulator, was measured with respect to the cumulative gamma dose.

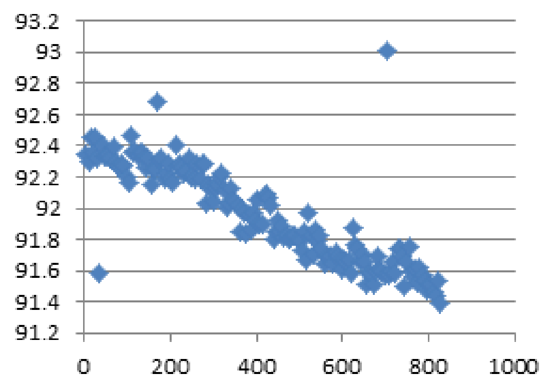

Figure 2: Efficiency vs. Gamma Dose.

Gamma irradiation Results

Figure 2 shows the efficiency of voltage regulator with cumulative gamma dose up to 8kGy. The efficiency of voltage regulator in the entire irradiation was dropped down from 92.5 percent to 91.5 percent, which is well within the acceptable range of current design of low voltage distribution board (LVDB) to be used for CBM-MUCH electronics.

References

[1] CBM Technical Design Report 2013 (TDR)

[2] A.K. Dubey, et. al, DAE Symp. On Nucl.Phys. vv, ppp (2010), Anna Kiseleva, P.P. Bhaduri, et.al. 85, 211-216 (2011) (2013) 56

[3] A. Fasso, A. Ferrari, J.Ranft and P.R. Sala, "FLUKA: a multi particle transport code",CERN-2005-10

A contribution to the GSI scientific report 2014

Suman Sau *[1], *Swagata Mandal* †[2], *Jogendra Saini*[2], *Amlan Chakrabarti*[1], *Susanta Paul*[2], and *Subhasis Chattopadhyay*[2]
[1]University of Calcutta; [2]Variable Energy Cyclotron Centre ; India

Introduction

A Gas Electron Multiplier (GEM) based detector system is being developed at VECC, Kolkata for use as muon tracker in the Compressed Baryonic Matter (CBM) experiment at the upcoming FAIR facility at Germany[1] Muon Chamber (MUCH) is used to detect low momentum muons in an environment of high particle densities. Detecting these set of particles require fast and radiation-hard detector systems, which are positioned in dense arrangements and to be readout by radiation hard front-end electronics (FEE). To read such high data rate, CBM requires precise time synchronization, compact hardware, radiation tolerance, self-triggered front-end electronics. For efficient data aggregation from these FEE's, GBTx (developed by CERN) is planned to be used as a bridge to the Data Acquisition (DAQ) system. As this ASIC is radiation hard, we are restricted to bring these GBTx ASICs to India. This article focuses on the implementation of this GBTx into a FPGA (Field Programmable Gate Array) board for CBM-MUCH detector.

CBM Network and DAQ Structure

The simplified read out architecture of MUCH to be used in CBM experiment is shown in Figure 1 In Muon Chamber fast and highly granulated GEM detector is to be used. The MUCH-XYTER a radiation hard ASIC used for signal detection from MUCH in the CBM environment. The self-triggered ASIC provides both timing and energy information for each incoming signal in its channel. MUCH-XYTER is connected to the Gigabit Transceiver (GBTx) in the back end through SPI-like e-links. The GBTX is a radiation tolerant chip that can be used to implement multipurpose high speed bidirectional optical links for high-energy physics experiments[2]It is connected with Data Processing Board (DPB) through optical fiber. DPB will be placed outside the irradiated area and more complex electronic systems like commercial-off-the-shelf (COTS) FPGA and faster optical links can be used in this layer[3] DPB will be connected to the First Level Event Selector interface Board (FLIB) through 10 Gbps optical link. Finally FLIB will transmit data to the computer using PCIe. As a Part of the development of DAQ here we have concentrated in the implementation of GBTx in FPGA. In the encoder block single error correcting (15, 11) Reed-solomon encoding is used. Input data to the scrambler is 84 bit. When data will enter into the encoder block it will append with four bit header. This channel coding can correct maximum eight symbols consecutively.Output of the encoder is 120 bit data. Interleaving is the reordering of data that is to be transmitted so that consecutive bytes of data are distributed over a larger sequence of data to reduce the effect of burst errors. Data width after interleaver block remains 120 bit. But this 120 bit data cannot be send at a time so a Gearbox is used. It will divide 120 bit data into three 40 bit words and send it to Multigigabit Transceiver (MGT). GBTx frame sent to the transmitter consists of four bit header, four bit data for slow control, 80 bit raw data, and 32 bit data for forward error correction. The GBT frame is shown in Figure 2. Receiver side of GBTx performs just opposite jobs like deinterleaving, decoding and descrambling. Only the framealigner block in receiver side is not present in transmitter side. It consists of:-Pattern Search block, Bitslip Counter, Right Shifter, Write Address generator. Pattern search block continuously check whether proper four bit header is received or not. Until the proper header is received bitslip counter continuously change its value. After receiving correct header write address generator will generate address in the RAM where 40 bit data will be written

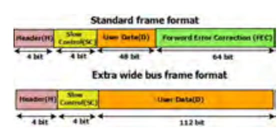

Figure 2: GBTx Frame format

Implementation on FPGA

For implementation of the GBTx code, we have used xilinx KC705 board. Here two clocks are used:- FPGA fabric clock whose frequency is 156.25 MHz and MGT reference clock whose frequency is 120 MHz. FPGA fabric clock is generated internally from Si570 3.3V LVDS I2C Programmable Oscillator. MGT reference clock has to be very low jitter clock. MGT reference clock has been given from External jitter cleaned clock source CDCE62005 from Texus instruments. GBTx is tested both in standard and latency optimized mode. In VECC we are also captured the data from GBTx in computer using PCIe and SGDMA.From the figure 5 it is observed that MGT transceiver is ready and working properly. We have received the same data that we have transmitted.

* sumansau@gmail.com
† swaga89@gmail.com

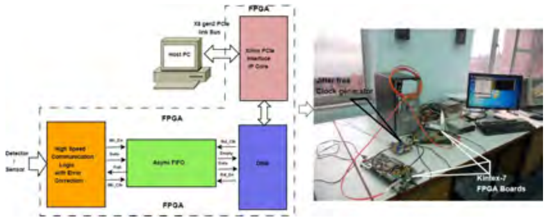

Figure 1: DAQ Chain

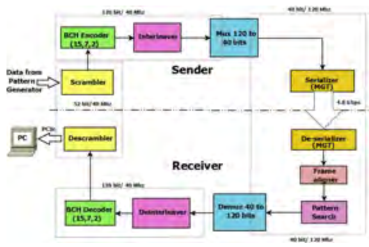

Figure 3: Internal Architecture of GBTx

Gigabit Transceiver (GBTx)

The simplified block diagram of GBTx is shown in Figure 3. Here pattern generator and pattern checkers are used for testing purpose. But when it is connected with the read out chain they will replace with fifo which will store data from MUCH-XYTER. Scrambler is mainly used for accurate timing recovery in the receiver side. It also reduces inter carrier interference.

References

References

[1] CBM Technical Design Report 2013(TDR)

[2] 2] P.Moreira, J.Christiansen and K.Wyllie," The GBTx Link Interface Asic," v1.7 Draft, Oct.2011.

[3] K.Kasinski, W.Zabolotny and R.Szczygiel, "Interface and protocol development for STS read-out ASIC in the CBM experiment at FAIR," in Proc. Photonics Applications in Astronomy, Communications, Industry, and High-Energy Physics Experiments, 2014.

Transition Radiation Detector

Two-dimensional MWPC prototype for CBM TRD*

A. Bercuci[1], *D. Bartoş*[1], *G. Caragheorgheopol*[1], *V. Cătănescu*[1], *F. Constantin*[1], *M. Petriş*[1], *and M. Petrovici*[1]

[1]IFIN-HH, Bucharest, Romania

Introduction

The signal induced on a segmented conductive electrode is used in a large number of MWPC applications for position information. Additionally, the firing anode can be used for orthogonal position information at an increased operational cost. The draw back of such procedure is the poor localization along the wire and the impossibility to operate in conditions of high local occupancies and counting rates. In the current report the performance of an innovative geometry of the read-out electrode is presented. The $2D$ information can be extracted in high fluxes without additional anode read-out channels.

The TRD MWPC for CBM

The TRD developed in Bucharest for the CBM experiment [1] is characterized by a $4\ mm$ drift and a $2 \times 4\ mm$ amplification regions and wire pitches of $1.5\ mm$ for the cathode and $3\ mm$ for the anode wires (see Fig. 1 left). The conductive electrode is segmented in triangular shaped pads of $7.3 \times 27.7\ mm^2$ and $0.2\ mm$ spacing arranged as in Fig. 1 right with respect to the anode wires.

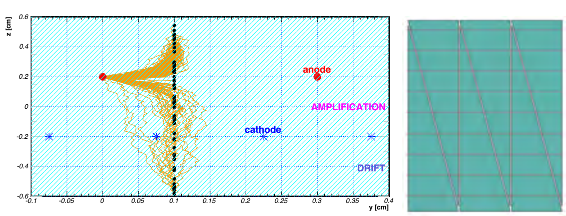

Figure 1: Active volumes (drift, amplification) and elements (anode, cathode wires and the pad plane structure) as well as signal formation in the TRD as simulated in Garfield++ [2].

The Local Anode Identification method

Due to varying cross section of pads with respect to anode wires in our current set-up and localization of the induced signal the Pad Response Function (PRF) varies with the position of firing anode wire along the pads. Thus one can build an Anode Response Function (ARF) for anode identification. In Fig. 2 left the method is tested using an uniform illumination of the TRD detector with a ^{55}Fe source. For each PRF value nine maxima are found corresponding to the anodes covered by a pad-row. Each local

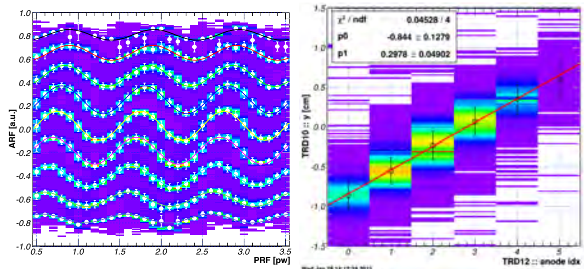

Figure 2: ARF correlations with PRF as measured with TRD prototype for a uniform illumination with ^{55}Fe (left) and with the position measurement by a reference TRD for MIPs (right) respectively. The slope of the fit ($p1$) gives the measured distance beteen anodes in cm.

maxim is fitted and the mean and sigma parameters of the Gaussian distribution are extracted (see markers on Fig. 2 left and the sin interpolation). A very good separation between each curve is obtained for the whole pad height.

In November 2014, the TRD prototype operated with Xe/CO_2 $(80/20)$ was tested with MIPs at CERN-PS. To estimate the resolution of the ARF method a reference position sensitive TRD was mounted orthogonal to it. The reference detector was operated in the rectangular shaped pads geometry for good position resolution across pads. The correlation between position measurements in the reference detector and anode identification by ARF is shown in Fig. 2 right. The measured distance of $2.98 \pm 0.05\ mm$ between anode wires corresponds to the designed pitch of $3\ mm$. The measurement across pads is performed for the time being using the parring of triangular pads. A resolution of $\approx\ 500\ \mu m$ is obtained for ^{55}Fe position scan operated with Ar/CO_2 $(80/20)$ and FASP v0.1 [3] FEE.

Conclusions

It was demonstrated that the usage of a varying PRF along pads can provide good local anode identification. The method opens the possibility of using reduced *effective* pad geometries with implications in position resolution at constant read-out costs and experimental material budgets.

References

[1] M. Tarzila et al., CBM Progress Report (2012) 80.

[2] Garfield++ http://garfieldpp.web.cern.ch/garfieldpp

[3] V. Catanescu, CBM 10^{th} Collaboration Meeting Dresden, Sept 25-28, 2007

* Work supported by Romanian ANCSI/CAPACITATI Modul III Contract F02 and NUCLEU Project Contract PN 09370103.

Fast Analog Signal Processor FASP-02 *

V. Cătănescu[1]
[1]NIPNE, Bucharest, Romania

A second version of FASP ASIC dedicated for high counting rate CBM TRD prototypes developed by Bucharest group [1] - [4] was designed and produced. Similar to the first version [5], it is based on AMS 0.35 μm N-well technology. The die size is 4.65 mm x 3.45 mm. Besides the main features of its previous version, new ones are implemented in FASP-02, considering the specific architecture of the fast TRD prototypes mentioned above and the results obtained in the tests carried out in the meantime. The most relevant new features are:

- 16 input channels
- selectable positive or negative polarity of the input signals
- multiplexed analog outputs, i.e. selectable semi-Gaussian or flat top
- channel wise clock synchronized logic time for individual ADC
- channel wise logic time signal generated at the selectable threshold level or at the signal peak detection, accordingly to the user setting
- selectable trigger of neighboring channels relative to the one with the signal over the threshold
- tilted and rectangular pairing of the triangular pads

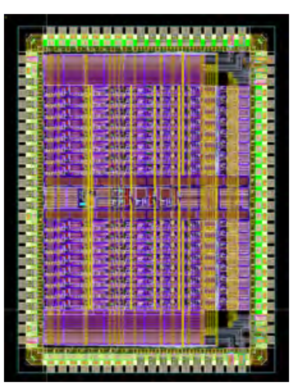

Figure 1: Photo of the FASP-0.2 ASIC

Good response to double pulse, to high pulse rate, fast recovery from positive/negative overload, base line restoration due to pulse rate shift, detector leakage current, temperature and voltage supply variations are also implemented to FASP-0.2 ASIC. Additionally the self trigger capability working with a new channel wise input/output interface enhances the performances of the new FASP-0.2 ASIC.

Table I

SPECIFICATION	FASP-0.1	FASP-0.2
Average pulse rate	>300kHz	>300KHz
Detector pad capacitance	25pF	25pF
Number of analog channel	8	16
Input polarity (1bit selection)	positive	Positive/negative
Channel pairing	no	yes
Charge input range	0.15fC...165fC	0.15fC...165fC
Input type	DC single ended	DC single ended
Channel gain	6.2mV/fC	6.2mV/fC
Shaping time /(1bit selection)	20ns and 40ns /yes	100ns/n.a
Analog output type (1bit selection)	semi-Gaussian or peak-sense	semi-Gaussian or peak-sense
Analog output polarity	Positive (single ended)	Positive (single ended)
Analog output voltage swing	0....1V	0....1V
Analog output DC voltage level base line (cont.adj)	0.2V....1V	0.2V....1V
Semi-Gaussian output FWHM	62ns/110ns	290ns
Peak-sense output plateau	typ. 400ns (cont. adj)	typ. 400ns (clock dependent)
Channel ENC (Cdet=25pF)	980e (St=40ns)/1170e (St=20ns)	940e
Crosstalk (max. signal in only one channel, no signals in others)	0.5%	0.012%
Crosstalk (max. signal in 15 ch. no signal in one channel)	0.7%	0.022%
Self trigger capability: variable threshold (cont. adj)	0....165fC	0....165fC
Logic common event output	negative 20ns width	negative 20ns width
External clock synchronization	no	max. 50MHz
Logic signal channel wise, clock synchronized, output	no	yes
Channel synchronized logic signal occurrence (1bit selection)	n.a	to threshold level / to maximum amplitude
Channel-wise synchronized logic signal for semi-Gaussian output	n.a	negative 20ns to threshold level/ to maximum amplitude
Channel-wise synchronized logic signal for peak-sense output	n.a	neg. 20ns to threshold level/ neg. 14 clock cycle to max. ampl
Channel neighbors trigger enable/disable	n.a	yes

The shaping time for FASP-0.2 is increased to 100 ns in order to accomplish the requirements of the new TRD prototypes with a drift region of 4 mm. The crosstalk is about ten times lover compared to FASP-0.1. The main specifications for FASP-0.1 and FASP-0.2 can be followed in Table I, where the new features and the modified specifications for FASP-0.2 can be followed.

References

[1] M. Petriş et al., Nucl. Instr. Meth. A,**714**(2013), 17

[2] M. Petriş et al., Nucl. Instr. Meth. A,**732**(2013), 375

[3] M. Târzilă et al., CBM Progress Report (2012) 80

[4] A. Bercuci et al., This Report

[5] V. Cătănescu, CBM 10^{th} Collaboration Meeting Dresden, Sept 25-28, 2007

* Work supported by EU-FP7/HP3 Grant No 283286 and Romanian NASR/CAPACITATI-Modul III contract RO-FAIR F02 and NASR NUCLEU Project PN09370103

Free running acquisition system for Transition Radiation Detectors - in beam tests -*

F. Constantin[1], *D. Bartoş*[1], *A. Bercuci*[1], *G. Caraghergheopol*[1], *V. Cătănescu*[1], *M. Petriş*[1], *M. Petcu*[1], *and M. Petrovici*[1]

[1]Horia Hulubei National Institute for Physics and Nuclear Engineering, Romania

The present acquisition system was developed as a test benchmark of a free running concept for high counting rate TRDs [1] based on FASP ASIC [2] and analog converters of the type foreseen to be implemented in a later stage in a hybrid updated version of FASP analog processor. This version can operate 64 TRD readout channels with a sample rate of 2 Msps and 12 bits resolution MAX 11105 ADCs. The system is based on a Spartan 6, SP601 evaluation board and a custom designed board for MAX 11105 analog converters [3,4]. Two such systems were built, each of them processing data from 32 pads. In order to merge the correlated data between several subdetectors, a synchronization signal is used. The main tasks assumed by the system are: data unpacking from the 2 x 32 MAX 11105 and synchronisation management, capture of the MBS_sync signal from a MBS (Multi-Branch System) system [5], packing the data and Ethernet transmission through UDP protocol. The mixed acquisition system, a trigger driven (MBS) and the free running, generates acquisition files which are later paired by a dedicated software. Data for TRD were collected based on the free running system described above while Cerenkov and Lead Glass by information was taken by the MBS system. The correctness of the data synchronisation is proved by the electron and pion pulse height distributions at three different momenta presented in Figures 1, 2 and 3.

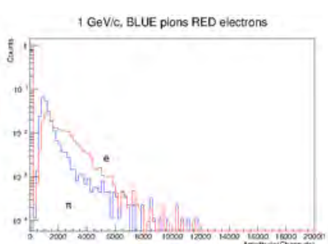

Figure 1: Pulse height distributions for electrons (red) and pions (blue) at 1 GeV/c momentum

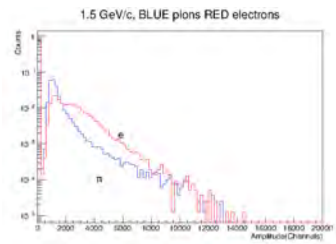

Figure 2: 1.5 GeV/c momentum

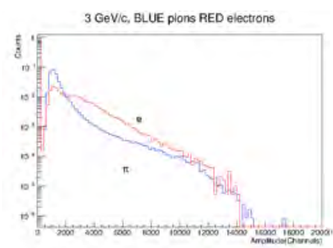

Figure 3: 3 GeV/c momentum

References

[1] M. Petris et all Two dimension position sensitive real size CBM-TRD prototype. PHN-SIS18-ACC-38

[2] V.Catanescu, CBM 10th Colaboration Meeting, Sept. 25-28,2007, Dresden

[3] http://www.xilinx.com/publications/prod_mktg/sp601_product_brief.pdf

[4] http://www.maximintegrated.com/en/datasheet/index.mvp/id/6419

[5] https://www.gsi.de/work/fairgsi/common_systems/csee_electronics/datenverarbeitung/datenerfassung/mbs.htm

* Work supported by Romanian NASR/CAPACITATI-Modul III contract F02 and NUCLEU contract PN09370103

Progress in TRD readout using SPADIC 1.0

M. Krieger and P. Fischer
ZITI, University of Heidelberg, Germany

After all features of the SPADIC 1.0 chip had been verified to be functioning in the laboratory [1], the next steps in the development of a readout system for the CBM transition radiation detector have been taken.

During this year's common beam time of several CBM detector subsystems at CERN [3], the latest "rev. B" front-end boards [2] were used to read out TRD modules (depicted in Fig. 1). The design of the front-end boards including the packaged chips has shown to be a viable solution, and a few aspects concerning the low voltage supply and reset mechanism have been identified to be improved in future revisions.

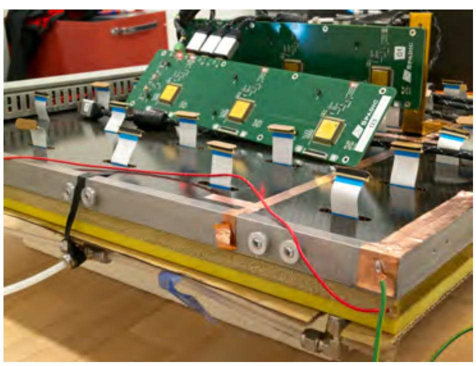

Figure 1: Two SPADIC "rev. B 3x" front-end boards on a TRD module.

Once a proper ground connection between the various components of the detector and readout setup had been found, the noise contained in the measured signals could be reduced to levels not much higher than what had been observed under laboratory conditions without any detector connected to the readout electronics (equivalent noise charge: $2.0 \pm 1.0\,\mathrm{ke}^-$ vs. $0.9 \pm 0.1\,\mathrm{ke}^-$). Examples of measured TRD pulses and a histogram of pulse amplitudes can be seen in Fig. 2.

A significant effort was the development of software components necessary to operate the SPADIC chips in the beam test environment. These include

- libraries to extract the SPADIC data from the *timeslice* objects provided by the FLESnet data acquisition system [4] and to decode the SPADIC data stream into a format understood by the CBMroot analysis framework,
- user interfaces for controlling and monitoring the SPADIC configuration, and

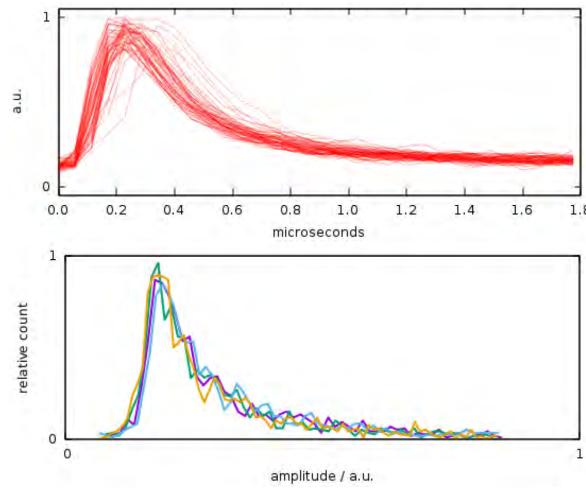

Figure 2: Top: An overlay of approximately 50 recorded pulse shapes. The horizontal axis covers a time interval of 1.8 microseconds, corresponding to 32 samples taken at a rate of 17.5 MHz. Bottom: Distribution of pulse amplitudes for four different channels.

- various automation scripts, for example to load previously determined configurations or to equalize baseline levels between channels.

The operation of the chips was complicated by two known bugs in the SPADIC 1.0 implementation. These are an instability in the charge sensitive amplifier and a glitch in the serial data output. In the near future, an intermediate version 1.1 of the ASIC will be produced, where among a few other smaller improvements these two problems will be solved, but which otherwise remains compatible to SPADIC 1.0 so that the existing infrastructure can be reused in upcoming beam tests.

References

[1] M. Krieger and P. Fischer, "Commissioning of the SPADIC 1.0 Amplifier/Digitizer Chip", CBM Progress Report 2013, p. 72

[2] M. Krieger, "Design of new SPADIC front-end boards for TRD readout", CBM Progress Report 2013, p. 73

[3] C. Bergmann, "Common CBM beam test of the RICH, TRD and TOF subsystems at the CERN PS T9 beam line in 2014", this report

[4] D. Hutter, "CBM FLES input interface developments", this report

Construction of a new CBM-TRD prototype with carbon frame, alternating wires and without drift region in Frankfurt

M. Tanha, W. Amend, A. Arend, A. Arend, C. Blume, P. Dillensegger, S. Gläßel, and F. Roeth
Institut für Kernphysik, Goethe-Universität Frankfurt, Germany

A new TRD prototype based on a thin Multi Wire Proportional Chamber (MWPC) without a drift region and with carbon frame was designed at the Institute for Nuclear Physics in Frankfurt (IKF) and tested in the test beam at CERN-PS in November 2014. According to this design, two identical full-size prototypes in dimensions of $586 \times 580 \times 38.5\text{mm}^3$ were developed with a pitch of 2.5 mm between field and sense wires. Cathode (field) wires made of Cu-Be with a diameter of 80 μm are placed between gold-plated tungsten anode (sense) wires with a diameter of 20 μm. The gas gap region, distance between entrance window and pad plane, is 3.5+3.5 mm (see figure 1).

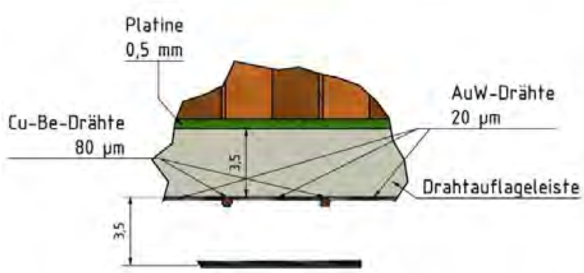

Figure 1: Schematic drawing of alternating wires, their pitch and diameters.

Applying cathode wires with alternating HV (alternating wires) has an improving result as it reduces the effect of a deformation of the cathode plane, which distorts the gas gain inside the detector via electric field deformation [1].

The MWPC with thin and symmetric geometry (3.5+3.5 mm) provides faster signal collection and efficient e/π separation, which is desired in CBM experiment [2]. The carbon frame instead of aluminium or vetronit frame provides optimum mechanical properties, low thermal expansion, high friction resistance and low material budget. Figure 2 shows the technical drawing of the prototype with the aforementioned components.

Figure 3 shows the gas feed through that is embedded inside the frame in the corners, thus it meets the structural conditions of TRDs, which have to be adjusted to each other's.

The data from the CERN-PS test beam in November 2014 are currently being analysed. The development of a large size ($1.0 \times 1.0\text{m}^2$) prototype of the TRD is planned at the IKF.

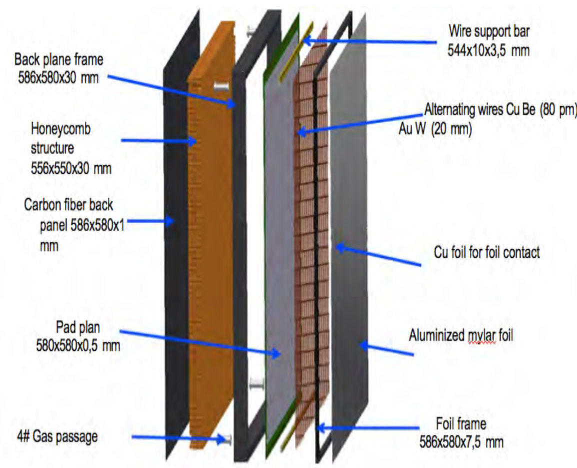

Figure 2: Technical drawing of a TRD prototype with alternating wires and carbon frame.

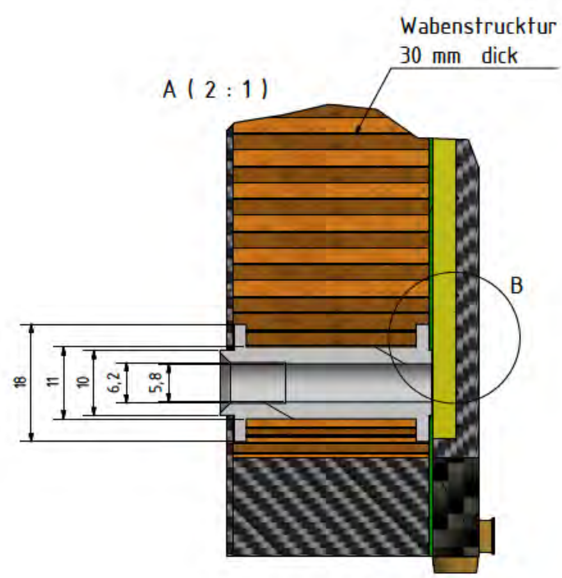

Figure 3: The gas feed through inside the frame.

References

[1] S. Gläßel, CBM Progress Report 2013, p. 70

[2] E. Hellbär, CBM Progress Report 2012, p. 54

Time-of-Flight Detector

Results from a heavy ion beam test @ GSI *

I. Deppner†[1], *N. Herrmann*[1], *P.-A. Loizeau*[1], *C. Simon*[1], *C. Xiang*[1,2], *M. Ciobanu*[3], *J. Frühauf*[3], *M. Kis*[3], *and the CBM-TOF working group*

[1]Physikalisches Institut Universität Heidelberg, Heidelberg, Germany; [2]Institute of Particle Physics, Central China Normal University, China; [3]GSI, Darmstadt, Germany

das ist nur eine Dummy-Version

The CBM Time-of-Flight-wall will be composed of Multi-gap Resistive Plate Chambers (MRPCs) [1]. In order to approach to a final MRPC design several counters from different groups were tested in October 2014 in a heavy ion test beam time at the Hades-cave GSI. A Ca beam of 1.9 AGeV beam energy was used to produce a spray of scattered particles by hitting a 5 mm thick lead target. Therefore a full illumination of the counters has been achieved which is extremely important for determining the counter properties under real battle condition. However, the targeted particle flux was not achieved for different reasons. The setup consist of two parts. An upper part close to the beam line containing the counters under test and a reference MRPC. The counters under test were a narrow strip prototype from Bucharest (called Buc3013) and a PAD-MRPC from Tsinghua, China. They were mounted in an exchangeable way. The stack of counters was sandwiched by plastic scintillator readout by two PMTs. The measured flux at this position was about 1 kHz/cm^2. The lower part of the setup contained again a counter under test, a reference MRPC and two plastic scintillator. The counter under test was a full size prototype from Heidelberg (called HDMRPC-P2). After half of the beam time it was exchanged by a strip counter from Tsinghua University. This two counters have similar dimensions and the same pickup electrode geometry. However they differ in the construction. The measured flux at this position was about few hundred Hz/cm^2. Figure 1 depicts the two layers of the setup.

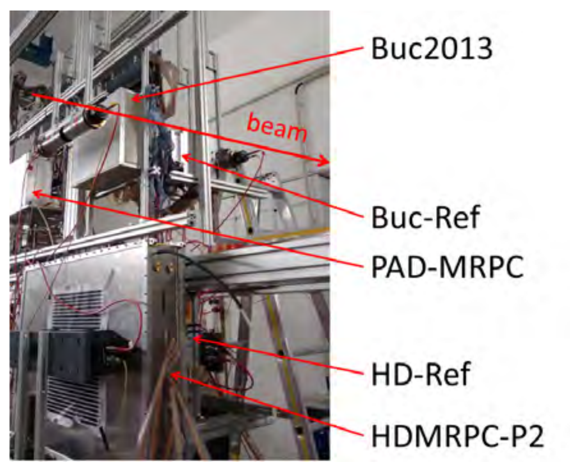

Figure 1: 3D drawing of the outer CBM ToF-wall as designed for the start version of CBM. For details see text.

References

[1] I. Deppner et al, Nucl. Instrum. and Methods A, Volume 661, Supplement 1, 2012, Pages S121 - S124

[2] M. Ciobanu et al, PAD-6 and PADI-7, new prototypes for CBM ToF, this Report

[3] J. Frühauf et al, Hardware Developmant for CBM ToF, this Report

[4] I. Deppner et al, Journal of Instrumentation. 10/2012; 7(10). DOI:doi:10.1088/1748-0221/7/10/P10008

[5] C. Simon et al, RPC test with heavy-ion beams, this Report

* Work supported by BMBF 06HD7141I and EU/FP7 HadronPhysics3

† deppner@physi.uni-heidelberg.de

Implementation and Test of a Configuration Upset Mitigation Strategy for the CBM ToF ROB FPGA without a local Memory Storage *

A. Oancea[1], *C. Stüllein*[1], *J. Gebelein*[1], *S. Manz*[1], *and U. Kebschull*[1]

[1]Infrastructure and Computer Systems for Data Processing (IRI), Goethe-Universität, Frankfurt, Germany

Motivation

The Read-Out Board (ROB) for the CBM ToF read-out chain is the connection between the front-end electronics (FEE) and data acquisition (DAQ) and processing further upsream. As such, unlike the rest of the devices in the DAQ chain, it is situated fairly close to the FEE, and therefore exposed to radiation. A local intelligence is necessary in the ROB for simple data pre-filtering and compression, and therefore it will feature an FPGA, whose radiation-caused configuration memory upsets need to be mitigated. So far, mitigation approaches always included a local memory storing the golden copy of the configuration memory, e.g. a local flash memory in the SysCore v.2.x and SysCore v3.x [1,2]. Since Flash technology has a considerably low Total Ionizing Dose (TID), a new apporach without a local memory present has been developed for the ROB.

Approach

The developed approach uses the Soft Error Mitigation Xilinx IP Core (SEM Controller), which is capable to autonomously detect and correct Single-Bit Upsets (SBUs), and report on Multiple-Bit Upsets (MBUs) (Figure 1).If a configuration frame has two upsets, the affected frame is reported via serial connection to a configuration management entity that can be on another level of the DAQ chain. From there, the affected frame can be dynamically overwritten via JTAG without the need to reset the FPGA. A reset is only necessary when more than two upsets occur in the same frame, since the SEM Controller cannot identify the location of the upsets anymore. The decision to use the GBTx has made it possible to have remote JTAG and GPIO connections to the FPGA through the GBT-SCA, and therefore a local copy of the configuration memory is no longer required.

An AC701 development board is currently running the SEM controller, while the configuration entity is running on a PC, that also monitors events.

Results

The setup has been tested in two beam times at COSY, Juelich in August 2014 and December 2014 respectively. An overview of the event distribution can be seen in Figure 2. For the low rate event distribution, which is closer to real event rates in the final setup, it would take roughly 10 min to a SBU, and 71 min to an MBU. A full reprogram was needed every 14 hours.

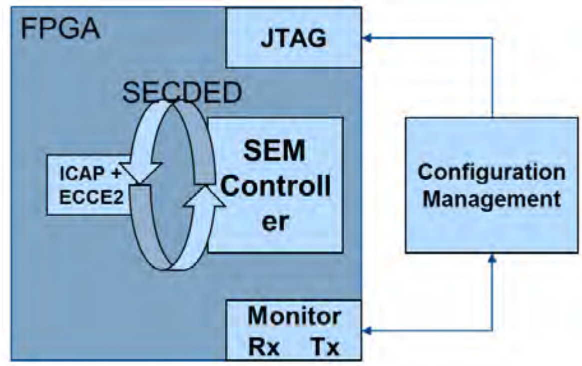

Figure 1: Conceptual overview of the mitigation apporach. The SEM Controller is capable of correcting single frame upsets and reporting dobule frame upsets (SECDED), as well as reporting a need for a complete reset in case of multiple upsets per frame.

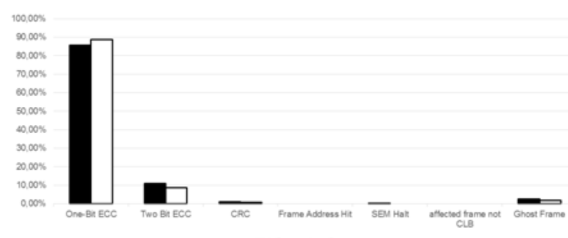

Figure 2: Distribution of different error types for high (2.5E7 protons/second) and low (4.2E6 protons/second) rates. Roughly 90% of all events are SBUs and do not require intervention from outside. Most other errors (8%) are two-bit upsets and handled by the configuration management entity. In rare cases, a full reset was required (CRC).

References

[1] A. Oancea, J. Gebelein, S. Manz, U. Kebschull, Firmware Development for the SysCore v3.1 Configuration Controller, CBM Progress Report 2013, p. 89

[2] J. Gebelein, G. May, and U. Kebschull, SysCore v3.1 – A universal Read Out Controller and Data Processing Board, CBM Progress Report 2013, p. 88

* Work supported by HGS-HIRe

Cosmic-ray and in-beam tests of 100 Ohm transmission line MGMSRPC prototype developed for the inner zone of CBM-TOF *

M. Petriş[1], *V. Aprodu*[1], *D. Bartoş*[1], *A. Bercuci*[1], *G. Caragheorgheopol*[1], *F. Constantin*[1], *V. Duţă*[1], *M. Petrovici*[1], *L. Prodan*[1], *A. Radu*[1], *L. Rădulescu*[1], *and V. Simion*[1]

[1]NIPNE, Bucharest, Romania

As a solution for the high granularity required for the most inner zones of the CBM-TOF, a new MGMSRPC prototype (called RPC2013), was designed and built. Constructive details of the tested prototype are presented in [1]. The strip structure of the readout and high voltage electrodes, (4.19 mm strip pitch with 2.16 mm width and 200 mm strip length) was decided based on APLAC simulations. The aim was to obtain a differential readout impedance as close as possible to 100 Ω in order to match the input impedance of the front-end electronics. The prototype is based on low resistivity ($\sim 10^{10}$ Ω·cm) glass plates in order to cope with the high values of the counting rate anticipated for the inner zone of the CBM-TOF wall. High counting rate tests performed with MGMSRPCs using low resistivity glass electrodes were already reported [2, 3].

The response of the new prototype was first tested with cosmic rays and radioactive sources in the detector laboratory of Hadron Physics Department from IFIN-HH. The prototype was operated at 2 x 5.5 kV high voltage with 95%$C_2F_4H_2$ + 5%SF_6 gas mixture. For this measurements the strip signals were processed by fast amplifiers/discriminators NINO chips [4], their differential output being converted by CAEN V1290A TDCs.

Figure 1: Cosmic ray experimental set-up.

The experimental setup used in the cosmic ray test is presented in Fig. 1. The position along the strips, triggered by the plastic scintillators positioned above the detector across the strips, is presented in the left side of Fig. 2 as a function of strip number. The right part of Fig. 2 shows the correlation between the position along the strip and position along the 10 cm length plastic scintillator, readout at both ends.

The in-beam tests of this prototype were performed in an in-beam test campaign of CBM-TOF Collaboration in October 2014 at GSI Darmstadt and at CERN-PS accelerator in November 2014, in an in-beam test campaign of different subsystems of CBM Collaboration. In the CERN in-beam

* Work supported by EU-FP7/HP3 Grant No 283286 and Romanian NASR/CAPACITATI-Modul III contract RO-FAIR F02 and NASR/NUCLEU Project PN09370103

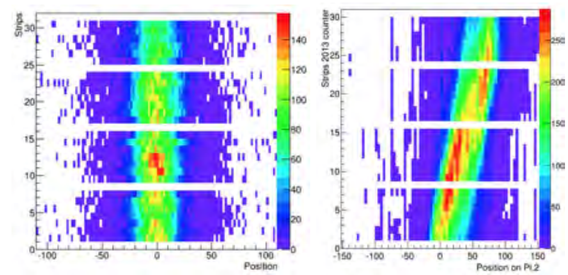

Figure 2: Cosmic-ray test: left side - position along the strip as a function of strip number; right side - correlation between position along the strips and position in the platic scintillator.

test the MGMSRPC signals were processed by the same electronic chain as in the cosmic ray test. As reference for time resolution estimation was used a plastic scintilator readout at both ends. Preliminary results show a time resolution of 52 ps using pure $C_2F_4H_2$ and of 61 ps using a gas mixture of 95%$C_2F_4H_2$ + 5%SF_6, after performing walk corrections and subtraction of the contribution of the reference counter. The October 2014 in-beam test was focused

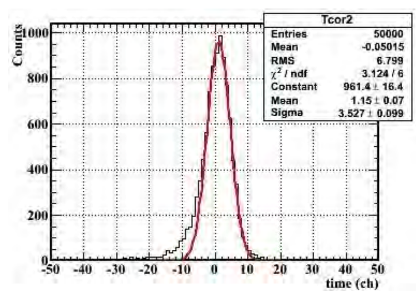

Figure 3: CERN in-beam test time spectrum using a gas mixture of 95%$C_2F_4H_2$ + 5%SF_6.

on the compatibility with the PADI8 new FEE, aiming to be used in the CBM-TOF wall. The MGMSRPC signals were converted by FPGA TDCs [5]. Data analysis is in progress.

References

[1] V. Aprodu et al., CBM Progress Report 2013, p.79

[2] M. Petrovici et al., JINST 7 (2012) P11003

[3] A. Bălăceanu et al., CBM Progress Report 2013, p. 78

[4] F. Anghinolfi et al., Nucl.Instr.and Meth. A533(2004)183

[5] J. Frühauf et al. CBM Progress Report 2012, p.71

Projectile Spectator Detector

Radiation hardness of the PSD APDs for the CBM experiment*

V. Kushpil[1], *A. Kugler*[1], *S. Kushpil*[1], *V. Mikhaylov*[†1,2], *O. Svoboda*[1], *and P. Tlusty*[1]
[1]NPI of ASCR, Řež, Czech Republic; [2]CTU, Prague, Czech Republic

Projectile Spectator Detector (PSD) of the CBM experiment is designed to register forward spectator nucleons and fragments emitted in nucleus-nucleus collisions at very low polar angles. It will be used to determine the collision centrality and the reaction plane orientation.

The PSD is a fully compensating modular lead-scintillator calorimeter. The Avalanche Photo-Diodes (APD) are used to read out the scintillation light via wavelength shifting fibers. An important characteristic of the APD is its radiation hardness to a neutron fluxes of 10^{13} n/cm^2 which corresponds to two months of CBM experiment operation.

Two different APD samples, Ketek PM3375 and Zecotek MAPD-3N, were irradiated at the NPI Řež Cyclotron Facility by quasi-monoenergetic secondary neutron beam with energy of 35 MeV. A sample of Zecotek APD was irradiated with a dose of $3.4\pm0.2\ 10^{12}$ n/cm^2, while two samples of Ketek APDs were irradiated with $2.5 \pm 0.2\ 10^{12}$ n/cm^2. Doses were measured with a special PIN diode calibrated with a dose equivalent to 1 MeV neutron [1]. The operation temperature during the tests was kept at $22 \pm 0.5°$ C.

The APD characteristics were measured before and after the irradiation. The Capacitance-Voltage (C-V), Current-Voltage (I-V), and Capacitance-Frequency (C-F) characteristics were studied using dedicated testing setup at NPI Řež [2,3]. After irradiation, the C-V technique showed significant decrease of hysteresis and fast but not complete self-annealing. The I-V curve revealed about 1000 times increase of dark current after irradiation. The C-F study showed significant increase of short-living traps in Silicon. The test results suggest an increase of internal APD noise, especially of the high frequency, which dependents on the amount of short-living traps in the APD volume.

Figures 1 (2) show the results of the Ketek (Zecotek) APD tests with LED and cosmic muons. Both APDs have a maximum signal (noise) amplitude of about $0.3 - 0.4$ V (0.05 V) which corresponds to $20 - 30$ ph.e (3 ph.e). After irradiation both APDs are unable to resolve single photons due to high noise levels. This is not critical for the PSD performance since there are at least 15 ph.e. produced in one PSD module already by a cosmic muon. The signal and noise peaks for irradiated Ketek APD are very close which makes it very difficult to separate signal from noise. On a contrary, signal and noise peaks for Zecotek APDs are well separated from each other, what allows reliable signal from noise separation even after irradiation.

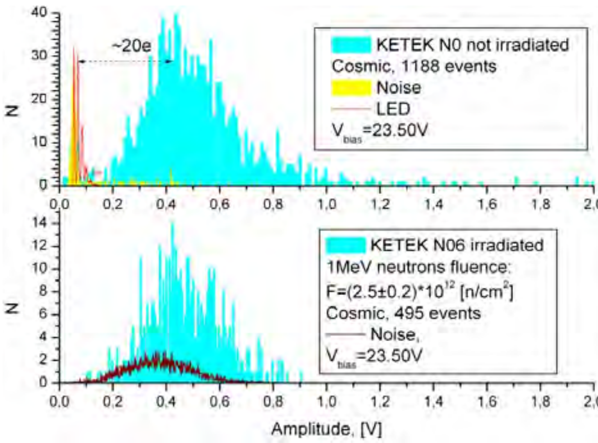

Figure 1: Test results with LED and cosmic muons of Ketek APD before (upper) and after (lower) irradiation.

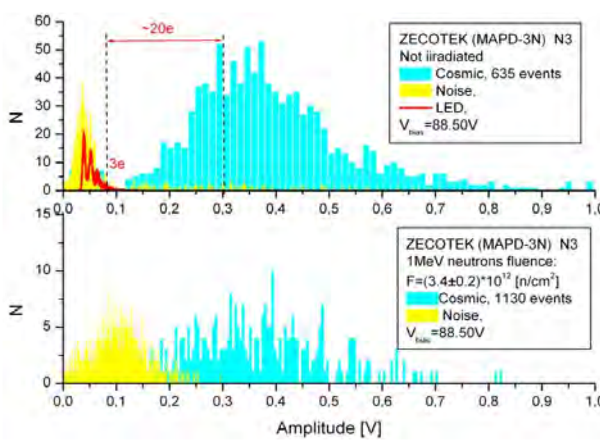

Figure 2: Test results with LED and cosmic muons of Zecotek APD before (upper) and after (lower) irradiation.

References

[1] V. Kushpil, S. Kushpil and Z. Huna, EPJ Web of Conferences 24 (2012) 07008.

[2] V. Kushpil, V. Mikhaylov, S. Kushpil, P. Tlusty, O. Svoboda, A. Kugler, doi:10.1016/j.nima.2014.11.071

[3] V. Kushpil, S. Kushpil, JINST 7 (2012) C01084.

* Work supported by the European Community FP7 – Capacities, contract HadronPhysics3 n°283286, LG12007 of the MECR and M100481202 of the ASCR grants, by project MSMT LG14004 of Cooperation Program between JINR and NPI in 2013-2014.

† mikhaylov@ujf.cas.cz

DAQ and Online Event Selection

High-Level Dataflow Description of FPGA Firmware Components for Online Data Preprocessing*

H. Engel[1] *and U. Kebschull*[1]

[1]IRI, Institut für Informatik, Johann Wolfgang Goethe-Universität Frankfurt, Frankfurt, Germany

FPGA firmware is commonly described with low level hardware description languages like VHDL or Verilog. With FPGAs getting bigger and faster, they become more and more suitable to also perform complex data processing algorithms. Describing complex algorithms with VHDL or Verilog creates code that is hard to maintain and makes it almost impossible to exploit the full capabilities of recent FPGAs. Frameworks are available that allow to describe hardware algorithms on a dataflow level. An existing cluster finding algorithm was ported from VHDL to dataflow description, compared against the original VHDL implementation and tested in hardware.

High energy physics detector readout chains rely widely on Field Programmable Gate Arrays (FPGAs) due to their flexibility and processing capabilities. The functional description of these FPGAs is usually realized with hardware description languages like VHDL or Verilog. These languages give fine control over the low level logic blocks inside the FPGAs like Lookup-Tables and Flip-Flops. The number of logic resources available in FPGAs has increased significantly over the last years and the growth is expected to continue.

The algorithm investigated in this work is the FastClusterFinder [1] that was used in the High-Level-Trigger Read-Out Receiver Card at ALICE in the read-out of the Time Projection Chamber during LHC Run1. This algorithm was implemented in plain VHDL and was developed during a PhD thesis. The VHDL implementation is a rather complex design due to its flow control structures and the number of fixed point and floating point arithmetics. Comparing the size of this implementation with the number of resources available in the most recent generations of FPGAs makes it obvious that the possibilities of new devices cannot be exploited effectively with low level hardware description languages.

The same algorithm was re-implemented in a dataflow description language from Maxeler Technologies [2]. This language uses a Java dialect to describe hardware on an algorithmic level. The compiler resolves the description into a dataflow graph, adjusts latencies, handles data transport, creates vendor specific IP cores and translates the description back into VHDL. The resulting files are then run through the regular vendor tools to create an FPGA configuration file.

The FPGA resource usage of the VHDL and the dataflow implementations are in the same order of magnitude as shown in table 1. The dataflow language allows to control the amount of pipelining to be used for the individual processing steps by specifying a pipelining factor. Column *Dataflow 1* shows the results with a pipelining factor of 0.5, which leads to a timing performance equivalent to the original VHDL implementation. Column *Dataflow 2* uses the maximum pipelining factor of 1.0 and creates a design that can be run at higher clock frequencies. The difference in BRAMs results mainly from a different implementation of the fixed-to-float conversion. The code base is the same for both pipelining settings and is significantly smaller and much easier to maintain than the VHDL implementation. Trying out different pipelining levels in VHDL could easily take several weeks alone.

Resource Usage	VHDL	Dataflow 1	Dataflow 2
Flip-Flops	∼5200	∼4800	∼6000
Lookup Tables	∼4600	∼4900	∼5100
BRAMs	19	19	21
DSPs	8	8	8

Table 1: FPGA Resource usage comparison of VHDL and two dataflow implementations

The dataflow implementation was tested in a Max3 Dataflow Engine containing a Virtex-6 FPGA and using the data transport framework provided by Maxeler. Event data is written into the FPGA with the Maxeler software API and the processed results are read back in the same way. The output of the algorithm was compared to that of the VHDL implementation using simulated and real detector data from LHC Run1.

A single instance of the cluster finder implementation from the dataflow description could also be extracted from the dataflow framework and ported to the C-RORC [3], which is used for the read-out of detector data in ALICE and ATLAS for LHC Run2. This allows to create netlists from dataflow implementations and integrate these cores into existing firmware environments. A deeper investigation on the performance of this integration is ongoing.

References

[1] T. Alt and V. Lindenstruth, *Status of the HLT-RORC and the Fast Cluster Finder*, GSI Scientific Report 2009

[2] Maxeler Technologies, *Programming MPC Systems*, White Paper, June 2013

[3] ALICE and ATLAS Collaborations, *The C-RORC PCIe Card and its Application in the ALICE and ATLAS Experiments*, JINST Vol 10, N2, C02022, 2015

* Work supported by HGS-HIRe, HIC4FAIR

A Feature Extraction Framework for Automatic FPGA Firmware Generation *

C. García Chávez[1] *and U. Kebschull*[1]

[1]Infrastructure and Computer Systems for Data Processing (IRI), Frankfurt University, Frankfurt/Main, Germany

Introduction

The design and development of a FPGA real-time data processing platform (or also known as online data processing platform) is a common task in every high-energy particle physics experiment. In most cases, it is a time consuming task that might take up to a couple of years to be developed, not mentioning that expert knowledge about hardware and software architecture and design is required. Despite the fact that most of the used algorithms in online data processing are very well known (from a physical and mathematical analysis), for different hardware platforms and data structures specific implementation of those algorithms is required. In order to overcome those common problems, a framework for automatic firmware generation has been developed, allowing the implementation of common algorithms for feature extraction. A brief overview of the framework as well as its experimental application in the Online Feature Extraction of the CBM Transition Radiation Detector (TRD) experiment will be presented.

Feature Extraction Framework Overview

Real-time processing algorithms require the extraction of specific information from a set of time-based signals. In other words, feature extraction algorithms are developed to extract relevant sets of data and, on the other hand, discard data that does not provide useful information for later reconstruction and/or analysis algorithms. The feature extraction framework is presented as a graphical user interface, where a user is able to configure a FPGA hardware platform based purely on its feature extraction parameters. Common used processing algorithms such as peak-finding, center of gravity calculation, time over threshold and cluster finding are implemented as processing cores inside the framework. In order to provide an agnostic-data processing, specific interface-cores are included to convert from specific data containers into known data containers used by the framework. As presented before in [1], the AMBA AXI4-Stream interface protocol[2] has been implemented as default internal communication interface for every design generated by the framework. As consequence, one of its main features is to allow new front-end electronics and communication protocols to be included into the framework by means of interface-cores. After configuring the desired feature extraction parameters, front-end electronics type and the requested communication protocols are set, an automatic compilation process is started where first, a project folder structure is created where source files written in human-readable VHDL are automatically generated and then, a synthesis process managed by external tools provided by Xilinx [3] is performed. Finally, configuration files (e.g. bitfile for FPGA configuration) are generated under the project hierarchy.

Current Status

The performance of the presented feature extraction framework is currently being tested in the CBM Transition Radiation Detector (TRD). The processing algorithms used for feature extraction were previously tested during a beam test as mentioned in [4][5]. Current results show that there is no significant FPGA resource consumption difference between hand-written code versus automatic-generated code, however a significant improvement on design-time has been achieved when using the presented framework for automatic firmware generation.

References

[1] C. García Chávez, “The Feature Extraction Framework”, FLESDAQ Session, 24th CBM Collaboration Meeting

[2] Xilinx Inc, “AMBA AXI4 Interface Protocol”, http://www.xilinx.com

[3] Xilinx Inc, “ISE Design Suite”, http://www.xilinx.com

[4] C. García Chávez and U. Kebschull, “Development of an online feature extraction pre-processing stage for TRD based on SPADIC 1.0”, CBM Progress Report 2013

[5] C. Bergmann et al, “Common CBM beam test of the RICH, TRD and TOF subsystems at the CERN PS T9 beam line in 2014”, GSI Scientific Report 2014

* Work supported by BMBF No. 05P12RFFCM.

Evaluation of FRAM for use in Radiation Environments*

J. Gebelein[1], *C. Stüllein*[1], *and U. Kebschull*[1]
[1]Infrastructure and Computer Systems for Data Processing (IRI), Frankfurt University, Frankfurt/Main, Germany

Ferroelectric Random Access Memory (FRAM) is a non-volatile, low power memory with high read/write speed and high endurance. It stores bit information in semi-permanent electric dipoles formed within a dielectric crystal cell by reversible spontaneous electrical polarization [1]. Each storage cell is composed of either two transistors and two capacitors (2T2C) as shown in Figure 1, or one transistor and one capacitor (1T1C). The MOSFET is built in a conventional CMOS process, while the capacitor typically uses ferroelectric PZT ($Pb(Zr,Ti)O_3$) material. PZT can easily be added to a conventional CMOS process by insertion of two mask layers between substrate contact and metal layers [1].

Specification	FRAM	Flash	SRAM
read time	110 ns	<120 ns	1 ns
write time	180 ns	1s/sector	<1 ns
standby curr.	5 μA	5 μA	7 μA
r/w current	4 mA	12-24 mA	40 mA
single bit r/w	yes	no	yes
endurance	10^8-10^{12}	100.000	∞

Table 1: Comparison of FRAM, Flash and SRAM.

Since the FRAM's ferroelectric storage cells are promoted to be unsusceptible against magnetic fields as well as radiation, FRAM is a prominent candidate to replace current technologies in particle accelerators – a comparison is given in Table 1. But the surrounding CMOS transistors were expected to behave differently. To verify this assumption, a beamtest has been performed at COSY Jülich in 08/2014, using 2 GeV/u p^+ particles and a total flux of $6 \cdot 10^8 p^+/s$. Two COTS FRAM chips placed on development boards have been selected for irradiation: Fujitsu MB85RS256B FRAM chip on mikroElektronika MIKROE-1486 break-out board (32 KB plain FRAM array) as well as Texas Instruments MSP430FR5739 FRAM chip on MSP-EXP430FR5739 Experimenter Board (16 MHz 16-Bit RISC Microcontroller with 16 KB FRAM storage). Two boards of each type were irradiated in parallel. The first ones were powered and readout continuously in beam while the second ones were hold completely passive and unpowered. All chips were initialized with a logical 0/1 pattern.

Throughout the beamtest, no upset could be detected in the Fujitsu devices, neither in active read-back mode, nor in passive mode at the end. Unfortunately, the constantly powered device broke down due to a leakage failure after about 160 krad. Current drain raised gradually from an initial operation value of 0.0007 A up to a final value of 0.100 A. After an unpowered annealing period of multiple hours at room temperature, the device was fully functional again and the stored FRAM configuration was still unchanged.

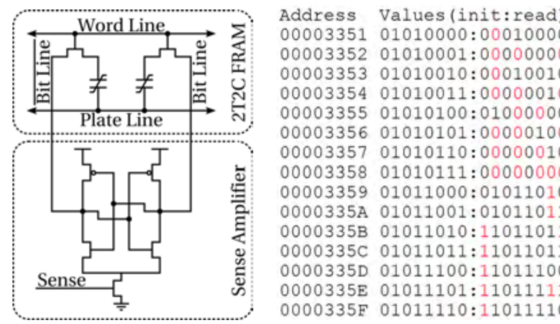

Figure 1: Left: FRAM 2T2C cell circuit according to [2]; Right: MSP430FR5739 bit errors during read-back.

While the passively irradiated Texas Instruments FRAM chip has shown no errors, the actively operated one observed a single failure throughout the test. It lead to an upset of multiple stored bit values in a single continuous chain as depicted in Figure 1. All values remained statically stored within the FRAM cell. A possible causer is the utilized sense amplifier (AMP). Sense AMPs in CMOS are usually realized as 4-transistor latch-type circuits as depicted in Figure 1. In consequence, a Single Event Transient (SET) in the AMP transistor's cross-coupled inverters whose pulse width overlaps with the sensing interval can lead to incorrect cell *read* results. Reading an FRAM cell is a destructive process – every cell *read* results in a subsequent cell *write*. This may have caused the SET's *latching* into a permanent Single Event Upset (SEU), even in the radiation tolerant FRAM cells. The characteristic structure of the observed upsets furthermore clearly allows to draw conclusions about the internal memory structure: AMPs are arranged in parallel to the memory rows which enables their reuse across the memory columns. If a single AMP is upset, a single bit position within multiple words is affected.

References

[1] V. C. Kumar, B. Underdahl, "Texas Instruments FRAM MCUs for Dummies", John Wiley & Sons, Inc., Hoboken, New Jersey, 2012, ISBN 978-1-118-15983-5

[2] Fujitsu Semiconductor, "Application Note AN-21377 about: FRAM MCU Key Strengths and Applications", 2012

* Work supported by BMBF (05P12RFFCM)

CBM First-level Event Selector Data Management Developments*

H. Hartmann[1], *J. de Cuveland*[1], *and V. Lindenstruth*[1]

[1]FIAS Frankfurt Institute for Advanced Studies, Goethe-Universität Frankfurt am Main, Germany

Figure 1: upgraded FLES demonstrator system.

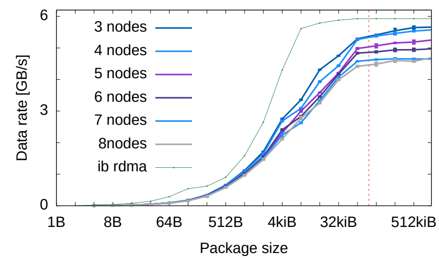

Figure 2: MPI benchmark on the Micro-FLES.

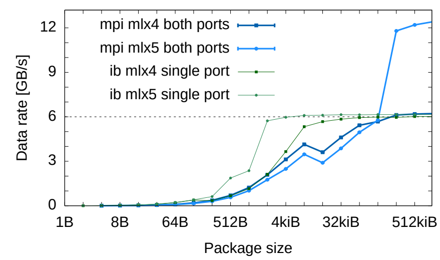

Figure 3: Perfomance tests for the Micro-FLES2.

The First-level Event Selector (FLES) is a high performance computing cluster functioning as the central event selection system in the CBM experiment. It combines data from a large number of input links to time intervals and distributes them to the compute nodes, via a high-performance network. Simultaneously, the FLES carries out online analyses and complete event reconstruction on the data. Data rates at this point are expected to exceed 1 TByte/s.

The FLES system will consist on one hand of a scalable supercomputer with custom FPGA-based input interface cards and a fast event-building network and will be constructed largely from standard components. On the other hand special developed software allowing to process the incoming data in real-time builds up the FLES.

A small scale, highly customizable platform, the Micro-FLES cluster was installed at GSI. Eight identical compute nodes provide a total of 192 logic cores and 512 GB memory plus one head node for infrastructural services. This test system enables studies on the development of the FLES such as elaborating performant software for timeslice building.

A *timeslice* is the fundamental data structure managing access to all detector raw data of a given time interval. In addition to existing timeslice building prototype software based on InfiniBand Verbs investigations of a more high-level interface to the network hardware have been performed using MPI. For this purpose a specialized micro benchmark test suite was developed simulating the FLES timeslice building use case. Benchmark results for simultaneous data transfer on the Micro-FLES are displayed in Fig 2. When communication is established only between three nodes, MPI's performance compares to the maximum data rate of point to point communication for Infiniband Verbs (green curve) on the Infiniband-FDR network. However, the data rate decreases by 15% when all eight nodes of the Micro-Fles are participating in an any-to-any communication. Further tests on bigger compute cluster are neccessary to evaluate the achievable data rates for MPI on a big scale and are currently under investigation.

* Work supported by BMBF (05P12RFFCP) and HIC for FAIR

In 2014 the FLES demonstrator system was upgraded signifciantly to the Micro-FLES2. First, the Micro-FLES2 was equipped with the latest Mellanox dual ConnectX-IB HCAs (mlx5), in addition to the existing Mellanox dual ConnectX-3 cards (mlx4). Overall the new cards are faster than the old as shown in Fig. 3. A data rate of 6 GB/s can be achieved using only one of the four ports, already. Furthermore, the new cards feature a 16x PCIe 3.0 interface and therefore allow to saturize the full bandwith of both ports. An accumulated data rate of 18 GB/s can be achieved utilizing all Infiniband ports. With this first upgrade the Micro-FLES2 can send data from node to node three times as fast as before (e.g., 18 GB/s instead of 6GB/s). The improved performance is essential for the development of timesslice building software.

Secondly, two further Mellanox SX6036 36-port 56Gb/s switches were installed in order to realize different network setups such as a fat tree. This helps investigating routing issues in the development of software when distributing the incoming data. The previous existing switch was connected with full bidirectional bandwidth to both of the new switches making them leaves of a fat tree. All first ports of mlx4 and mlx5 for each node were connected to leaf-switch1 and all second ports to leaf-switch2. Using this setup the network structure and blocking ratio in case of a fat tree can be configured dynamically via the provided internet interface of the switches. The upgraded Micro-FLES2 provides better performance and a greater flexibilty in testing different scenarios allowing to evaluate a greater varity of possibilites for the final system – the FLES.

CBM FLES Input Interface Developments*

D. Hutter[1], *J. de Cuveland*[1], *and V. Lindenstruth*[1]
[1]FIAS Frankfurt Institute for Advanced Studies, Goethe-Universität Frankfurt am Main, Germany

The First-level Event Selector (FLES) is the central event selection system in the CBM experiment. Its task is to select data for storage based on online analyses including a complete event reconstruction. To do so, the FLES timeslice building has to combine data from all input links to time intervals and distribute them to the compute nodes. To allow for efficient timeslice building, detector data streams are partitioned into microslices prior to combining them. Microslices are specialized containers covering a constant timeframe of real time, which is the same for all subsystems. This allows data agnostic, subsystem independent timeslice building. This partitioning will be done by the Data Processing Boards (DPB) as they are the last stage of the read-out tree which has to contain subsystem specific components.

The FLES input interface is realized by a custom FPGA PCIe card, the FLES Interface Board (FLIB). Its purpose is to provides the optical interface to the DPBs as well as the interface to the FLES input nodes. The current development is based on the commercial HTG-K7-PCIE board form Hitech Global. It features a Xilinx Kintex-7 FPGA, a 8x PCIe 2.0 interface, up to eight 10 GBit/s links and optionally 8 GB of DDR3 memory.

The FPGA design includes the protocol for receiving microslices, a pre-processing engine preparing microslices for timeslice building and a custom full off-load DMA engine. Once configured the DMA engine is capable of constantly transferring microslices and meta data to the PCs memory without involving the host CPU. The only task the CPU needs to perform is to acknowledge processed data segments occasionally to allow reusing buffer space. A measurement of the DMA performance for one to four 10 Gbit/s microslice streams is given in Fig. 1. For up to three steams, data is transmitted at full input speed. For four streams, the input data rate exceeds the available PCIe bandwidth. The achieved maximum data rate is 3345 MB/s, which matches the absolute maximum PCIe data rate for the given configuration.

For demonstration and testing the input interface concept in real live applications, the FLIB and flesnet software have been used for read-out in the CERN-PS 2014 testbeam at T9 beamline. In contrast to the final system, current setups lack the DPB layer and do not support the creation of microslices. A specialized FLIB prototype firmware therefore includes a mockup of the DPB design and is capable of directly receiving CBMNet messages as delivered by the CBM front-end electronics. Simplified microslices are generated inside the FLIB and subsequently handled in the same way as foreseen for the final setup. Thus the setup is capable of delivering fully build timeslices to any given consumer. In case of the testbeam, timeslices were written to disk and simultaneously published via a ZMQ socket to CBMroot clients for front-end calibration and online monitoring. In addition the firmware and software includes support for front-end configuration and synchronization over CBMnet which is accessible via a ZMQ interface or from within CBMroot.

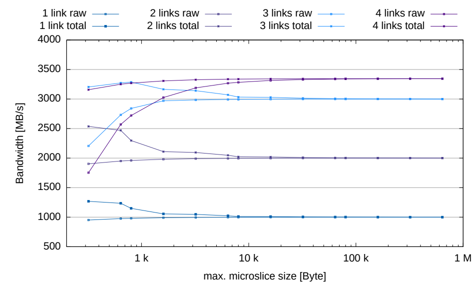

Figure 1: FLIB read-out bandwidth

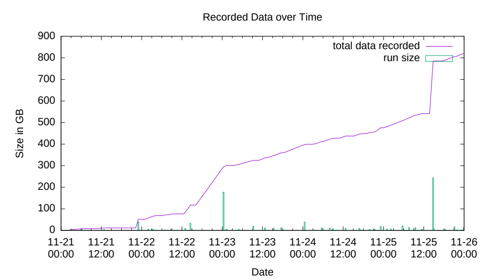

Figure 2: Recorded testbeam data over time

During the testbeam a single FLIB in conjunction with the flesnet software was successfully used to read-out up to six detector setups in different configurations. Three different flavors of data sources have been employed, Syscore 2, Syscore 3 and TRB boards. Figure 2 shows an overview over five days of data taking. In total 888 GB of data in 84 runs was written to disk without any major read-out related problems. Online performed data consistency checks and first offline analysis did not reveal any issues with the data.

To support future setups including DPBs the FLES interface module is currently under development. It will provide a 10 GBit/s link transferring microslices to the FLIB enabling full featured microslice creation on the DPBs.

* Work supported by BMBF (05P12RFFCP) and HIC for FAIR

CBM Control System Board with TMS570 Micro-controller

J. A. Lucio Martínez[1] *and U. Kebschull*[1]
[1]Infrastructure and Computer Systems for Data Processing (IRI), Frankfurt University, Frankfurt/Main, Germany

The Control System

A control system board is being designed to be used as an EPICS IOC (Input Output Controller) for the CBM experiment.

EPICS

EPICS is an Experimental Physics and Industrial Control System. It is a server based system that performs real world operations. Each server is called IOC [1]. A basic IOC was compiled successfully for the TMS570 on RTEMS but no setups were tested yet. To test the software before building the Control System Board, the TMS570 Hardware Development Kit (HDK) depicted in Figure 1 is currently being used.

Figure 1: TMS570 HDK Board

The Micro-controller: TMS570

The selected micro-controller is the cheap TMS570LS series for automotive safety critical applications. This micro-controller implements ECC on SRAM and flash, although the latter will not be used due to radiation susceptibilities in the final setup. The micro-controller posses Interfaces capabilities such as Flex Ray, CAN, LIN and further communication interfaces [2]. The disadvantages of this micro- controller are: The manufacturer designed it to be programed with specialised TI software and in order to compile the code for this microprocessor TI tools are necessary. Fortunately, there are open source solutions as well.

RTEMS for TMS570

The system will operate with the RTEMS Operating System as it supports EPICS applications, has a free open source license and has real time OS capabilities [3]. The RTEMS BSP (Board Support Package) for TMS570 is still being developed. Fortunately, the last version works and the tests applications run successfully as shown in Figure 2. The TMS570 BSP developers used OpenOCD to program the micro- controller with a SDRAM initialising code and bootstrap it by writing the RTEMS executable binary in the SDRAM [4]. This is how only open source software is used in the programming chain.

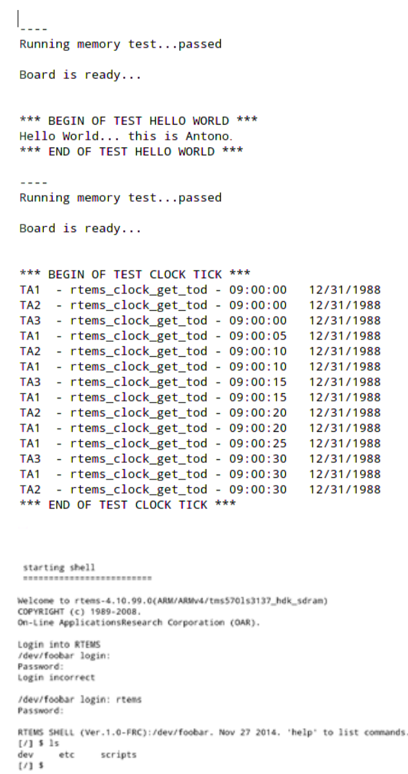

Figure 2: RTEMS Running on TMS570 HDK

References

[1] Argone National Laboratory, ”About EPICS”, http://www.aps.anl.gov/epics/about.php

[2] Texas Instruments, ”TMS570 Data sheet”, http://www.ti.com/lit/ds/symlink/tms570ls20216.pdf

[3] On-Line Applications Research Corporation (OAR), ”RTEMS C User”s Guide”, https://docs.rtems.org/doc-current/share/rtems/pdf/c_user.pdf

[4] RTEMS Database, ”TMS570 RTEMS BSP”,October 2014, https://devel.rtems.org/wiki/TBR/BSP/Tms570

Maintenance of read-out controller firmwares for GET4 and NXYTER chips *

S. Manz[1] *and U. Kebschull*[1]

[1]Infrastruktur und Rechnersysteme in der Informationsverarbeitung (IRI), Frankfurt University, Frankfurt, Germany

Introduction

The read-out controller firmwares for the nXYTER and GET4 chips required some substantial adaptions to keep up with the overall progress of CBM DAQ developments in 2014. In case of the read-out controller for the GET4 chips, the following points needed to be addressed:

- Backport of firmware with CBMNet v2 [1] to the SysCore v2 board
- Putting into service the SysCore v3 [2] firmware for the new GET4 prototypes (GET4 v1.23 [3])
- Implement netlist based build-flow for GET4 module, Auxiliary module and USB module
- Update CBMNet from v2 to v3 for all involved GET4 firmwares (SysCore v2 and v3)

In case of the read-out controller for the nXYTER chips, the following actions had to be taken:

- Provide SysCore v2 firmware with CBMNet v2
- Update CBMNet from v2 to v3 for nXYTER firmwares

Read-Out firmware for GET4 chips

Backport of firmware for SysCore v2 boards A read-out firmware for the GET4 v1.23 chips that can be connected to a CBMNet v2 network was only available for the SysCore v3 board. As there was no GET4 v1.23 adapter hardware for the SysCore v3 available at the beginning of the year, the read-out based on legacy SysCore v2 hardware was desired. This was achieved by porting the existing SysCore v3 firmware back to the SysCore v2 board.

SysCore v3 firmware to read-out the GET4 v1.23 When the new GET4 v1.23 hardware for the SysCore v3 became available in autumn, the firmware had to be put into service. It now runs stably with this new hardware and is planned to be used in the next ToF beamtime at CERN end of February 2015.

Netlist based build-flow For better compatibility with the CBM build server [4], the build flow of the GET4 related firmwares was improved to first build netlists for each module that then can be put together to a full firmware. This allows a better and cleaner distribution of responsibilities among the developers of the different modules. The modules that have been adapted are: the module to interface GET4 chips, the module with basic functionality (Auxiliary module), and the module to transport data via USB. One external module that implemented a comparable netlist build flow is used as well, the CBMNet transport module.

Update CBMNet to version 3 During preparation for autumn beamtimes, CBMNet was updated from v2 to v3. This update was also integrated into the read-out controller firmwares for the GET4 chips.

Read-Out firmware for nXYTER chips

Provide CBMNet version 2 firmware The read-out controller firmware for the nXYTER chip was only available for CBMNet v1 so far, while read-out for the STS-XYTER and the SPADIC chips relied on CBMNet v2. For 2014 beamtimes it was foreseen to use the nXYTER chip in the same setup as STS-XYTERs and SPADICs. The nXYTER was planned as a reference system and also to read-out the fiber hodoscopes. As a downgrade of STS-XYTER and SPADIC setup to CBMNet v1 was not possible, the nXYTER read-out had to be updated to CBMNet v2.

Update CBMNet to version 3 The read-out controller firmware for the nXYTER chips needed the same update as the above-mentioned update to CBMNet v3 in case of GET4 read-out.

References

[1] F. Lemke, S. Schatral, and U. Brüning, "Status of the CBM-net based FEE DAQ readout", CBM Progress Report 2013, Darmstadt 2014, p.86

[2] J. Gebelein, D. Gottschalk, G. May, and U. Kebschull, "SysCore3 - A universal Read Out Controller and Data Processing Board", GSI Scientific Report 2012, Darmstadt 2013, p.74

[3] H. Flemming, and H. Deppe, "The GSI Event Driven TDC ASIC GET4 V1.23", GSI Scientific Report 2013, Darmstadt 2014, p.382

[4] J. de Cuveland, and V. Lindenstruth, "Status of DAQ/FLES firmware build server", 23rd CBM Collaboration Meeting, Darmstadt, April 2014

* Work supported by BMBF No. 06HD9123I.

A CBMNet Bridge for the TRB3 *

M. Penschuck[1], *J. Michel*[1], *J. Stroth*[1,2], *and the TRB3 collaboration*[1]
[1]Goethe-Universität, Frankfurt, Germany; [2]GSI, Darmstadt, Germany

The TRB3 is a flexible and modular FPGA-based data acquisition platform originating from the HADES detector at GSI. Unifying all base-functionality on a universal main board, connectivity to the experimental setup is established using up to five application-specific add-on boards. The platform is used by a number of detectors, amongst them prototypes for CBM-MVD and CBM-RICH.

The board features five inexpensive Lattice ECP3 FPGAs optimised for a high IO count rather than computational power, which is typically not required for early DAQ stages: one central chip primarily executes management- and network-related tasks while the remaining FPGAs together with their respective add-ons form four independent sub-systems. Applications include FPGA-based TDC- (up to 264 channels/board with a precision of 7.2 ps RMS [1]) and ADC-measurements as well as the read-out of high-speed digital signals, e.g. for the MAPS in case of CBM-MVD. The TRB3 can be operated in a stand-alone fashion only requiring an external power supply and a PC capable of Gigabit Ethernet (GbE); however, large systems are inherently supported by its internal network protocol, TrbNet, which was originally developed for HADES.

In order to bring forward the integration of TRB3-based experiments into the CBM DAQ, uplink- and synchronisation capabilities have been added to the platform. As most TRB3 applications are intricately build around the TrbNet infrastructure, it was decided not to replace TrbNet but to develop a bridge between both networks. The adoption included the implementation of CBMNet's physical layer, the migration of its high-level functions onto a new FPGA platform as well as the design of protocols to bridge the semantically different network types.

Since TrbNet features a central trigger and read-out scheme, CBM's streaming data transport is emulated using a free-running mode of operation based on periodic pulsers. These cause the frontends to deliver their zero-suppressed data in packets with a temporal binning comparable to FlesNet's timeslices. To reduce data overhead, load adaptive trigger frequencies based on external signals, such as an spill-indicator, are supported.

As shown in Fig. 1, current network typologies foresee a single CBMNet bridge for (possibly) multiple interconnected TRB3s since TrbNet hubs are easily available; in case of bandwidth limitation multiple uplink modules are provisioned in the firmware. An unpacker software building on top of the FlesDAQ infrastructure [2] is available in

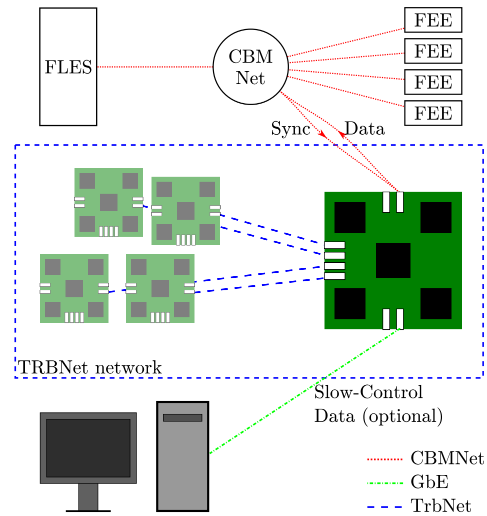

Figure 1: A typical TRB3 set-up with CBMNet bridge. If multiple boards are used, they can share a common CBMNet link. Slow-Control is available only via GbE.

CBMRoot. Additionally, a dual-stack uplink with CBMNet and GbE is feasible.

Synchronisation with native CBMNet frontends is possible by means of freely configurable DLMs. Several approaches suitable for one to many DLMs are supported and exhibit an event-to-event jitter of < 50 ps RMS after converting TrbNet timestamps into the CBMNet domain.

Graphical user interfaces to configure, monitor and debug the new firmware were developed and enable non-experts to operate the system. The network bridge was successfully used in conjunction with the current CBM-RICH prototype during a beam time in November 2014 at Cern (PS).

References

[1] C. Ugur and the TRB3 collaboration, "264 Channel TDC Platform applying 65 channel high precision (7.2 psRMS) FPGA based TDCs", IEEE NoMe TDC, October 2013

[2] D. Hutter, "CBM FLES Input Interface Developments", CBM Progress Report 2014

* This work has been supported by BMBF (05P12RFFC7), EU-FP7 HadronPhysics3, HGS-HIRe, GSI and HIC for FAIR.

Status of CBMnet readout and the prototype ASIC*

S. Schatral[1,2], *F. Lemke*[1], *and U. Bruening*[1]
[1]University of Heidelberg, Mannheim, Germany; [2]GSI, Darmstadt, Germany

Front-end read-out status

The CBMnet protocol is currently present in all stages of the CBM data acquisition (DAQ) network for the TRD and STS readout. Beside the two FEE ASICs using CBMnet links over HDMI cable, the cores are also integrated in the Read-Out Controller (ROC), the FLES Interface Board (FLIB) and further FPGA to FPGA interconnects. For these links Xilinx Gigabit Transceiver over SFPs are used. A typical setup is depicted in 1. To improve the link stability under influence of radiation, a reworked CBMnet Version 3.0 has been developed and implemented, containing a link layer, various physical layer implementations and more network related building blocks to deliver generally required features in CBM network devices. Implementations have been optimized for FPGA and ASIC use. The logic is built in such a way, that a malfunction triggered by a single event effect is detected and the corresponding functional blocks are reset. In this manner, the data acquisition over a long time is possible without any interruption. Larger test beam read-outs with up to three SPADICs per ROC have been tested in laboratory and under beam. The FLIB physical layer implementation has been tested intensively to work reliable under all conditions. The design can handle up to eight links now.

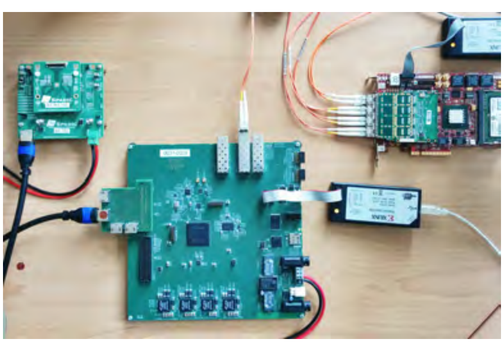

Figure 1: Read-out with FLIB, Syscore3 and SPADIC

Prototyping of a readout aggregation ASIC

A prototype of the readout and aggregation ASIC has been designed together with the Indian Institue of Technology Kharagpur (IITKGP). Therefore, an internship student from IITKGP was visiting the University of Heidelberg for half a year in 2014. This was possible because of successfully raised additional funding from the Heidelberg Center South Asia. This mixed-signal ASIC consists of a full-custom 5Gb/s serializer/deserializer, designed by the IITKGP including design elements such as phase-locked loop, bandgap reference, and clock data recovery, and a digital designed network communication and aggregation part designed by the computer architecture group of the University of Heidelberg.

In addition, there are test structures and an I2C readout integrated to ease bring up and monitoring. A specialty of this test ASIC is the aggregation of links featuring different data rates, running with bundles of 500 Mb/s LVDS [1]. This enables flexible readout setups of mixed detectors respectively readout of various chips. There are 1x, 2x, or 4x LVDS connections available enabling up to 2 Gb/s for a front-end connection. The prototype will be able to run in a mixed configuration, e.g. one 1x, two 2x, and one 4x. A prototype structure diagram depicting the link configuration possibilities is presented in figure 2. As communication protocol for the prototype, a unified link protocol is used including control messages, data messages, and synchronization messages on an identical lane. The design has been successfully simulated, verified, and hardware emulations using Spartan 6 FPGAs. The miniASIC mixed-signal design has been prepared and simulated together with the collaboration partners from the IITKGP. The first chance in 2015 for a submission using the TSMC 65nm LP Europractice process will be taken.

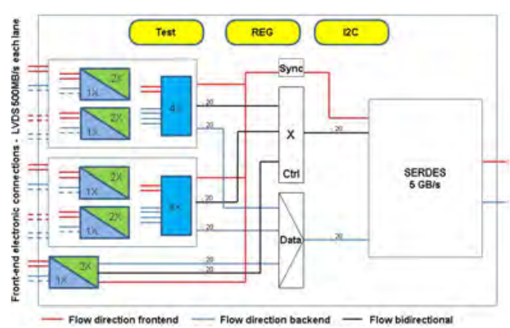

Figure 2: Link connection diagram for HUB ASIC

References

[1] S. Schatral, F. Lemke, U. Bruening, "Design of a deterministic link initialization mechanism for serial LVDS interconnects", Journal, doi:10.1088/1748-0221/9/03/C03022, VOL. 9, No. 03, pages C03022, March 2014.

* Work supported by GSI, BMBF FAIR-CBM 05P12VHFCE

Computing

CBM Component Database

E.P. Akishina, E.I. Alexandrov, I.N. Alexandrov, I.A. Filozova, and V.V. Ivanov
LIT JINR, Dubna

The CBM Component Database (DB) is designed and implemented as a part of the CBM Databases project [1] according to the User Requirements Document [2]. The Component DB is used to store and manage the properties of the detectors hardware and electronic components. It contains characteristics, statuses, test results, certificates and other parameters both numeric/strings and images. The current relational DB structure allows to use it for any CBM detector performing minor adjustments. The components of different detectors (STS, Magnet, PSD, RICH, ToF, MUCH, MVD, TRD, ECAL) will be stored in different databases. Data is accessed through the common authorization service. The Component DB has a tree structure. The root of the tree has a name of the CBM facility part such as Magnet, MVD, STS etc. The list of the detector components is stored in the tree. The tree leaf is connected to a table with according names and values. The tests, certificates and statuses are stored in DB as the references. Test of the components are images. The certificates details depend on the component and can be implemented for each detector. The catalog of different statuses can be defined for each detector separately.

The authorization for each detector is needed. The responsible person can work only with the data of corresponding detector. The Web access is organized for viewing, inserting and editing data. The implementation is realized on the basis of client-server interaction. The same schema for all subdetector was produced. Scripts and their usage in according html pages were implemented. Figure 1 presents an example of the Magnet main page. The details of the Magnet component are shown on the right. Figure 2 shows page for editing Magnet details.

Figure 1: View Mode GUI Example for Magnet

The system implementation is based on the software DBMS PostgreSQL v8.4.20. Basic services are supported:

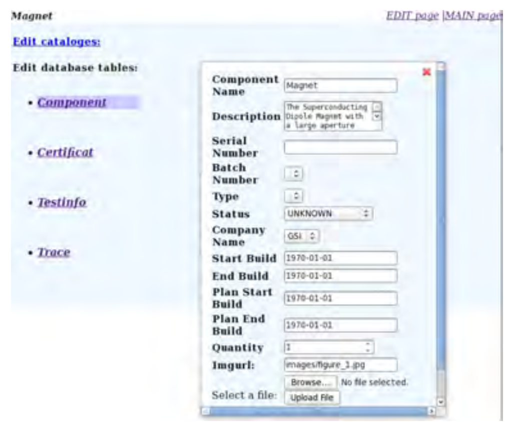

Figure 2: Edit Mode GUI Example for Magnet

data viewing for detector components, search in navigation mode, inserting and editing data for the detector component, support of the catalogs, authorization services for system access. The authorization is based on affiliation to the detectors group. There are several catalogs such as Manufacturer Companies, Component Categories, Batches Details, Quality Measurement Units, and Quality Criteria. User Guide for The CBM Component DB is developed.

Web-interface allows to work with system from any place with internet access, to reach data from mobile device on according speed level. Current Magnet Component DB is completely implemented, filled with data and available through the link: http://cbmdb.jinr.ru/magnet.main.php. STS and MVD tree structures are defined. They are going to be filled in with data after some specification. The Users Guide for Component DB support is developed and can be used [3].

References

[1] E.P. Akishina et al., "Conceptual Considerations for CBM Databases", E10-2014-103 JINR Communication, Dubna.

[2] E.P. Akishina et al., "User Requirements Document for CBM Component Database", http://lt-jds.jinr.ru/record/67403?ln=en

[3] E.P. Akishina et al., "Users Guide for CBM Component Database", http://lt-jds.jinr.ru/record/67404?ln=en

4-Dimensional Cellular Automaton Track Finder for the CBM Experiment*

V. Akishina[1,2,3] *and I. Kisel*[1,2,4]

[1]Goethe-Universität, Frankfurt am Main, Germany; [2]GSI, Darmstadt, Germany; [3]JINR, Dubna, Russia; [4]FIAS, Frankfurt am Main, Germany

The CBM experiment at FAIR will focus on the measurement of rare probes at interaction rates up to 10 MHz. The beam will provide free stream of particles, so that some events may overlap in time. It requires the full online event reconstruction not only in space, but also in time, so-called 4D (4-dimensional) event building. A time-slice is reconstructed in parallel between cores within a CPU, thus minimising communication between CPUs. This is a task of the First-Level Event Selection (FLES) package.

The FLES reconstruction package consists of several modules: track finding, track fitting, short-lived particles finding, event building and event selection. The Cellular Automaton (CA) track finder is fast and robust and thereby will be used for the online track reconstruction. This method benefits from enumeration suppression by introducing a phase of building short track segments at an early stage before going into the main combinatorial search. The reconstruction efficiency for the primary tracks with momentum higher than 1 GeV/c in case of event-based analysis (see 3D column of Table 1) is 96.1%.

As a special study of the CA track finder stability the algorithm behavior was investigated with respect to the track multiplicity. For the study a super-event, which includes a number of minimum bias events, was reconstructed with no time information taken into account. In a super-event we combine space coordinates of hits from a number of Au+Au minimum bias events at 25A GeV and give it to the CA track finder as an input to reconstruct with a regular procedure. The reconstruction efficiency dependence is stable: the efficiency for all tracks changes by 4% only for the extreme case of 100 minimum bias events in the super-event (see (3+1)D column of table 1), comparing to the case of event-based analysis.

The time information was included to the algorithm. It has resulted in a higher reconstruction efficiency (see 4D column in table 1). In particular the time information drastically decreased ghost and made the reconstruction 3.7 times faster than without the time information ((3+1)D column of Table 1). The speed now is 8.5 ms and comparable with the event-based analysis. The CA track finder was fully parallelised inside the time-slice. The parallel version shows the same efficiency as a sequential one and achieves a speed-up factor of 10.6 while parallelising between 10 Intel Xeon physical cores with a hyper-threading.

The first version of event building based on 4D track finder was implemented. The hits time measurements distribution illustrating the complexity of defining event borders in a time-slice is shown Figure 1 with blue color, the resulting distribution of reconstructed track time – with black. Reconstructed tracks clearly represent event-corresponding groups. The FLES package is ready for the 4D reconstruction of time-slices in CBM.

Efficiency, %	3D	(3+1)D	4D
All tracks	83.8	80.4	83
Primary high-p	96.1	94.3	92.8
Primary low-p	79.8	76.2	83.1
Secondary high-p	76.6	65.1	73.2
Secondary low-p	40.9	34.9	36.8
Clone level	0.4	2.5	1.7
Ghost level	0.1	8.2	0.3
Time/event/core	8.2 ms	31.5 ms	8.5 ms

Table 1: Track reconstruction performance for 3D event-by-event analysis, super-event (3+1)D and time-based 4D reconstruction for 100 mbias Au+Au collisions at 25A GeV.

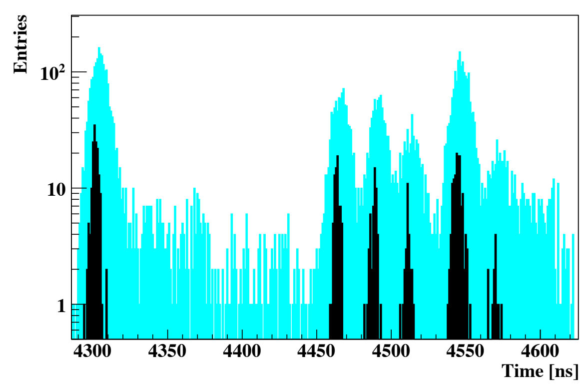

Figure 1: Distribution of time measurement in a part of a time-slice at the interaction rate of 10^7 Hz: hit time measurement (light blue), track time (black).

References

[1] I. Kisel, I. Kulakov, and M. Zyzak, "Standalone First Level Event Selection Package for the CBM Experiment", IEEE Transactions on Nuclear Science, 60 (2013) 3703

[2] V. Akishina, I. Kisel, "Online 4-Dimensional Reconstruction of Time-Slices in the CBM Experiment", submitted to IEEE Transactions on Nuclear Science

* Work supported by HICforFAIR, FIAS and HGS-HIRe for FAIR.

On a performance of $J/\psi \to e^+e^-$ reconstruction algorithms

O.Yu. Derenovskaya and V.V. Ivanov
LIT JINR, Dubna, Russia

The measurement of J/ψ decays is one of the key goals of the CBM experiment. The procedure of the J/ψ registration in its dielectron channel includes a chain of methods and corresponding algorithms for trajectories and momenta reconstruction of charged particles with STS, electron/positron identification with RICH, TRD and TOF, as well as construction of the J/ψ-candidates and their characteristics using the KFParticle package [1]. Taking into account that selection and reconstruction decays of $J/\psi \to e^+e^-$ are planned to be carried out in real time of the CBM experiment, the used methods and algorithms should be not only effective but also fast.

In this paper the time-consuming estimation of the existing algorithms based on their acceleration via code vectorization by means of SIMD instructions and parallelization between the processor cores that are implemented using different software environments has been carried out (see details in [2]).

Table 1 presents the speedup factors of the algorithms (Cellular Automaton and Kalman Filter in the STS, ring reconstruction with RICH, electron identification in the TRD applying the ω_n^k criterion, KFParticle package) obtained with using SIMD instructions.

STS: CA	STS: KF	RICH: ring reconst.	TRD:el.id. with ω_n^k	KFParticle
2	4	2	3.5	2.5

Table 1: Speedup factors of the algorithms obtained with using SIMD instructions

It should be noted that there is a certain reserve to accelerate the computing in this way, because some algorithms, such as the track reconstruction of the charged particle with the TRD is not subjected to vectorization, and others, for example KFParticle package, is not vectorized fully. In the case of the maximum possible optimization and vectorization of all algorithms, the total acceleration factor may be considerably higher.

According to preliminary estimates, the share of central collisions in the real experiment should not exceed 1 %. In this regard, we used the events, corresponding to a mixture of the central (1 %) and Minimum Bias (99 %) AuAu-collisions at 25 AGeV to determine the performance of the algorithms. Furthermore, to avoid dependence of the algorithms to the particles multiplicity produced in one AuAu-collision, we calculate an average time Δt, which specific algorithm takes for processing a single trajectory. To do it the following formula is used:

$$\Delta t = \frac{t_{mbias}}{N_{mbias}} \cdot 0,01 + \frac{t_{centr}}{N_{centr}} \cdot 0,99, \qquad (1)$$

where t_{mbias} is the average time spent by the algorithm on one MB-events and t_{centr} is the same value for one central event; M_{bias} and M_{centr} are average numbers of the reconstructed tracks in one MB and one central event, respectively.

Table 2 presents the average time Δt (in μs/track or μs/ring) which $J/\psi \to e^+e^-$ reconstruction algorithms spend on data processing. Note that the presented results are referred to the SIMD-algorithms (besides the track reconstruction with the TRD) and obtained using one logical CPU core.

STS: CA	STS: KF	RICH: ring reconst.	TRD: track reconst.	TRD: el.id. with ω_n^k	KFParticle
164.5	0.5	49	1390	0.5	9.15

Table 2: Average time Δt (in μs/track or μs/ring) which described SIMD-algorithms spend on data processing

Table 2 shows that time spent by the algorithm of track reconstruction of charged particles in the TRD, many times exceeds the summing time of all the other algorithms. It should be noted that an alternative approach to track finder in the TRD, based on a Cellular Automaton is now under development [3]. It is expected that the new algorithm will be not inferior in efficiency to the existing method but more reliable and productive.

All of the above algorithms were adapted in software environments (OpenMP, OpenCL and TBB) for parallel computation on high performance hybrid servers constructed on the basis of multi-core CPU and GPU. All algorithms shows a good linear scalability in depending on the number of the cores included in the processing.

The analysis of the algorithms scalability has allowed us to estimate the acceleration of data processing using the technologies for high performance computing and identified “weak” places in the chain of the methods for J/ψ reconstruction (track reconstruction in TRD), over which is under investigation.

References

[1] O.Yu. Derenovskaya, V.V. Ivanov // PEPAN, Letters, T.11 , No.4 (188) , 2014, pp. 862-885.

[2] O.Yu. Derenovskaya, V.V. Ivanov // Bulletin of PFUR, Series Matematics. Information Sciences. Physics. No. 4, 2014, pp. 50-67.

[3] T.O. Ablyzimov, V.V. Ivanov, this report.

Event Building Process from Time Stream Data

V. Singhal[1], *S. Chattopadhyay*[1], *and V. Friese*[2]

[1]Variable Energy Cyclotron Centre, Kolkata, India; [2]GSI, Darmstadt, Germany

Upto now all the High Energy Experiments are based on the hardware triggered approach, which means a specific set of hardware, signals the entire elecronics to collect the data, this is known as triggered electronics. This signal define the event boundary, therefore all the available simulation and reconstruction software are working on the event by event basis. On the contrary due to unprecedented interaction rate at the CBM experiment conventional triggered electronics will not work, therefore building of trigger less electronics have been under development. In this scenario, the event boundary will not be defined by any hardware. This implies a novel read-out and data acquisition concept with self-triggered front-end electronics which will generate free-streaming data. To do the analysis from this time stamped free steam data, event association must be performed in software. To simulate the free stream data, work has been under development [1] to change the CBMROOT framework in the direction of putting timestamp on each and every digi (digi is the smallest piece of raw data known as one hit which detected by triggerless electronics).

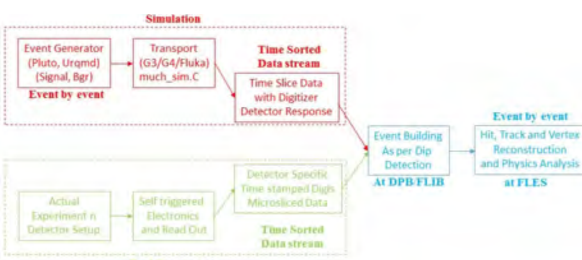

Figure 1: Simulation and analysis process chain.

To use all the available software for processing of free stream time stamped data, generated by CBM experiment, an event association package has to be introduced at the appropriate place in the simulation, reconstruction and analysis chain which will separate one event to another and also this should cater to actual experiment data processing. Fig. 1 shows proposed process chain for both simulation and real experiment. Fig. 1 shows that all the available hit, track, vertex reconstruction and physics analysis packages can be used if a new process named event building introduced which will convert timestamped data stream into event by event data stream.

Report describes that how we are going to address this issue. Time stamped raw data stream have been generating via simulation and each detector will generate separate raw data stream like STS data stream, MUCH data stream etc and all will be stored in a ROOT Tree. In actual scenario also different detectors will generate different stream of digis with time stamp. As a first step towards the reconstruction of such free-streaming data, we introduced an event-building process which tags physical events based on the time information of the raw data. Process counts the digis in each nano second and put these values in nanosecond vector. Then the process identifies and analyzes dips in the continuous nanosecond vector. Data between two dips indicates probable event candidate, which then further analysed with respect to a number of parameters like minimum and maximum number of digis per event,average event duration etc. Fig. 2 shows the flowchart for event building process. In this process a vector indexed nanosecond created, which contain $<$ No. of Digis in the nanoslice, starting index of first digi of this nanoslice$>$. Presently our sample set contain free time stream data only for the muon detector system (MUCH).

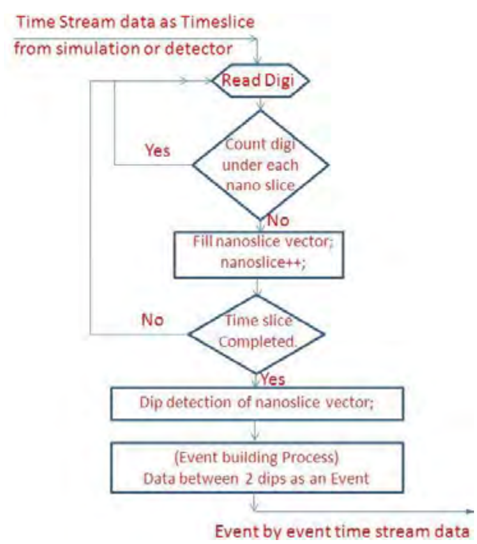

Figure 2: Flowchart for proposed Event Building

Fine tuning of the eventbuilding process has been going on with respect to MUCH on the basis of different parameters and thereafter same will be developed for the other detector systems. If once event could be defined with respect to all the detector thereafter, all available reconstruction algorithms, working event-by-event basis, could be used without any modification for processing time stamped free stream data.

References

[1] V. Friese, J. Phys.: Conf. Ser. 331 032008 (2011) "Simulation and reconstruction of free-streaming data in CBM"

Event-by-event extraction of kinetic and chemical freeze-out properties in the CBM experiment*

V. Vovchenko[1,2,3,4], *I. Kisel*[1,2,3], *and D. Anchishkin*[4,5]

[1]Goethe University, Frankfurt, Germany; [2]GSI, Darmstadt, Germany; [3]FIAS, Frankfurt, Germany; [4]Taras Shevchenko University, Kiev, Ukraine; [5]Bogolyubov Institute for Theoretical Physics, Kiev, Ukraine

The future CBM experiment at FAIR is designed to study properties of strongly interacting matter produced in heavy-ion collisions at high baryon densities. It will employ high intensity beams and large acceptance detectors. One important task is to extract the thermal parameters of matter at stages of kinetic and chemical freeze-out from the observed data. The extraction of thermal parameters is implemented as a package within the CBMROOT framework.

The kinetic freeze-out temperature of charged pions is extracted from their measured momentum spectrum. In the simplest scenario the particles are assumed to have a Boltzmann momentum distribution with no collective flow. To test the method, a 1000 Monte Carlo (MC) events with thermally distributed pions ($T = 128$ MeV) were generated and then processed in CBMROOT. Reconstructed STS Tracks, as well as the initial MC Tracks, were used to calculate the average transverse mass of pions $\langle m_T \rangle$, which was then used to estimate the temperature. Due to limited detector acceptance, and due to imperfect reconstruction efficiency, the mean transverse mass of STS tracks differs from the MC one. Therefore, an appropriate correction was performed using the known momentum dependence of acceptance function and reconstruction efficiency. Figure 1 depicts the extracted Boltzmann temperature on the event-by-event level. It is seen that the extracted temperature has a Gaussian-like distribution around the theoretical value of 128 MeV when one uses MC Tracks (blue line) or STS Tracks with proper correction on acceptance (red line). If one neglects this correction on acceptance then one gets essentially different (incorrect) value of temperature (green line). The procedure, developed for this model, can be used as a basis for analysis in the framework of more complex and more realistic models.

The parameters of the chemical freeze-out are extracted by fitting the measured particle ratios in the framework of the Hadron Resonance Gas model. All strange and non-strange hadrons which are listed in the Particle Data Tables are included and the model is implemented in CBMROOT and works similarly to the THERMUS package [1]. The grand canonical ensemble formulation is used and excluded volume corrections are included in the framework of the thermodynamic mean-field approach [2]. The fit can be performed on event-by-event level and also on the inclusive spectra level. Figure 2 shows the extracted temperature and baryonic chemical potential from MC events generated in the thermal model with $T = 100$ MeV and $\mu_B = 550$ MeV. For each parameter extraction a set of 10 events was used, and the fit error estimates were calculated and depicted as well. The extracted values are consistent with the theoretical input.

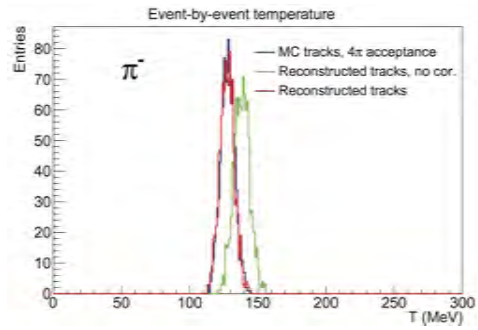

Figure 1: The temperature of pions extracted on event-by-event level using the MC tracks (blue line), STS tracks without acceptance correction (green line), and STS tracks with correction on acceptance (red line).

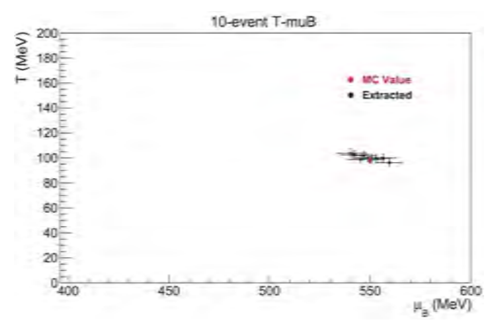

Figure 2: The temperature and the baryonic chemical potential extracted from the 10-event sets in the framework of the Hadron Resonance Gas model. The theoretical MC values is shown by the red dot.

References

[1] S. Wheaton, J. Cleymans, and M. Hauer, "THERMUS — A thermal model package for ROOT", Comput. Phys. Commun. 180 (2009) 84.

[2] D. Anchishkin and V. Vovchenko, "Mean-field approach applied to relativistic heavy-ion collisions", arXiv:1411.1444 [nucl-th]

*Work supported by the Hessian LOEWE initiative through the Helmholtz International Center for FAIR (HIC for FAIR)

A "vector finding" approach to track reconstruction in CBM MUCH

A. Zinchenko[*], *V. Myalkovskiy, D. Peshekhonov, and V. Peshekhonov*
LHEP JINR, Dubna, Russia

The existing track reconstruction method in CBM MUCH is based on the track following approach. It consists in the STS track propagation through the MUCH subsystem using the Kalman filter procedure. Although quite straightforward, this method has some deficiencies such as a necessity to run a prior STS reconstruction or the effect of the absorbers, which blow up the track covariant matrix and make hit selection right behind them rather difficult in high hit density environment (in first stations) or for one-coordinate detectors (straw tubes - Fig. 1).

Here an alternative approach to the track reconstruction task in MUCH is described based on a so-called "vector reconstruction" procedure [1]. The idea is to build track segments (vectors) for each MUCH station and merge them with each other (and with STS tracks at the end) through the absorbers. This approach offers some advantages (beside being alternative): vector finder can be run for all stations in parallel and the procedure is rather simple (straight line fit of a few measurements), there is a possibility to trigger on di-muons, the damaging effect of absorbers is excluded at the first stage of reconstruction allowing to fully exploit coordinate reconstruction accuracy for handling hit combinatorics.

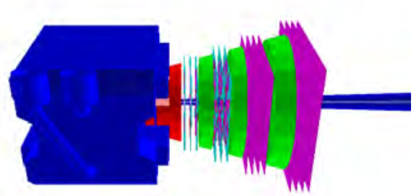

Figure 1: SIS100 CBM muon system configuration with straw tubes comprising two last detector stations.

Vector finder in the magnetic field-free region can be realized very efficiently using the solution of the linear equation system from the Least Squares Method (LSM). It consists in finding the minimum value of the χ^2 - functional (for 2-D detectors):

$$\chi^2 = \sum_{i=1}^{N_{planes}} \Big[\frac{(x(z)-x_i)^2}{\sigma_{x_i}^2} + \frac{(y(z)-y_i)^2}{\sigma_{y_i}^2}\Big],$$

where $x(z) = x_0 + T_x \cdot z$ and $y(z) = y_0 + T_y \cdot z$ are the vector equations in two planes with track parameters (x_0, y_0, T_x, T_y) and sum is taken over the number of planes in the detector station (i.e. the number of points with coordinates (x_i, y_i) and errors $(\sigma_{x_i}, \sigma_{y_i})$). Similar expression can be written for one-dimensional detectors (straw tubes).

The minimum value of χ^2 is found by taking its partial derivatives with respect to track parameters and setting them to 0. As a result, the following system of equations is obtained (for 2-D detectors - GEMs):

$$\sum_i \begin{pmatrix} 1 & 0 & z_i & 0 \\ 0 & 1 & 0 & z_i \\ z_i & 0 & z_i^2 & 0 \\ 0 & z_i & 0 & z_i^2 \end{pmatrix} \begin{pmatrix} x_0 \\ y_0 \\ T_x \\ T_y \end{pmatrix} = \sum_i \begin{pmatrix} x_i \\ y_i \\ x_i \cdot z_i \\ y_i \cdot z_i \end{pmatrix}.$$

Here it is assumed that the measurement errors are the same for all hits in a station, which is a reasonable approximation for MUCH. One can see that the left matrix does not depend on individual hit measurements and can be called a configuration matrix $\mathbf{A}$. As such, it can be computed at the initialization stage and kept in memory for the whole processing. The configuraton matrices also define the covariance matrices of the fitted vector parameters $\mathbf{V} = \sigma^2 \cdot \mathbf{A}^{-1}$.

The above formalism is used as follows: for each detector station, different hit combinations are fitted to straight lines. Combinations with high χ^2-value are rejected. To reduce hit combinatorics, some a priori constraints can be applied (e.g., vector angles). At the next step, vectors from sequential stations are merged through the absorbes, taking into account multiple scattering in the absorber material and covariance matrices of vectors. Again, only vector pairs with low enough matching χ^2 are accepted. At the end, matching with STS tracks is done.

Some results on vector matching in two last stations are presented in Tab. 1. Here the signal muon pair efficiency (from ω decays) is shown along with the average number of background tracks in central Au-Au collisions at 8 AGeV. The background tracks include the "real" tracks, i.e. the ones from real particles (punchthrough hadrons or decay muons) and "ghosts", i.e. combinations of two vectors from different particles. Although the results are very preliminary, one can see that MUCH configuration with straw tubes demonstrates somewhat better performance (due to higher coordinate resolution).

Geometry	Efficiency,%	⟨ Bkg. tracks / event⟩	
		"real"	"ghost"
GEM	4.3±0.3	1.23±0.02	0.50±0.01
Straws	4.9±0.3	1.22±0.02	0.30±0.01

Table 1: Tracking efficiency for the dimuon signal and background track rate.

References

[1] A. Zinchenko *et al.*, CBM Progress Report 2010, Darmstadt, 2011, p.38

* Alexander.Zinchenko@jinr.ru

Physics Performance

TOF PID

S.M. Kiselev[1]
[1]ITEP, Moscow, Russia

10^6 Au+Au UrQMD events at 4, 10 AGeV (for the setups A, B and C), 25 and 35 AGeV (for the setup C) simulated and reconstructed in the frame of the CbmRoot package have been used for analysis. Setups A: SIS100 with TOF at 6m, B: SIS100 with TOF at 10m, C: SIS300 with TOF at 10m. The TOF resolution σ_{TOF}=80 ps was taken in the TOF hit producer. For global track matching with TOF hits the "nearest hit" mode was selected.

Figure 1 (left) shows distribution of global tracks with the vertex cut for selecting primaries. For different species the PID regions on the plane (p, m^2) are defined in Fig. 1 (right). To increase purity for anti-protons the tracks from the "white" region (mostly includes protons) are excluded from the PID analysis. PID efficiency is defined as a ratio of the correctly identified tracks to the all global tracks, PID purity is a ratio of the correctly identified tracks to the all tracks from the PID region.

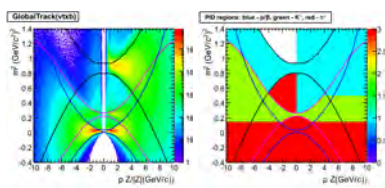

Figure 1: Setup A. Central Au+Au events at 10 AGeV. (left) Distribution of global tracks with the vertex cut on the plane (p, m^2). (right) PID regions for different species. $\pm 3\sigma_p(p)$, $\pm 3\sigma_K(p)$ and $\pm 3\sigma_\pi(p)$ boundaries are shown by lines.

Figures 2 and 3 present PID efficiency and purity at beam energies 4 and 10 AGeV respectively. At 4 AGeV multiplicity of anti-protons is very low, 3×10^{-5} per event, and statistic is not enough. At 10 AGeV multiplicity of anti-protons is 10^{-2} per event. In spite of high PID efficiency for anti-protons, its PID purity is low $\sim 0.1 - 0.2$ due to large contribution of tracks from protons. PID results weakly sensitive to beam energy (4/10 AGeV) and TRD (with/without TRD). In the momentum region $1 < p < 3 - 4$ GeV/c PID efficiency is high, $\sim 0.9 - 1$, PID purity > 0.8, except for anti-protons.

Figure 4 presents PID efficiency and purity at 10, 25 and 35 AGeV with the setup C. PID efficiency is low sensitive to the beam energy. PID purity is most sensitive for anti-protons, it increases with the energy up to ~ 0.4 at 35 AGeV. For other species PID purity changes within $5 - 10\%$.

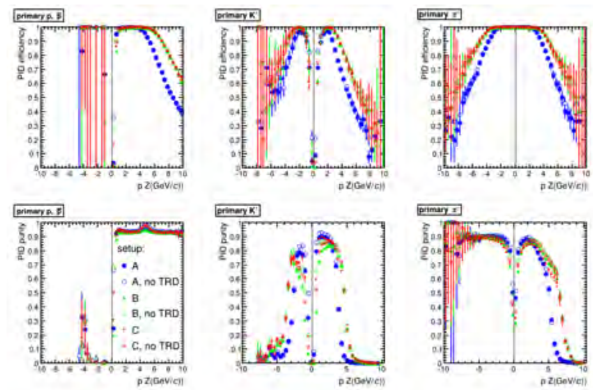

Figure 2: PID efficiency and purity for minimum bias Au+Au events at 4 AGeV with the setups A, B and C.

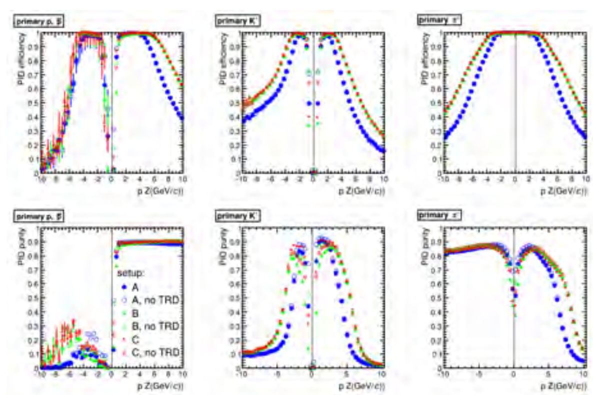

Figure 3: PID efficiency and purity for central Au+Au events at 10 AGeV with the setups A, B and C.

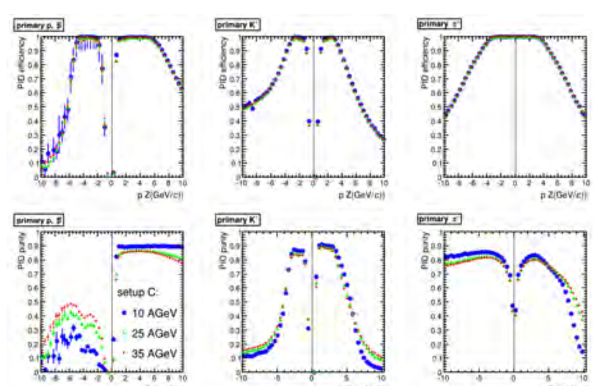

Figure 4: Setup C. PID efficiency and purity for central Au+Au events at 10, 25 and 35 AGeV.

Reconstruction of Σ hyperons with ECAL at SIS100

S.M. Kiselev[1]
[1]ITEP, Moscow, Russia

The feasibility of Σ hyperons reconstruction using the ECAL was studied on samples of UrQMD events at the SIS100 energies: 10^7 p+C and 10^6 p+Cu minimum bias events at 10 GeV, 10^6 minimum bias and 10^6 head-on p+C events at 30 GeV. The set-up consists of MVD, STS, TOF and ECAL wall of the size X×Y=5.76 $\times$ 8.64 m^2 with the beam gap $|Y| < 0.48$ m distanced from a target at 12 m. Reconstructed photons with $p > 0.3$ GeV/c and $\chi^2_{cluster} <$ 1000 have been taken for the analysis. We analyzed the decays $\Sigma^0 \to \Lambda\gamma$ and $\Sigma^+ \to p\pi^0$.

1. $\Sigma^0 \to \Lambda\gamma$. For the reconstruction of $\Lambda \to p\pi^-$ PID information was not exploited. Λ is named by "accepted" if each of its decay products has MC points in at least 4 STS stations and by "reconstructed" if each decay product has the reconstructed track ($\geq$ 70 % of track hits belong to the same MC track). Single track cut: impact parameter in the target plane for positive and negative tracks (in σ) > 4. Vertex quality cuts: χ^2 of the fitted vertex < 2, distance of closest approach $<$ 0.2 cm. Additional topological cuts: impact parameter of the reconstructed mother track $<$ 0.15 cm, position of the fitted decay vertex along the beam axis in the range 3 - 25 cm. The reconstructed Λ within the range $m_\Lambda \pm 25$ MeV and reconstructed γ have been chosen as candidates for Σ^0 analysis. Figure 1 (left) shows an example of the invariant mass distributions of signal and background $\Lambda\gamma$ pairs. Table 1 summarize characteristics of

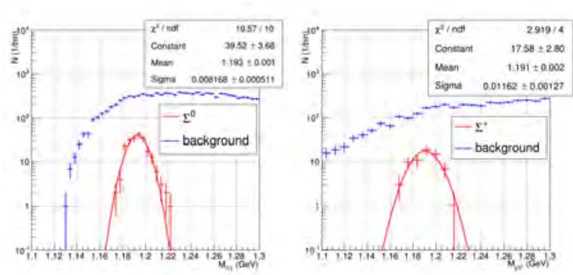

Figure 1: Invariant mass spectra of signal and background $\Lambda\gamma$ (left) and $p\pi^0$ (right) pairs for head-on p+C events at 30 GeV

the analysis: signal yield, acceptance, reconstruction and cut efficiencies, signal-to-background ratios $S/B_{\pm 2\sigma}$ and significances.

2. $\Sigma^+ \to p\pi^0$. For π^0 candidates the pairs with 0.124$< M_{\gamma\gamma} <$ 0.144 GeV/c were selected. No PID was used to select the proton candidates. The positive tracts with the impact parameter in the target plane (in σ) > 5 have been used to reject the positive primaries. Figure 1 (right) shows an example of the invariant mass distributions of signal and background $p\pi^0$ pairs of selected candidates.

Table 1: $\Sigma^0 \to \Lambda\gamma$

system	yield /event	acc. eff.	rec. eff.	cut eff.	S/B /sign.
pC@10	0.004	0.027	0.45	0.12	0.11/2.2
pCu@10	0.017	0.015	0.45	0.13	0.11/1.2
pC@30	0.009	0.042	0.61	0.26	0.08/2.1
pC@30,b=0	0.029	0.042	0.59	0.30	0.08/3.9

Table 2 summarize characteristics of the analysis. Due to

Table 2: $\Sigma^+ \to p\pi^0$

system	yield /event	acc. eff.	rec. eff.	cut eff.	S/B /sign.
pC@10	0.008	0.011	0.46	0.03	0.08/1
pCu@10	0.018	0.007	0.47	0.02	-
pC@30	0.010	0.022	0.50	0.14	0.04/1
pC@30,b=0	0.030	0.019	0.56	0.19	0.07/2.1

lower efficiencies we have $\sim$ 5 times lower the number of signal pairs than for the channel $\Sigma^0 \to \Lambda\gamma$. To estimate S/B for the p+Cu system statistics is not enough.

Results for the head-on p+C events at 30 GeV agree with those obtained with light ECAL in [1].

In order to achieve a reasonable significance level of about 10, two order higher event statistics is required.

References

[1] S.M. Kiselev, *Reconstruction of Σ hyperons with light ECAL in p+C at SIS100*, CBM Progress Report 2012, GSI Darmstadt, p. 105.

Reconstruction of $\eta'(958)$ with ECAL at SIS100

S.M. Kiselev[1]

[1]ITEP, Moscow, Russia

The feasibility of $\eta'(958)$ reconstruction using the ECAL was studied on samples of UrQMD events at the SIS100 energies: 10^7 p+C and 10^6 p+Cu minimum bias events at 10 GeV, 10^6 minimum bias and 10^6 head-on p+C events at 30 GeV. The set-up consists of MVD, STS, TOF and ECAL wall of the size X×Y=5.76 × 8.64 m^2 with the beam gap $|Y| < 0.48$ m distanced from a target at 12 m. Reconstructed photons with $p > 0.5$ GeV/c and $\chi^2_{cluster} < 1000$ have been taken for the analysis. We analyzed the decay $\eta'(958) \to \pi^+\pi^-\eta$ (BR=43%).

In the invariant mass spectrum of MC primaries there is a peak at $m_{\eta'(958)}$. Figure 1 demonstrates an example for p+Cu at 10 GeV. We assume that triples of primaries

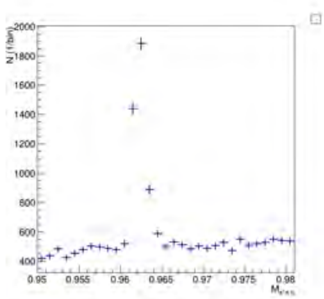

Figure 1: Invariant mass spectra of $\pi^+\pi^-\eta$ triples of primaries for p+Cu at 10 GeV

in the range $0.960 < M_{\pi^+\pi^-\eta} < 0.964$ GeV are from "primary" $\eta'(958)$. There is large background, the part of the "primary" $\eta'(958)$ corresponding to the signal is ∼60 %.

An example of invariant mass distributions for $\gamma\gamma$ pairs around η mass is shown in Fig. 2. The peak from η

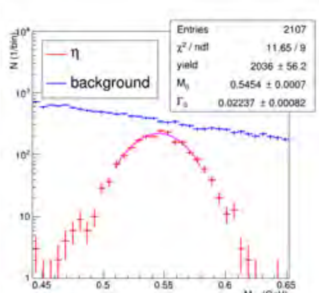

Figure 2: Invariant mass spectra of $\gamma\gamma$ pairs with $p_T^{\gamma\gamma} > 0.2$ GeV/c for p+C at 10 GeV

has σ ∼20 MeV. For η candidates the pairs with 0.530< $M_{\gamma\gamma} <$ 0.560 GeV/c were selected.

PID information was not used to select π^+ and π^- candidates. The impact parameter cut < 4 (in σ) was used to reject secondary charged tracks.

Figure 3 shows an example of invariant mass distributions for selected $\pi^+\pi^-\eta$ triples. Table 1 summarizes char-

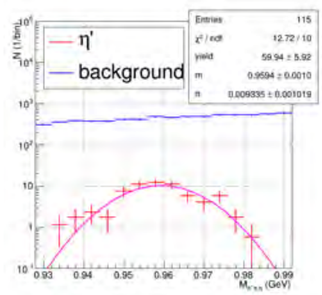

Figure 3: Invariant mass spectra of selected $\pi^+\pi^-\eta$ triples for head-on p+C collisions at 30 GeV

acteristics of the analysis: signal yield, acceptance, reconstruction and cut efficiencies, signal-to-background ratios $S/B_{\pm 2\sigma}$ and significances. To estimate S/B for the p+Cu

Table 1: $\eta'(958) \to \pi^+\pi^-\eta$

system	yield x100	acc. eff.	rec. eff.	cut eff.	S/B /sign.
pC@10	0.09	0.011	0.98	0.29	0.061/1.0
pCu@10	0.45	0.057	0.96	0.12	-
pC@30	0.3	0.035	0.99	0.45	0.014/0.6
pC@30,b=0	1.1	0.030	0.99	0.37	0.014/1.0

system statistics is not enough. In order to achieve a reasonable significance level of about 10, two order higher event statistics is required. The channel $\eta' \to \pi^0\pi^0\eta$ (BR=22%) has one order lower total detection efficiency and needs even more statistics. Due to low branching the channel $\eta' \to \gamma\gamma$ (BR=2%) also requires higher statistics.

Results for the head-on p+C events at 30 GeV agree with those obtained with light ECAL at 6 m in [1].

References

[1] S.M. Kiselev, *Reconstruction of $\eta'(958)$ hyperons with light ECAL in p+C at SIS100*, CBM Progress Report 2012, GSI Darmstadt, p. 104.

Background rejection in the dilepton analysis with the CBM-Micro Vertex Detector*

E. Krebs[1], *T. Galatyuk*[2,3], *and J. Stroth*[1,3] *for the CBM collaboration*
[1]Goethe-Universität, Frankfurt, Germany; [2]Technische Universität Darmstadt, Germany; [3]GSI Darmstadt, Germany

The light vector mesons ρ, ω and ϕ are excellent probes of the strongly interacting matter under extreme conditions. Their leptonic decay channels of interest as leptons leave the hot and dense fireball without strong interaction and may reveal information on the characteristics of the matter created in the collisions. Single electron or positron tracks from incompletely detected γ-conversions and Dalitz decays of π^0-mesons are the most abundant source contributing to the significant combinatorial background. This study aims at exploring the use of MVD hits topology to reduce this background, despite of the fact that additional background is produced due to the material budget of the MVD.

To do so, electron pairs from meson decays have been simulated from a thermal source for central Au+Au reactions at SIS-100 energies such that the meson spectra are consistent with p_T and rapidity distributions measured by NA49 [1]. The decays of various sources simulated with the Pluto[2] event generator are embedded into the hadronic environment calculated with UrQMD transport model calculations. The magnetic field was set to 100% strength and δ-electrons with energies above 1 MeV have been added equivalent to a 10 kHz interaction rate.

The strategy of background rejection comprises several steps. In order to identify leptons from photon conversions that were produced outside of the target region, each reconstructed track is extrapolated to the primary decay vertex and removed from the analysis depending on its deviation to the vertex. One characteristic for conversion pairs is their small opening angle. A wedge cut is applied taking into account the opening angle of an identified electron to its closest neighbor with particle identification and product of the momenta of the two tracks. As lepton tracks from background sources can predominantly be found at low transverse momenta such tracks are rejected as well [3].

The MVD of the CBM experiment can further contribute to reduce this background by including points from the MVD into the track reconstruction. An improved rejection of pairs originating from the target region could be observed. Previous studies have shown that the MVD stations are also a source for γ conversions which can not be effectively rejected by the vertex extrapolation cut, especially in the first two stations closest to the target. Extrapolating tracks to the first MVD station and requiring that they are in its acceptance helped to better suppress off-vertex tracks from γ-conversions and resulted in an improved signal-to-background ratio for the low mass vector mesons ρ, ω and ϕ as depicted in Tab. 1. The invariant mass spectrum of the full cocktail after all analysis steps is presented in Fig. 1.

*This work has been supported by BMBF (05P12RFFC7), HIC for FAIR, HGS-HIRe, H-QM, and GSI.

Mass Range $\left[\frac{\mathrm{GeV}}{\mathrm{c}^2}\right]$	MVD Stations	S/B	$\mathrm{S}/\sqrt{\mathrm{S}+\mathrm{B}}$
$0 - 0.15$	0 4	6.56 8.27	31.3 29.4
$0.15 - 0.6$	0 4	0.10 0.14	3.7 3.7
$0.6 - 1.2$	0 4	0.15 0.21	4.9 5.4
$\omega \to e^+e^-$	0 4	0.67 0.96	7.4 8.0
$\phi \to e^+e^-$	0 4	0.13 0.19	0.74 0.86

Table 1: Signal-to-background ratios and significance for dilepton decays in different mass regions.

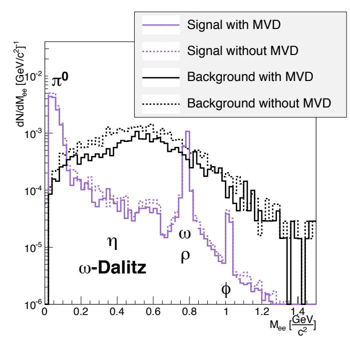

Figure 1: Invariant mass spectrum after all cuts are applied for central AuAu collisions at 8AGeV.

There have been major updates to the CBM software with more realistic digitization and geometries for the CBM detectors, including the MVD [4]. The effects on the dielectron reconstruction are under investigation.

References

[1] C. Alt et al. (NA49 Collaboration), Phys. Rev. C 78, 044907 (2008)
[2] I. Froehlich et al., arXiv:0708.2382
[3] T. Galatyuk, PhD Thesis, Goethe-Universität, Frankfurt am Main, (2009)
[4] S. Amar-Youcef et al., Status of the CBM MVD simulation model, this report

Collision centrality determination in the CBM experiment*

V. Mikhaylov†[1,2], *M. Golubeva*[3], *A. Kugler*[1], *S. Seddiki*[4], *I. Selyuzhenkov*[4], *and P. Tlusty*[1]
[1]NPI of ASCR, Řež, Czech Republic; [2]CTU, Prague, Czech Republic; [3]INR RAS, Troitsk, Russia; [4]GSI, Darmstadt, Germany

The magnitude of the impact parameter b in a heavy-ion collision is not known experimentally. The multiplicity of the produced particles in the overlap zone of the nuclei is used as an experimental proxy of the b value. All events are sorted in centrality classes, with most central ($b \approx 0$) being the collisions with highest multiplicity of the produced particles and peripheral (b being about the sum of the radii of the two nuclei) with low multiplicity. Since the b value and particle multiplicity are correlated only on average, for a given multiplicity (centrality) class of events only an average $\bar{b}$ value and its spread σ_b can be estimated.

Projectile Spectator Detector (PSD) of the CBM experiment is designed to register forward spectator nucleons and fragments emitted in nucleus-nucleus collisions at very low polar angles. It will be used to determine the collision centrality and the reaction plane orientation. The multiplicity of the spectators (collision fragments) can be also used as an independent way to determine centrality which is important for physics studies such as event-by-event fluctuations at midrapidity of various physics observables. In the case of spectator measurements, the most central events correspond to a low spectator multiplicity (small energy deposition in the PSD), while peripheral events result in large amount of spectators (large energy deposition in the PSD).

Performance of the centrality determination was studied using DCM-QGSM heavy-ion collision event generator [1] for PSD as a standalone detector utilizing correlation between energies deposited in the PSD subevents (segments), and in combination with the CBM Silicon Tracking System (STS) which measures the multiplicity of the produced particles. In the case of the PSD standalone analysis, it was required to have at least 40 GeV of energy in the PSD1 subevent or total energy in two PSD2 and PSD3 subevents of 15 GeV to exclude very peripheral collisions with only few heavy fragments.

Figure 1 shows performance of the centrality determination for Au+Au collisions at E_{beam} = 10 AGeV and PSD positioned at 8 m from the target with different centrality classes defined with different detector combinations. The top panel shows the average impact parameter value $\bar{b}$ (central value) and σ_b (as the error bars) versus centrality estimate from different subevent correlations. The bottom panel presents the same information in terms of impact parameter resolution $\sigma_b/\bar{b}$ of different centrality estimators. The $\bar{b}$ and σ_b were determined from Gaussian fits of the impact parameter distribution for a given centrality class.

The results in Fig. 1 demonstrate that the PSD can be used standalone for the centrality determination and, depending on the collision energy, has a comparable impact parameter resolution $\sigma_b/\bar{b}$ to that of the STS. This provides an independent method in the CBM experiment for the centrality determination based on spectator fragments. When used in a combination with the STS detector, the PSD helps to improve the overall centrality determination in the centrality range of 0-40% and allows for centrality determination in narrow classes with a width of at least 5%.

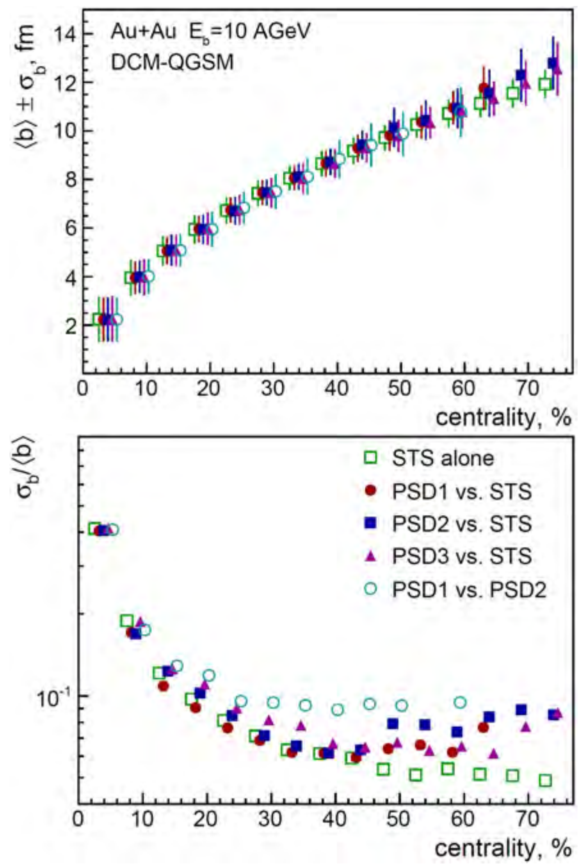

Figure 1: Average $\bar{b}$ and width σ_b of the impact parameter distribution (top); impact parameter resolution ($\sigma_b/\bar{b}$) vs. centrality (bottom).

* Work supported by the European Community FP7 - Capacities, contract HadronPhysics3 n°283286.

† mikhaylov@ujf.cas.cz

References

[1] The SHIELD code, www.inr.ru/shield/index.html.

Anisotropic flow and reaction plane reconstruction with the CBM experiment*

V. Mikhaylov[†1,2], *M. Golubeva*[3], *A. Kugler*[1], *V. Kushpil*[1], *S. Seddiki*[4], *I. Selyuzhenkov*[4], *and P. Tlusty*[1]
[1]NPI of ASCR, Řež, Czech Republic; [2]CTU, Prague, Czech Republic; [3]INR RAS, Troitsk, Russia; [4]GSI, Darmstadt, Germany

Projectile Spectator Detector (PSD) of the CBM experiment is designed to register forward spectator nucleons and fragments emitted in nucleus-nucleus collisions at very low polar angles. It will be used to determine the orientation of the collision reaction plane. The accuracy of the reaction plane determination with PSD depends on the multiplicity and energy distribution of spectators and the magnitude of their directed flow, v_1.

The PSD performance is studies with simulated Au+Au collisions in the beam energy range 2-30 AGeV, which corresponds to that of future accelerator rings SIS100/SIS300 at FAIR. To identify the most suitable heavy-ion event generator for the performance study, the simulated directed flow with UrQMD [1], DCM-QGSM [2], LA-QGSM [2], and HSD [3] heavy-ion event generators is compared with existing experimental data. Figure 1 shows the slope of proton directed flow at midrapidity, $F_y(v_1) = dv_1/dy$, for different collision generators compared with E895 [4] and STAR [5] experimental data. Protons are used for the directed flow comparison as the most abundant particles in this kinematic region. The magnitude of the directed flow generated with different collision generators varies significantly, while DCM-QGSM seems to be the most consistent in describing the data over the whole energy range. The possibility of collision fragment generation in the spectator region and the qualitative agreement with the experiment data for directed flow justifies the use of the DCM-QGSM for the PSD performance study.

The CBM detector response is simulated with GEANT4 Monte-Carlo for three different configurations: (1) "PSD-accept." when simulated azimuthal distribution of the particles within geometrical acceptance of the PSD ($0.215° < \theta < 5.0°$ for $E_{beam} = 2 - 8$ AGeV and $0.115° < \theta < 2.7°$ for $E_{beam} = 30$ AGeV) were used without simulating the actual PSD response; (2) "PSD-geom.,B=0" when PSD response is simulated without CBM magnetic field (this allows to study the bias due to finite PSD segmentation); (3) "PSD-geom.,B>0" - same as configuration (2) but with magnetic field on. Reaction plane resolution, quantified in terms of correction factor used in the directed flow measurement, is shown in Fig. 2. Resolution simulated with the DCM-QGSM generator is similar to that of E877 experiment [6]. The transverse segmentation of the PSD seems to have a small effect. The CBM magnetic field introduces significant bias, while the reaction plane resolution is still high even in a presence of the magnetic field.

* Work supported by the European Community FP7 - Capacities, contract HadronPhysics3 n°283286 and grant LG12007 of the Ministry of Education of the Czech Republic.
† mikhaylov@ujf.cas.cz

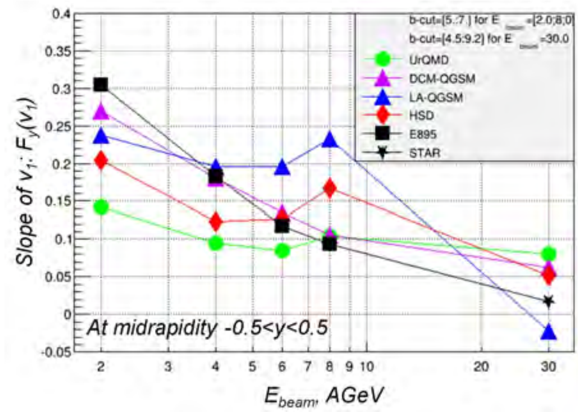

Figure 1: The slope of proton directed flow at midrapidity simulated with different collision generators is compared with E895 [4] and STAR [5] experimental data.

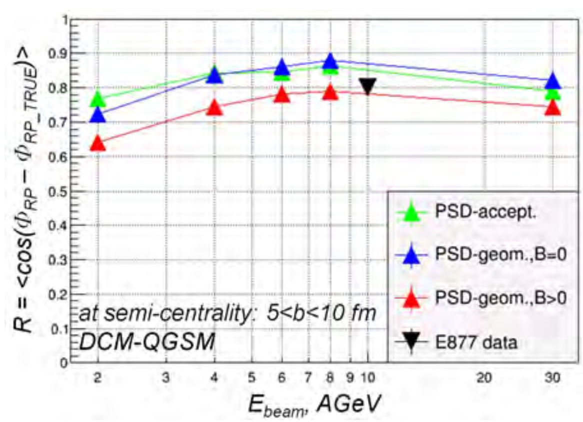

Figure 2: First order reaction plane resolution correction factor simulated with DCM-QGSM and E877 [6] data.

References

[1] The UrQMD model, urqmd.org.
[2] The SHIELD code, www.inr.ru/shield/index.html.
[3] The HSD model, fias.uni-frankfurt.de/ brat/HSD/index1.html
[4] H. Liu et al. (E895), Phys. Rev. Lett. 84 (2000), p. 5488.
[5] L. Adamczyk et al. (STAR), Phys. Rev. Lett. 112 (2014).
[6] 7. J. Barrette, et al. (E877), Phys. Rev. C55 (1997), p. 1420.

Towards a realistic event generator for in-medium and QGP dileptons

F. Seck[1], *I. Fröhlich*[2], *T. Galatyuk*[1,3], *J. Markert*[2], *and J. Stroth*[2,3]

[1]Technische Universität Darmstadt, Germany; [2]Goethe-Universität Frankfurt, Germany; [3]GSI, Darmstadt, Germany

Until now the hadronic cocktails produced with the event generator Pluto [1] for the HADES and CBM experiments included only a contribution from freeze-out sources.

However as dileptons are radiated from the fireball during the whole space-time evolution, medium effects like the broadening of the ρ should also be included in the simulations. Calculations of the in-medium ρ spectral function by R. Rapp and J. Wambach [2] demonstrate, that a large part of the in-medium ρ mesons feed into the mass region below the ρ/ω pole mass down to zero masses.

The basic idea behind the event generator under development is to simulate an ensemble of events with a transport model like UrQMD [3]. The space-time evolution of these events is then divided into four-dimensional cells (similar approaches have been conducted in [4,5]). Afterwards the quantities needed as input for the Rapp - Wambach spectral function, i.e. temperature T, the baryon chemical potential μ_B (or density ϱ_B) and the collective flow velocity $\vec{v}_{coll}$, can be extracted locally for each cell.

The observation, that the momentum distributions start after ~5 fm/c to resemble Gaussians, suggests a thermalization of the system, thus we have used a Maxwell-Boltzmann fit to determine the temperature of the cell. The net baryon as well as the energy density can be obtained with the four-current method [6].

The temperature and baryon density evolution results in the trajectory of the cell. Figure 1 shows this trajectory followed by the cell at the center of the collision.

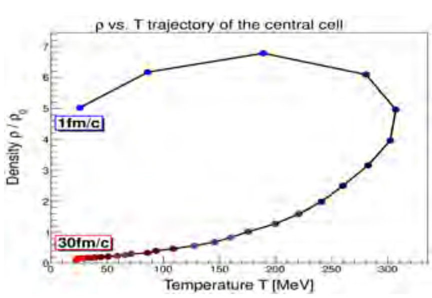

Figure 1: Phase-space trajectory of the central cell in Au+Au at 20 AGeV as extracted from UrQMD tranport model calculations. A marker is indicating time evolution in 1 fm/c steps.

The modular structure of Pluto makes it feasible to customize the event generator and incorporate models of in-medium physics, like the Rapp - Wambach spectral function, as well as the emission due to multi-pion annihilation and QGP radiation as plug-ins.

If the input parameters to the thermal emission rates exceed a certain threshold we will use the in-medium spectral function for the dileptons emitted from this cell. Otherwise the vacuum spectral functions will be utilized.

Figure 2 shows the hadronic cocktail produced with Pluto for Au+Au collisions at a beam energy of 25 AGeV with the in-medium ρ and ω contributions provided by R. Rapp. In addition the dileptons stemming from QGP radiation are included in the cocktail.

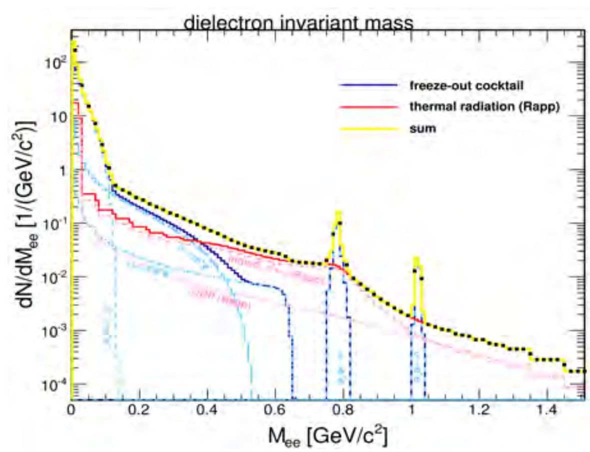

Figure 2: Dilepton cocktail for Au+Au collisions at 25 AGeV produced with Pluto including also in-medium and QGP contributions.

In the upcoming months the focus will lie on the calculation of the dilepton emission rates for different collision systems at FAIR energies with a spectral function package from R. Rapp. Consistency checks will be done as well.

The main objective of this work is then the implementation of this concept into Pluto in such a way as to enable users to pick the collision system of their choice and simulate a realistic dilepton mass spectrum for their analyses.

We thank Ralf Rapp for providing m-p_T-distributions of the in-medium spectral function.

References

[1] I. Fröhlich *et al.*, PoS **ACAT2007** (2007) 076
[2] R. Rapp and J. Wambach, Adv. Nucl. Phys. **25** (2000)
[3] S. Bass *et al.*, Prog. Part. Nucl. Phys. **41** (1998) 255
[4] J. Kapusta, Nucl. Phys. **A 715** (2003) 709
[5] S. Endres *et al.*, arXiv:1412.1965
[6] S. Vogel *et al.*, Phys. Rev. **C 78** (2008) 044909

π^0 reconstruction through a γ-conversion method with KF Particle Finder in the CBM experiment*

M. Zyzak†[1,2,3], *I. Kisel*[1,2,3], *and I. Vassiliev*[1]

[1]GSI, Darmstadt, Germany; [2]Goethe-Universitaet Frankfurt, Frankfurt am Main, Germany; [3]Frankfurt Institute for Advanced Studies, Frankfurt am Main, Germany

The CBM experiment is being designed to study heavy-ion collisions at extremely high interaction rates and track densities. One of the main observables for CBM are light vector mesons decaying through dilepton channels, that are of the particular importance for the physics program of the experiment. Because of the low branching ratio the key issue for reconstruction of light vector mesons is background suppression. Being a major source of this background, π^0 and γ-conversion have to be carefully studied.

The main decay channel of π^0 is a $\pi^0 \rightarrow \gamma\gamma$ channel with a branching ratio of 98.8%. The γ can be reconstructed in the Silicon Tracking System (STS) when it was converted into an electron-positron pair on the material or support structures of the detector: $\gamma \rightarrow e^+e^-$. To study this decay π^0 reconstruction through a γ-conversion method was implemented in the KF Particle Finder package for short-lived particle reconstruction.

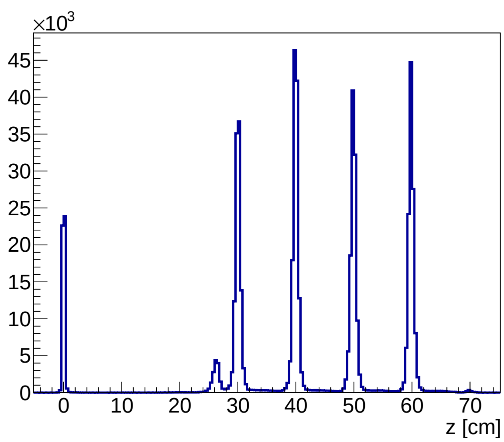

Figure 1: Distribution of γ-particles reconstructed z-position. The obtained histogram represents position of the target, a beam pipe window and four stations of the STS detector.

At the first stage tracks from electrons and positrons registered in STS are selected using particle identification (PID) information from the Ring Image Cherenkov Detector (RICH), Transition Radiation Detector (TRD) and Time of Flight (ToF) detector. Selected tracks are combined into γ-candidates. Based on the Kalman filter mathematics, the KF Particle Finder package allows to achieve high reconstruction quality of the particles. For example, distribution of the reconstructed z-position nicely represents the structure of the detector: the target at 0 cm, the beam pipe window at 26 cm and four stations of the STS detector at 30, 40, 50 and 60 cm (see Fig. 1). Then the γ-candidates within 3σ region around the peak position (0 MeV/c^2) are selected and combined with each other. High quality of the γ-candidates allows reconstruction of π^0 with a width of 1.7 MeV/c^2 and signal to background ratio of 0.77 already for 5 million central AuAu events at 25 AGeV (see Fig. 2).

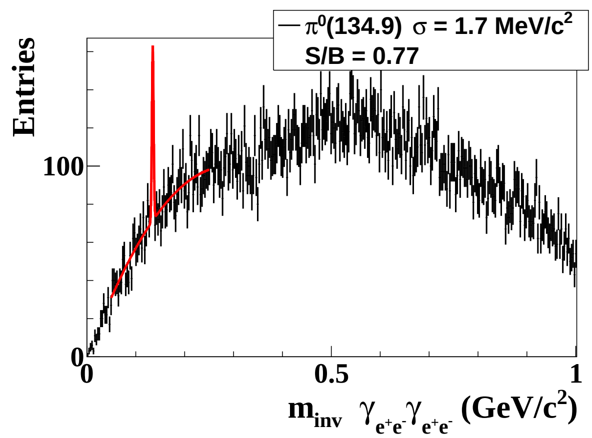

Figure 2: Mass distribution of $\gamma\gamma$ pairs for 5 million central AuAu events at 25 AGeV using PID information form RICH, TRD and ToF detectors. The peak from π^0 is nicely seen with a width of 1.7 MeV/c^2 and a signal to background ratio of 0.77.

Average gamma conversion factor within the STS detector is about 6.5%. This gives a probability of $4 \cdot 10^{-3}$ for both γ-daughters to produce tracks. Tacking into account efficiency of the track finding, PID detector and particle construction the overall π^0 reconstruction efficiency is about 10^{-6}. However, the big advantage of the method is high resolution and signal to background ratio.

Summarizing, π^0 reconstruction was implemented in the KF Particle Finder package. High quality of the obtained π^0 particles makes it possible to study the background for dielectron decays of the rare probes.

* Work supported by HICforFAIR, FIAS and HGS-HIRe for FAIR.

† m.zyzak@gsi.de

CBM Physics

Heavy-quark dynamics in a hot and dense medium*

H. Berrehrah[1], *E. Bratkovskaya*[1], *W. Cassing*[2], *P.B Gossiaux*[3], *and J. Aichelin*[3]
[1]Frankfurt Institute for Advanced Studies; [2]Institut für Theoretische Physik, Giessen; [3]Subatech, Nantes, France

Introduction

We study the dynamics of on- and off-shell heavy quarks Q in the quark-gluon plasma (QGP) as produced in relativistic nucleus-nucleus collisions. The interactions of heavy quarks with the partonic environment at finite temperature T and finite quark chemical potential μ_q are investigated in terms of transport coefficients within the dynamical quasiparticle model (DQPM) designed to reproduce the lattice-QCD (lQCD) results (including the partonic equation of state) in thermodynamic equilibrium. The collisional scattering cross sections σ^Q_{elas} are evaluated for perturbative partons (massless on-shell particles) and for dynamical quasi-particles (massive on or off-shell particles) using the leading order Born diagrams [2, 3].

Charm spatial diffusion coefficient

Based on σ^Q_{elas} in a finite T and μ_q medium [1, 2, 3, 4], the on- and off-shell heavy quark dynamical collisional energy loss and transport coefficients are computed [1, 3, 4]. As an example, the charm spatial diffusion coefficient D_s is shown in Fig. 1 at finite T (top) and finite T and μ_q (bottom) where our non-perturbative DpQCD model (Dressed pQCD using DQPM pole masses for the partons) is confronted with nuclear many-body calculations below and close to the critical temperature T_c from Ref.[5].

The hadronic and partonic D_s join smoothly and show a pronounced minimum close to T_c at $\mu_q = 0$ as well as at finite μ_q . Close to and above T_c its absolute value matches the lQCD calculations for $\mu_q = 0$. The smooth transition of the heavy-quark transport coefficients from the hadronic to the partonic medium corresponds to a crossover transition in line with lattice calculations, and differs substantially from perturbative-QCD calculations (Moore & Teaney) which show a large discontinuity at T_c. This indicates that in the vicinity of T_c dynamically dressed massive partons should be the effective degrees of freedom in the quark-gluon plasma.

The heavy quark scattering cross sections and transport properties [1, 2, 3, 4] form the basis of a consistent study of the heavy quark dynamics in heavy-ion collisions at FAIR, SPS, RHIC and LHC energies where the partonic processes are implemented into the Parton-Hadron-String-Dynamics (PHSD) transport approach.

* Work supported by DFG and "HIC for FAIR" framework of the "LOEWE" program. The computational resources have been provided by the LOEWE-CSC.

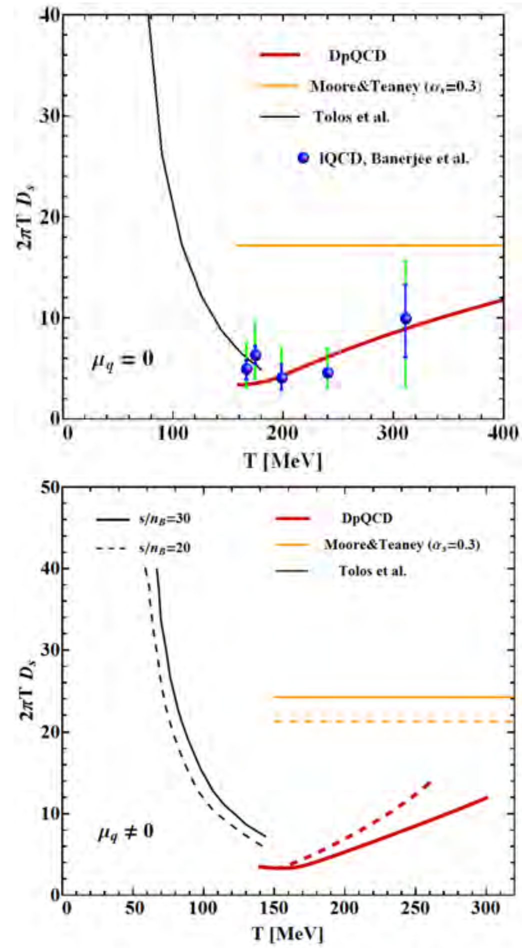

Figure 1: Spatial diffusion coefficient for heavy quarks, D_s, as a function of T for $\mu_q = 0$ (top) and $\mu_q \neq 0$ (bottom). The hadronic diffusion coefficient is taken from [5]. For partonic environment the result from the DpQCD model is compared to pQCD [6], and lattice calculations from Ref. [7].

References

[1] H. Berrehrah, *et al.,* Phys. Rev. C 90 (2014) 051901.

[2] H. Berrehrah, *et al.,* Phys. Rev. C 89 (2014) 054901

[3] H. Berrehrah, *et al.,* Phys.Rev. C90 (2014) 064906

[4] H. Berrehrah, *et al.,* arXiv:1412.1017 [hep-ph]

[5] L. Tolos and J.M. Torres-Rincon, Phys. Rev. D 88, 074019 (2013).

[6] G.D. Moore and D. Teaney, Phys. Rev. C 71, 064904 (2005).

[7] D. Banerjee *et al.*, Phys. Rev. D 85, 014510 (2012).

Rapidity dependent strangeness enhancement of the produced particles at FAIR energies*

K. Dey[1,2] *and B. Bhattacharjee* [†2]

[1]Department of Physics, Bodoland University, Kokrajhar, India; [2]Department of Physics, Gauhati University, Guwahati India

It has now been understood that the width of the rapidity distribution of various produced particles, in addition to kinematic effect, has got a non-trivial baryon density effect as well [1]. The heavy ion collision at FAIR energies, where the baryon density could be something of the order of 5-10 times the normal nuclear matter density, might play a vital role in understanding the role of rapidity distribution of net-baryon density on the width of the rapidity distribution of hadrons containing leading quarks. Further, strangeness enhancement which has been considered as one of the traditional signatures of QGP is studied quite extensively considering strangeness to be conserved both globally and locally. However, Steinheimer *et al.* [2] from UrQMD calculation predicted that although strangeness is conserved globally, yet, it is not uniformly distributed over rapidity space leading to a local violation of strangeness conservation. Due to the limitation of the detector acceptance, the past and ongoing heavy ion experiments could measure the strangeness enhancement at midrapidity only. A number of strange particles do contain leading quark(s) and thus a study of the rapidity dependent strangeness enhancement is of considerable importance.

In this work, by generating 93 million UrQMD events, an attempt has therefore been made to study the rapidity dependent strangeness enhancement at FAIR energies.

Following the reference [3], the strangeness enhancement factor is defined as –

$$E_S = \left[\frac{(Yield)_{AA}}{\langle N_{\pi^-} \rangle}\right]_{central} \Big/ \left[\frac{(Yield)_{AA}}{\langle N_{\pi^-} \rangle}\right]_{peripheral}$$

In Fig.1, the strangeness enhancement factor (E_S) has been plotted as a function of rapidity for various identified particles for $Au+Au$ collision at 30A GeV. It is interesting to see from the figure that E_S depends strongly on rapidity and this dependence follow two distinctive patterns. While the enhancement factor at mid-rapidity is found to be maximum for the particles containing leading quarks (filled circle), the same is observed to be minimum at mid-rapidity for the particles containing produced quarks only (open circle). Even though, $\Omega^-(sss)$, consisting of three produced quarks, is observed to be behaving differently than those hadrons with all its constituents as produced quarks, a slight decrease in the enhancement at mid-rapidity is clearly visible. This apparent anomalous behavior could be because of the contribution of Ξ^- (containing one leading quark), in the production of Ω^- via $\Xi K^- \to \Omega\pi$ channel.

To understand the underlying dynamics of such rapidity

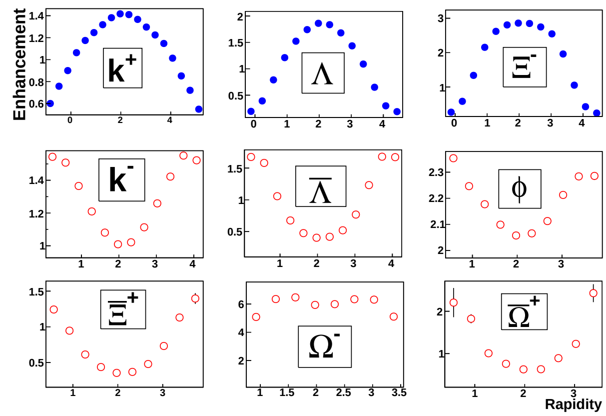

Figure 1: Strangeness enhancement factor as a function of rapidity for particles containing at least one leading quark (filled circle) and particles containing only produced quarks (open circle) for $Au + Au$ collision at 30A GeV.

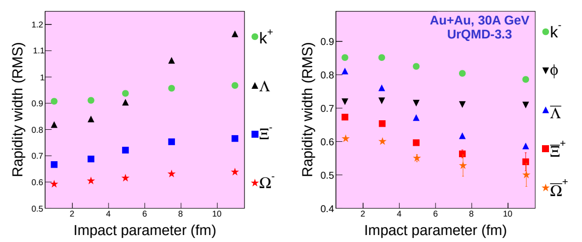

Figure 2: Rapidity width as a function of impact parameter for identified particles for $Au + Au$ collision at 30A GeV.

dependent strangeness enhancement, in Fig.2, the widths of the rapidity distribution of the identified particles are plotted as a function of centrality. It is readily evident from this figure that the different patterns of rapidity dependence of strangeness enhancement factor for particles containing and not containing leading quarks lie on the dependence of rapidity width on centrality. The width of the rapidity distribution increases as we go from central to peripheral collisions for the particles containing leading quarks, a feature that might be attributed to the variation of net-baryon density with impact parameter. It is also seen from Fig.2 that for all but Ω^-, rapidity width follows a decreasing pattern with decreasing centrality for the particles containing produced quarks only. Such observation may be attributed to the fact that the size of the central fireball and hence the scattering effect decreases with the decreasing centrality.

References

[1] K. Dey, B. Bhattacharjee, Phys. Rev. C **89**, 054910 (2014).
[2] J.Steinheimer *et al.* Phys. Lett. **B676** (2009).
[3] S. Soff *et al.* Phys. Lett. **B471**, 89-96,1999

* Work supported by DST Govt. of India
† buddhadeb.bhattacharjee@cern.ch

K^* dynamics in a nuclear medium*

Andrej Ilner[†1,2], *Daniel Cabrera*[‡1,2], *and Elena Bratkovskaya*[§1,2]

[1]Frankfurt Institute for Advanced Studies, Ruth-Moufang-Straße 1, 60438 Frankfurt am Main, Germany; [2]Institut für theoretische Physik, Johann Wolfgang Goethe-Universität, Max-von-Laue-Straße 1, 60438 Frankfurt am Main, Germany

The K^* and the $\bar{K}^*$ are vector mesons that are composed of a light and a strange quark, i.e. the K^* is composed of a u and a $\bar{s}$ quark and the $\bar{K}^*$ is composed of a u and a s quark. We study the in-medium properties of these mesons in a dense and hot nuclear medium. The in-medium properties are based on chirally motivated models and these in-medium effects are parametrised as density or temperature dependent effective masses and widths. For broad in-medium particles we adopt the relativistic Breit-Wigner prescription, i.e. the spectral function

$$A_i(M,\rho_N) = \frac{\frac{2}{\pi}\cdot C_1 \cdot M^2 \cdot \Gamma_i^*(M,\rho_N)}{\left(M^2 - M_i^{*2}(\rho_N)\right)^2 + \left(M\Gamma_i^*(M,\rho_N)\right)^2}\,, \tag{1}$$

where C_1 stands for a normalisation constant, which is determined as the spectral function must fulfil the sum rule $\int_0^\infty A_i(M,\rho_N)dM = 1$, and $i = K/\bar{K}, K^*/\bar{K}^*$.

The in-medium effects are based on the complex self-energy obtained by solving the strange meson (off-shell) dispersion relation $E^2 - |\vec{p}^2| - M_i^2 - \Pi_i = 0$, i.e. the width of the spectral function is related to the imaginary part of the self-energy as

$$\mathrm{Im}\,\Pi_i(M,\rho_N) = -\Gamma_i^*(M,\rho_N)\cdot M \tag{2}$$

and the mass shift is related to the real part of the self-energy as

$$\mathrm{Re}\,\Pi_i(M_i^*,\rho_N) = M_i^2 - (M_i^*)^2 \tag{3}$$

(with M_i being the nominal mass in vacuum, i.e. $M_{K^*} = 0.892$ GeV). A vacuum width of $\Gamma_V^0 = 42$ MeV has been used throughout all of our calculations for the vector mesons.

We distinguish two scenarios for energies where the medium is dense and is filled with baryonic particles (FAIR; $\mu_B \neq 0, T \approx 0$) and when the medium is hot and filled with pionic particles (RHIC, LHC; $\mu_B \approx 0, T \neq 0$). The behaviour of strange vector mesons is different for these two media. Additionally the behaviour of a strange particle is different from the behaviour of a strange anti-particle in a dense nuclear medium, whereas it is the same in a hot nuclear medium (we are dealing with an isotopically symmetric pionic medium).

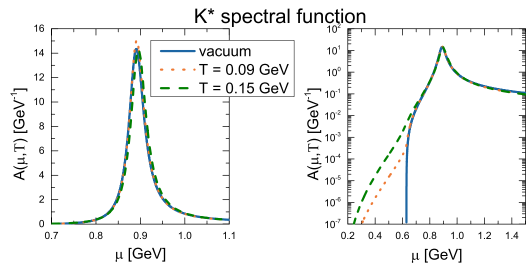

Figure 1: The K^* spectral function is shown as a function of the invariant K^* mass μ for different temperatures T. The blue solid line is for the vacuum case, the orange dotted line is for a temperature of $T = 0.09$ GeV and the green dashed line is for a temperature of $T = 0.15$ GeV. The same results are shown on a linear (left plot) and on a logarithmic (right plot) scale.

In figure 1 one can see spectral function for the K^* (and consequently the $\bar{K}^*$) in a hot, pionic medium. The effects of the medium are negligible, there is only a small mass shift and a very small broadening. However, when looking at the logarithmic plot one can see that the K^* gains some enhancement in the low mass region at temperatures $T > 0$.

For the K^* in a dense nuclear medium the width of the K^* decreases with increasing density since the kaon becomes slightly heavier as a result of the repulsive KN interaction. However, this is compensated by the repulsive self-energy from the K^*N interaction. The resulting K^* self-energy in a $t\rho$ approximation leads to a mildly repulsive K^* mass shift of about 5% (30 MeV) at a density of $\rho_N = \rho_0$. The change in the shape of the spectral function is negligible.

The major effects for the $\bar{K}^*$ in a dense nuclear medium come mainly from both the $\bar{K}\pi$ decay channel and from the highly inelastic $\bar{K}^*N$ interaction, leading to decay widths as large as 200 MeV at normal nuclear matter density $\rho_N = \rho_0$.

* Work supported by the Helmholtz International Center for FAIR within the framework of the LOEWE program, HGS-HIRe for FAIR, H-QM and the BMBF (Germany) under project no. 05P12RFFCQ.

† ilner@fias.uni-frankfurt.de
‡ cabrera@fias.uni-frankfurt.de
§ Elena.Bratkovskaya@th.physik.uni-frankfurt.de

References

[1] Andrej Ilner, Daniel Cabrera, Pornrad Srisawad, Elena Bratkovskaya, *Properties of strange vector mesons in dense and hot matter*, Nucl. Phys. A 927 (2014) 249-265

Nuclear fragments at CBM at SIS100

V.P. Ladygin[*1], *K.K. Gudima*[1,2], *N.B. Ladygina*[1], *and A.A. Lebedev*[1,3]
[1]LHEP-JINR, Dubna, Russian Federation; [2]IAP, ASM, Kishinev, Moldova; [3]GSI, Darmstadt, Germany

The light nuclear fragments are formed from nucleons at the latest stage of the evolution of the fireball, called the stage of freeze-out. The simple coalescence models [1] predict that the invariant yield of light nuclei with mass A is proportional to the A-th power of the nucleon yield and coalescence factor B_A, which characterizes the coalescence probability. This factor depends on the fireball size, it can be measured in the experiment and used to estimate the reaction volume in which the composite particles are created.

The simulation has been performed for 100K of the Au+Au minimal bias events at 4 A·GeV using Dubna Cascade Model [2] for the hadron version of the CBM detector at SIS100. The secondary particles have been selected using m^2-p/Z correlation, where momentum and time-of-flight were reconstructed from STS and TOF information, respectively. This method leads to some contamination of misidentified protons, especially at high momentum values [3].

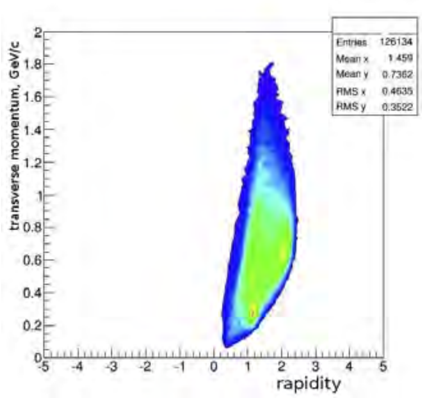

Figure 1: $y - p_T$ distribution for deuterons from $Au + Au$ minimal bias collisions at 4 A·GeV [2].

The transverse momentum- rapidity, $y - p_T$, distribution for deuterons from the $Au + Au$ minimal bias collisions at 4 A·GeV [2] is presented in Figure 1. The yield is ∼1.2 deuteron/event with ∼97% of the purity selection. The dominant reaction mechanisms are the coalescence and projectile fragmentation. The deuterons with the rapidity values ∼1.2 and typical transverse momenta p_T ∼0.3 GeV/c are produced via the coalescence, while the deuterons with the rapidity values ∼2.0 come from the fragmentation process.

The $y - p_T$ distribution for tritons from the $Au + Au$ minimal bias collisions at 4 A·GeV [2] is presented in Figure 2. The yield is ∼0.046 tritons/event with ∼90% of the purity selection. Here, the dominant mechanism is the coalescence. The purity selection for ^{3}He using m^2-p/Z correlation is much worse (∼40%) due to large contamination of the background protons and deuterons. Additional information on the charge of the nuclear fragments is required to improve the purity.

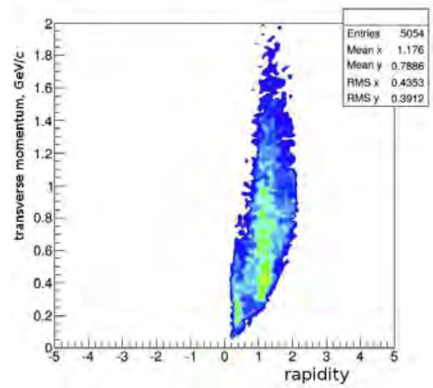

Figure 2: $y - p_T$ distribution for tritons from the $Au + Au$ minimal bias collisions at 4 A·GeV [2].

The yields for the deuterons and tritons obtained from the simulation for 100K of the central $Au + Au$ collisions at 4 A·GeV [2] are ∼4.1 and ∼0.24, respectively. The purities of the selection are found being the same as for the minimal bias events. The dominant reaction mechanism is the coalescence for the both nuclei.

The CBM setup at SIS100 allows to obtain the data on the light nuclei production in the mid- and forward rapidity regions. Systematic studies of the light nuclear fragments and hyper-nuclei production with CBM could distinguish different approaches in the description of the relativistic heavy ion collisions [4].

References

[1] L.P. Csernai, J.I. Kapusta, Phys.Rep.131 (1986) 223.

[2] V.D. Toneev, N.S. Amelin, K.K. Gudima, S.Y. Sivoklokov, Nucl.Phys. A519 (1990) 463C.

[3] V.P. Ladygin, A.I. Malakhov and T.A. Vasiliev, CBM Progress Report 2010, Darmstadt 2011, p.58.

[4] J. Steinheimer et al., Phys.Rev.B714 (2012) 85.

* vladygin@jinr.ru

Creation and annihilation of antimatter at FAIR energies*

P. Moreau[1], *J. Aichelin*[2], *and E. Bratkovskaya*[1]

[1]Frankfurt Institute for Advanced Studies, Johann Wolfgang Goethe Universität, Ruth-Moufang-Strasse 1, 60438 Frankfurt am Main, Germany; [2]Subatech, UMR 6457, IN2P3/CNRS, Université de Nantes, Ecole des Mines de Nantes, 4 rue Alfred Kastler, 44307 Nantes cedex 3, France

The 'Big Bang' scenario implies that in the first microseconds of the universe the entire state has emerged from a partonic system of quarks, antiquarks and gluons – a quark-gluon plasma (QGP) – to color neutral hadronic matter consisting of interacting hadronic states (and resonances) in which the partonic degrees of freedom are confined. Nowadays this early phase can be reproduced in relativistic heavy ion collisions. They show indeed that such a QGP can exists and that it interacts more strongly than hadronic matter. Consequently the concept of a weakly interacting system described by perturbative QCD (pQCD) has to be questioned.

The dynamics of partons, hadrons and strings in relativistic nucleus-nucleus collisions can be analyzed within the Parton-Hadron-String Dynamics approach [1, 2]. In this transport approach the partonic dynamics is based on Kadanoff-Baym equations for Green functions with self-energies from the Dynamical QuasiParticle Model (DQPM) which describes QCD properties in terms of 're-summed' single-particle Green functions [3]. The lattice QCD results, of which the parameters of DQPM are fitted on, lead to a critical temperature $T_c \approx 160$ MeV which corresponds to a critical energy density of $\epsilon_c \approx 0.5$ GeV.fm^{-3}.

The aim of this project is with the help of the PHSD to study the creation and annihilation of anti-matter at the FAIR facility in the future CBM and PANDA experiments. Since anti-matter (or antiparticles) doesn't exist in our world it has to be created first by strong interactions before its dynamics can be studied in different hadronic or partonic environments. These experiments aim at the exploration of the QCD phase diagram, especially to find out the order of the phase transition between hadrons and partons at high baryonic densities. In addition we will study the optical potential of different hadrons and the in-medium properties of hadrons in the strange and the charm sector. To verify that our approach is adequate for this study we start out with the calculation of the measured spectra of particles and anti-particles at RHIC energies. We have found a good agreement with the PHENIX data for single particle spectra in Au+Au (figure 1) and p+p (figure 2) collisions at mid-rapidity. One can see that the production of particles and anti-particles in pp collisions is very similar while in Au+Au collisions we observe the effects of anti-baryon absorption at low p_T as well as rescattering on the partonic and hadronic levels.

* Work supported by HIC4FAIR/HGS-HIRe.

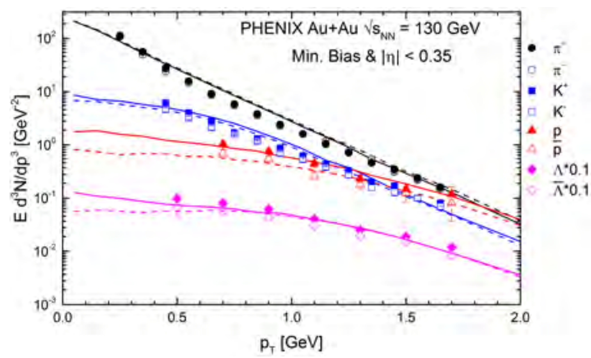

Figure 1: Invariant p_T spectra in Au+Au collisions at $\sqrt{s_{NN}} = 130$ GeV for π^+, π^-, K^+, K^-, p, $\bar{p}$, Λ and $\bar{\Lambda}$ obtained with PHSD, in comparison with the experimental data from the PHENIX collaboration [4, 5].

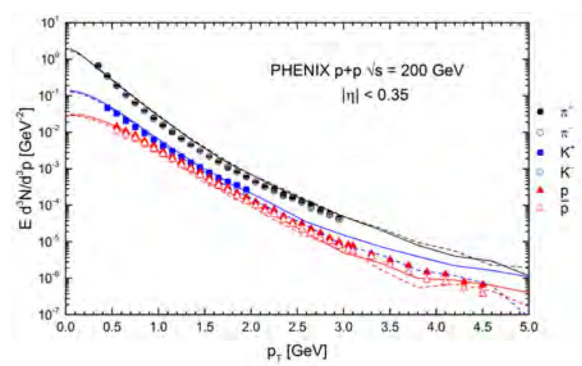

Figure 2: Invariant p_T spectra in p+p collisions at $\sqrt{s} = 200$ GeV for π^+, π^-, K^+, K^-, p and $\bar{p}$ obtained with PHSD in comparison with the experimental data from the PHENIX collaboration [6].

References

[1] W. Cassing and E. L. Bratkovskaya, Nucl. Phys. A **831**, 215 (2009).

[2] E. L. Bratkovskaya, W. Cassing, V. P. Konchakovski and O. Linnyk, Nucl. Phys. A **856**, 162 (2011).

[3] W. Cassing, Eur. Phys. J. ST **168**, 3 (2009).

[4] K. Adcox *et al.* [PHENIX Collaboration], Phys. Rev. C **69**, 024904 (2004).

[5] K. Adcox *et al.* [PHENIX Collaboration], Phys. Rev. Lett. **89**, 092302 (2002).

[6] A. Adare *et al.* [PHENIX Collaboration], Phys. Rev. C **83**, 064903 (2011).

Simulation results on elliptic flow at FAIR energies

S. Sarkar, S.Ghosh, P.Mali, and A.Mukhopadhyay
Department of Physics, North Bengal University, Siliguri 734013, West Bengal

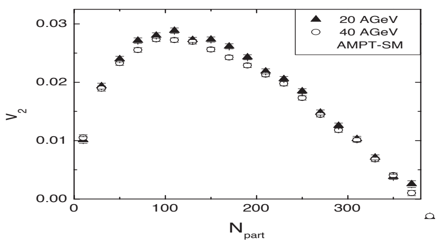

Figure 1: Energy dependence of v_2 versus N_{part}

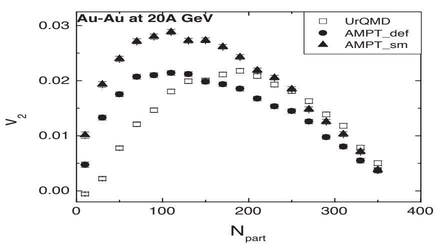

Figure 2: v_2 versus N_{part}

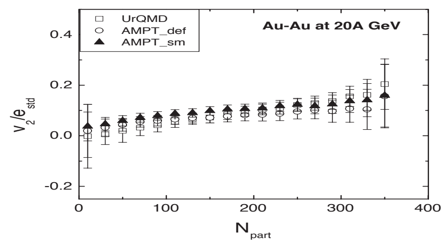

Figure 3: v_2/e_{std} versus N_{part}

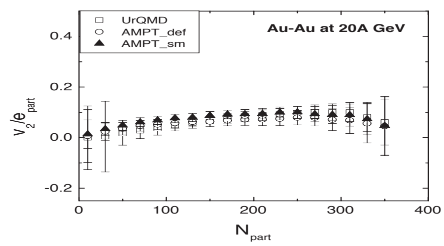

Figure 4: v_2/e_{part} versus N_{part}

In high-energy heavy-ion collisions elliptic flow refers to a preferential emission of particles with respect to certain azimuthal angle [1]. The magnitude of this effect is characterized by an elliptic flow parameter, defined as [2]:

$$v_2 = \langle \cos 2(\phi - \psi) \rangle$$

where ϕ is the azimuthal angle of an outgoing particle, ψ is the azimuthal angle of the impact parameter, and the angular brackets denote averaging over many particles and many events. In this preliminary investigation we report some aspects of the elliptic flow in Au–Au collision at $E_{lab} = 20$A GeV and 40A GeV, using the UrQMD [3] and the AMPT model (both default and string melting versions) [4]. The results are based on a statistics of 2×10^5 events for each simulation. The initial spatial anisotropy of the created system is quantified by the eccentricity [5]:

$$e_{std} = \left(\sigma_y^2 - \sigma_x^2\right) / \left(\sigma_y^2 + \sigma_x^2\right)$$

where σ_x, σ_y denote the standard deviations of the x, y coordinates of the participating nucleons in the transverse plane. However even at fixed impact parameter the number of participating nucleons (N_{part}) and their positions can fluctuate from event to event. To address this issue the eccentricity is redefined [5]:

$$e_{part} = \sqrt{(\sigma_y^2 - \sigma_x^2)^2 + 4(\sigma_{xy})^2} / (\sigma_y^2 + \sigma_x^2)$$

In FIG. 1 we plot v_2 as a function of N_{part} for both incident energies using the AMPT code. We see that the nature of variation of v_2 is almost independent of the incident energy at this energy scale. Similar nature has also been observed for UrQMD and AMPT default. In FIG. 2 we plot v_2 as a function of N_{part} at $E_{lab} = 20$A GeV. Results of all models nearly follow the same pattern, the UrQMD plot being slightly more symmetric than the AMPT plots. Because of the strong asymmetry of the nuclear overlap region in the mid-central collisions, v_2 is large. For the AMPT-string melting model v_2 values of peripheral and mid-central events are found to be the largest. In FIG. 3 and FIG. 4 we have plotted v_2/e_{std} and v_2/e_{part} respectively, against N_{part} for all three models at $E_{lab} = 20$A GeV. Within errors v_2/e appears to scale with N_{part}. Several other aspects of elliptic flow like variation of v_2 with transverse momentum and pseudorapidity (not shown here) are also examined.

References

[1] J. Y. Ollitrault , Phys. Rev. D 46, 229 (1992)

[2] A.M. Poskanzer et al., Phys. Rev. C 58, 1678 (1998)

[3] S.A. Bass et al., Prog. Nucl. Part. Phys. 41, 255 (1998)

[4] Zi-Wei Lin et al., Phys. Rev. C, 2005, 72, 064901

[5] B. Alver et al. (PHOBOS), Phys. Rev. Lett, 2007, 98, 242302.